Czech Technical University in Prague

Faculty of Electrical Engineering

Doctoral Thesis

June 2014   Petr Hoffer

Czech Technical University in Prague

Faculty of Electrical Engineering
Department of Physics

Shock waves generated by corona-like discharges in water

Doctoral Thesis

Ing. Petr Hoffer

Prague, June 2014

Ph.D. Programme: Electrical Engineering and Information Technology
Branch of study: Plasma Physics

Supervisor: Doc. Ing. Pavel Šunka CSc.
Supervisor-Specialist: Prof. RNDr. Pavel Kubeš CSc.

Declaration

I declare that this thesis is a product of my own work, that it has not been submitted before for any degree or examination in any other university, and that all the sources I have used or quoted are indicated and acknowledged as complete References.

Prague, 29.5. 2014   …………………………

Acknowledgements

Table of Contents

1. Introduction, purpose of the thesis

This thesis deals with initiation and propagation of electric discharges in- or in-contact-with water that is (in the second case) called "aqueous electrode" and we speak about penetration of discharges into it. The propagation of discharges in water is accompanied by production of shockwaves and pressure waves. Due to a certain similarity of these discharges with corona discharges in gases they are called *corona-like* discharges. The differences between corona and corona-like discharges are briefly clarified in the Chapter 2, which is based on references [1]-[35]. The rest of the work is divided into two main Chapters 3 and 4. Each of these Chapters has one (Chap. 3) or two (Chap. 4) Experimental parts, where newly received data are presented and finally summarized and assessed (in Conclusion to each Experimental part). Each Experimental part is also preceded by one or more parts, where present knowledge of the subject (state of the art) is given.

Since one of the most frequent initiation mechanisms of underwater discharges is an electrical breakdown of bubbles on a metallic electrode (see Chapter 2), the first part (Chapter 3) is aimed at penetration of electric discharges into the volume of aqueous electrodes (of both polarities) from their surface, and at answering up-to-now opened question of what process on a plasma-liquid boundary causes development of tiny structures producing strong electric field (10^8 V·m^{-1} - 10^9 V·m^{-1}) has not been answered. Experiments utilizing aqueous electrodes as well as experiments aimed at propagation of plasma streamers in liquids are plentifully described in literature. Results of these earlier experiments, the summary of which can be found in the Sub-chapters 3.1 and 3.2 (with appropriate references [36]-[57]), contain important information about main plasma characteristics (temperatures, electron concentrations, etc.). However, none of these experiments is concerned with the mechanism of streamer initiation, i.e. with the mechanism of transition from a gas discharge to a streamer discharge in liquid volume. Therefore, experiments studying the process of gas-discharge to streamer-in-water transition by using of high speed shadowgraphy were performed. The information mentioned in the Sub-chapters 3.1 and 3.2 together with the obtained experimental results described in the Sub-chapter 3.3 (Experimental part 1) were considered, and a mechanism of streamer initiation based on plasma-liquid conductivity ratio has been proposed.

The second main part (Chapter 4) is aimed at shock waves and pressure waves produced by propagating or expanding corona-like discharges in water and especially in highly conductive salt aqueous solutions. Although the existence of this phenomenon is very well known (see e.g. [12][48][49][57][58]), there is only one article [47] containing analysis of pressure field around positive corona-like discharges, specifically, pressure field around positive secondary streamers in a distilled water or in a low conductive aqueous solution. Extract of results from this article [47] can be found in the Sub-chapter 4.2. Therefore, interferometry analysis of pressure field around corona-like discharges was performed not only in distilled water, but also in highly conductive aqueous solutions and at both polarities. These experiments and their results are described in the Sub-chapter 4.3 (Experimental part 2). In addition, analysis of pressure field around corona-like discharges produced on a surface of so called composite (ceramic coated) electrode was performed. The composite electrodes have been developed in the Institute of Plasma Physics AS CR and are being used in the second generation of generators of focused shockwaves, which is briefly described in the Sub-chapter 4.4, and a more detail description of which can be found in [74][75][76]. Analyses of focused shockwaves produced by this generator, obtained by obsolete methods, can be also found in these articles. Hence, the final Sub-chapter 4.5 (Experimental part 3) contains results of pressure field analysis acquired by modern methods: while pressure development in- /near-the-focus of focused shockwave was measured by a fiber optic hydrophone, its propagation has been visualized by a high-speed shadowgraphy. It turns out that the theoretically spherical converging wave is in fact (due to diffraction effects on the pressure-wave periphery) a conical pressure wave, where pressure enhancement appears just in the cone-vertex travelling along the reflector-symmetry-axis.

2. Plasma in gases and liquids

2.1 Low current electric discharges in gases

This section briefly describes the most common mechanisms of discharge development in gases to underline and stress the differences in their development in liquids, especially in water, which will be the subject of next chapters. The ignition of a gas discharge is possible due to presence of some initial charge carriers (electrons or electron-ion pairs), which can be generated by a few different sources. Among the most important charge carrier sources belong:

o Photoemission from cathode caused by impact of photons with energy higher than the output energy of cathode material

$$h\nu \geq e\varphi_o, \tag{2.1}$$

where h [J·s] is the Planck constant, ν [Hz] is the frequency of the incident radiation, e [C] is the elementary charge and φ_o [V] is the cathode material output potential.

o Thermionic emission from heated cathode. The emission current is given by the Richardson equation [1]

$$J = AT^2 e^{\frac{-e\varphi_m}{kT}} \qquad [\text{A·m}^{-2}], \tag{2.2}$$

where A [A·m^{-2}·K^{-2}] is an emission constant, T [K] is the temperature of the cathode surface and k [J·K^{-1}] is the Boltzmann constant. The minimum energy, which must be added to an electron in a metal at $T = 0$ K to enable him to escape from the metal surface, must be great enough to overcome the metal output potential φ_m [V].

o Ionization of atoms/molecules in a bulk gas by a natural agent (cosmic rays, radioactive background, etc.) leading to creation of electron-ion pairs [2]. In the case of ionizing radiation, the process is represented by

$$A + h\nu \rightarrow A^+ + e^-,$$
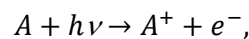
where A denotes particle (atom or molecule).

The two most important gas breakdown mechanisms are based on electron secondary emission and on avalanche of electron and ion production in strong electric field [3].
o The Townsend (relatively slow) mechanism, which needs a large number of secondary electron generations ($\approx 10^2$) to produce breakdown.
o The streamer (rapid) mechanism, which develops directly the first avalanche to breakdown.
These mechanisms are described in more detail in the next two chapters.

The Townsend Mechanism

The Townsend discharge theory is based on so called *Townsend's first ionization coefficient* α, which is the probable number of ionizing collisions made on the average by an electron as it travels one meter along the electric field [1]. The parameter α has the units of ion-electron pairs per meter, and it is related to the mean free path for ionization as follows:

$$\alpha \sim \frac{1}{\lambda_i} = \frac{E_0}{\varphi_i} \qquad [\text{m}^{-1}], \tag{2.3}$$

where λ_i [m] is ionization mean free path, $E_0 = U_0/d$ [V·m^{-1}] is electric field intensity between the plane electrodes at voltage U_0 and the inter-electrode distance d, φ_i [V] is the gas atom (molecule) ionization potential. The λ_i is related to the electron collision frequency, and therefore, to the gas pressure. The parameter α is exactly given by [4]

$$\alpha = Ape^{\frac{-A\varphi_i}{E/p}}, \tag{2.4}$$

where p [Pa] is the gas pressure and A [Pa^{-1}·m^{-1}] is a constant which depends on the electron kinetic temperature and the type of gas. If the cathode emits Γ_{e0} electrons per square meter per second (by photoemission), then electron flux at a distance x from the cathode is

$$\Gamma_e = \Gamma_{e0}e^{\alpha x} \qquad [\text{m}^{-2}\cdot\text{s}^{-1}]. \tag{2.5}$$

Electrons generated by ionization of the gas leave behind them positive ions, which impact the cathode surface (see Figure 1). Total number of electrons emitted from the cathode surface by photo and secondary emission is

$$\Gamma_{ec} = \Gamma_{es} + \Gamma_{e0} = \gamma\Gamma_{ic} + \Gamma_{e0} \qquad [\text{m}^{-2}\cdot\text{s}^{-1}], \tag{2.6}$$

where Γ_{es} is the flux of the secondary emission electrons, Γ_{ic} is the flux of ions impacting the cathode surface and γ is *secondary emission coefficient*. In equilibrium state, the electron flux to the anode is then

$$\Gamma_{ea} = \Gamma_{e0}\frac{e^{\alpha d}}{1-\gamma(e^{\alpha d}-1)} \qquad [\text{m}^{-2}\cdot\text{s}^{-1}]. \tag{2.7}$$

The breakdown occurs when the denominator of equation (2.7) goes to zero

$$1 - \gamma(e^{\alpha d} - 1) = 0. \tag{2.8}$$

In this situation, the current might increase by a factor of 10^8. The condition (2.8) determines the breakdown voltage to be given as [4]

$$U_B = \frac{A\varphi_i p d}{\ln\left(\frac{Apd}{\ln[1+\frac{1}{\gamma}]}\right)}, \tag{2.9}$$

which shows that the breakdown voltage for a particular gas depends only on the product pd (*Paschen's law*). A dependence of the breakdown voltage of air on the product pd is plotted in the Figure 2.
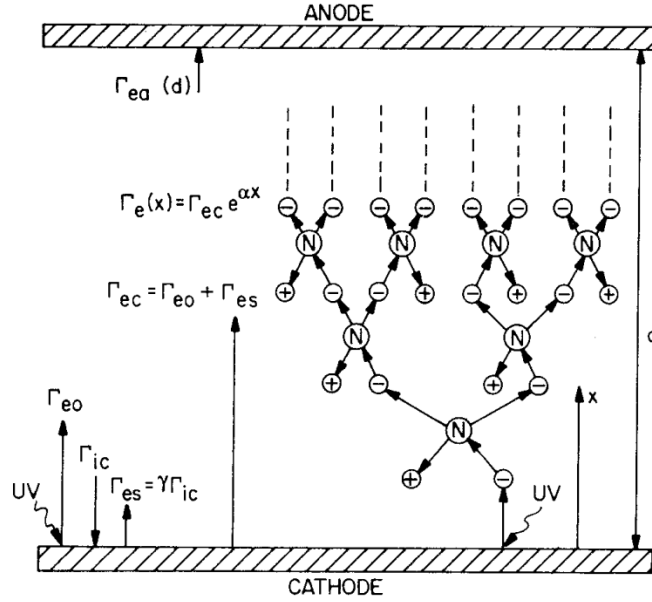
Figure 1 A parallel plate configuration in the dark discharge regime, only ionizing collisions are depicted **[1]**.
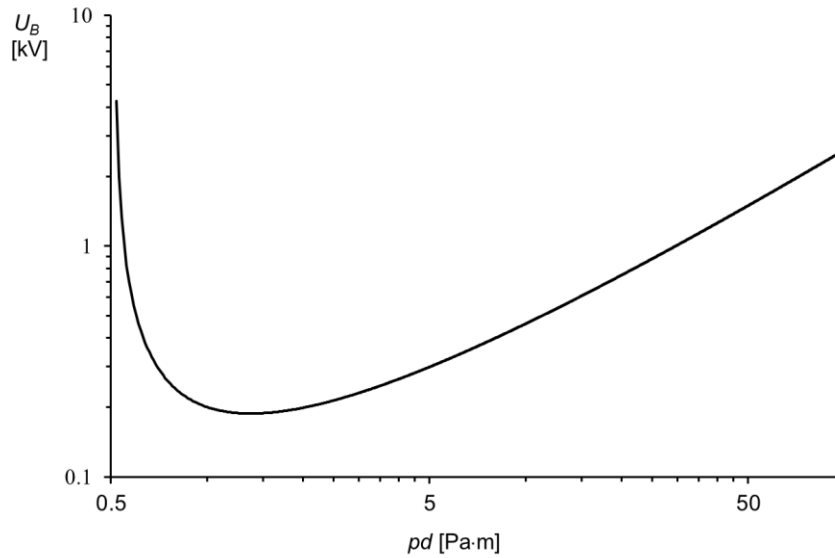
Figure 2 Dependence of the air breakdown voltage U_B on the product pd according to (2.9); used parameters were γ = 10^{-2}, φ_i = 15.5 V (N_2) and A = 9.17 $Pa^{-1} \cdot m^{-1}$.

A minimum of the curve against product pd appears for the following reason: the number of molecules in the gap is proportional to pd. At low p, the electron mean free path is large and few electrons can collide with gas molecules; most of them impinge on the anode and few ionizations take place. In order to have a number large enough for breakdown to occur U_B has to be the larger the smaller p is. At large p, however, the electron mean free path is small and few electrons acquire sufficient energy over a mean free path to ionize. Hence most of the electrons produce electronic or molecular excitation only. Consequently in

4

order to produce enough ionization in the gap, U_B must be large and is higher for larger p. A similar argument would apply for a variation of d [5].

Streamer Mechanism

The Townsend discharge mechanism is valid as long as the electric field of the space charges of the electrons and ions can be neglected compared to the ambient electric field E_0 [3]. The observation of single avalanches between electrodes and the behavior of avalanches of very high amplification ($e^{\alpha d} > 10^8$) led to idea that these space charge fields are essential for the development of very rapid plasma streamers which are able to prepare the breakdown. The electric field around the avalanche is demonstrated in the Figure 3. The field behind and before the head of the avalanche is increased by the space charges and reduced between the electron and ion cloud in comparison with the electrostatic field E_0. The most important difference of this mechanism compared to the Townsend breakdown is that the space charge developed by the avalanche itself transforms the avalanche into a plasma streamer (Figure 4.) The initial seed electrons necessary for this process are generated by the streamer in advance. It makes this mechanism very rapid in comparison with the Townsend breakdown; its velocity reaches to some 10^6 m·s^{-1}.
The empirical condition for streamer formation [3] is

$$\alpha d > 20. \tag{2.10}$$

Using (2.4) and putting $\varphi_i = 15.5$ V (N$_2$), $p = 10^5$ Pa, $A = 9.17$ Pa^{-1}·m^{-1} and $E_B \approx 3$ MV·m^{-1} (approximate air breakdown electric field at normal pressure and millimeter gaps, see Figure 2) we get $\alpha = 8.3\cdot10^3$ m^{-1}. From the condition (2.10) it follows that the streamers do not form in gap with $d < 2.4$ mm, and the Townsend discharge probably happens.
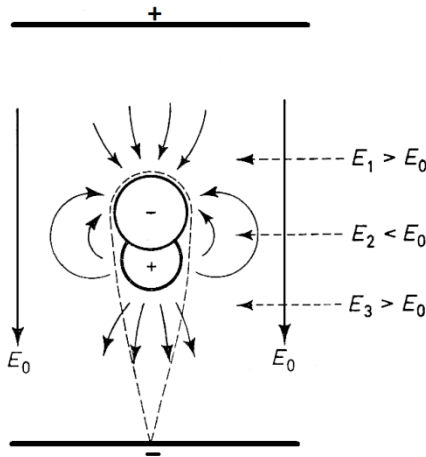
Figure 3 The effect of space charges of an avalanche on the electric field E_0 **[3]**.

If the streamer length is much greater than the streamer tip radius, its velocity and the tip parameters (tip radius, maximum electric field on the tip, electron density) change little during the time the tip travels a distance of its several radii [6]. This means that, depending on the time t and the axial coordinate z (along which the streamer propagates with velocity v_s), all parameters are slowly changing function of a new variable $z-v_s.t$, and, therefore, the group of curves shown in the Figure 4 moves to the right without noticeable distortions. This kind of process represents a wave of strong electric field with highly enhanced ionization. The front portion of the streamer tip is called the *ionization wave front*.
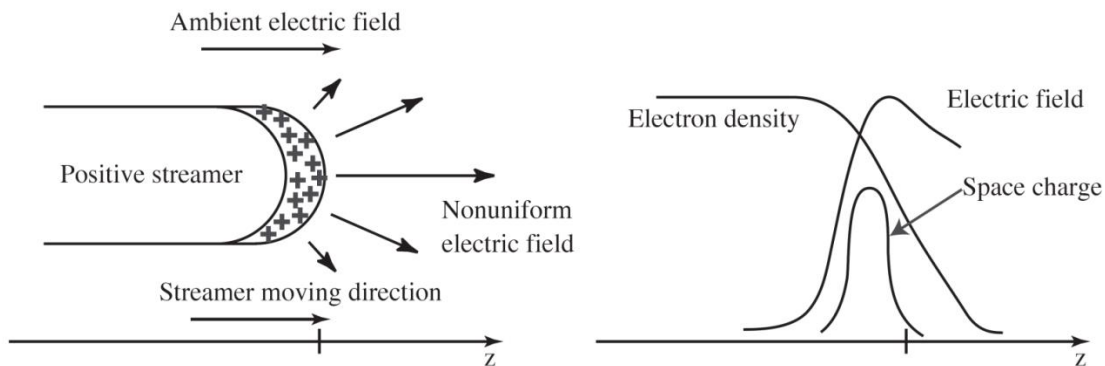
Figure 4 Diagram of a positive streamer propagating in an ambient field [6].

Corona discharge

Corona is a phenomenon which occurs in regions of high electric field near sharp points, edges, or wires in electrically stressed gases prior to the point of electrical breakdown [1]. The phenomenology of corona generated by a sharp point is schematically shown in the Figure 5. Here, corona is generated on the tip of a thin wire of the radius a at potential U_0, which is located in the center of a large grounded spherical electrode of the radius b. The electric field will be the maximum on the tip of wire, and will decrease with radius reaching its minimum at the outer electrode. If b is much greater than a, the maximum local electric field is approximately [7]
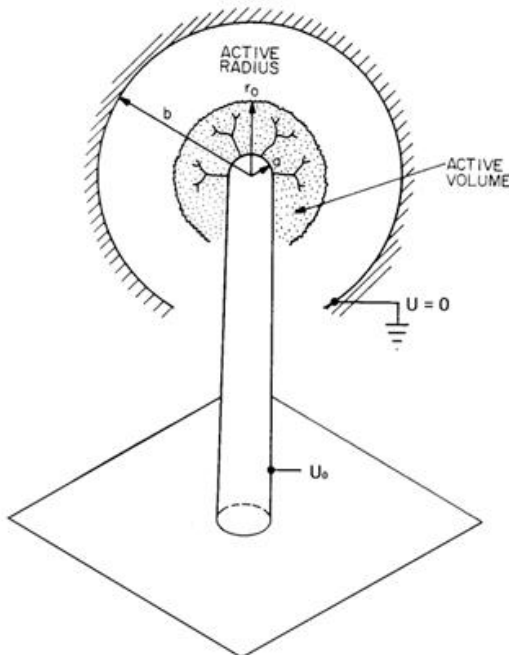
Figure 5 Corona from a sharp point in the form of a hemisphere of a radius a, located at the center of a grounded spherical electrode of a radius b [1].

$$E(r) = E(a) \approx \frac{2U_0}{a \ln\frac{4(b-a)}{a}}.\qquad(2.11)$$

When this local electric field exceeds the breakdown level, the corona appears. Corona discharge may start as a Townsend discharge. If coronal currents are relatively low, the entire corona is dark, appropriate to the dark discharges. At high currents, corona can be technically a 'glow discharge', visible to the naked eye. When the applied voltage, U_0, is higher than necessary to initiate corona, the radius r_0, at which the electric field drops off to the breakdown value is called the active radius. It delimits the active volume (ionization region), where the corona plasma occurs. The space connecting the active volume with the surrounding grounded electrode is the drift region, which, in unipolar coronas, contains preferably drifting charge carriers (positive or negative ions or free electrons (in gases with low electron affinity) of the sign appropriate to the corona polarity. The unipolar current at a given voltage U_0 cannot exceed the saturation limit [8]

$$I_{sat} \approx 2\mu\varepsilon_0 \frac{U_0^2}{d} \ [\text{A}], \tag{2.12}$$

where μ [m^2·V^{-1}·s^{-1}] is the charge carrier mobility, ε_0 [F·m^{-1}] is the vacuum permittivity and d [m] is the distance of the inner electrode to the outer one, here $d = b - a$. At pressure near one atmosphere, electrons attach to oxygen quite readily, and, therefore, the electric current between the active radius and the outer electrode is carried by either negative or positive ions, depending on the polarity of the voltage applied to the inner electrode [1]. For ions in air at atmospheric pressure, this gives

$$I_{sat} \approx 4 \frac{U_0^2}{d} \ [\mu\text{A,kV,mm}]. \tag{2.13}$$

At $U_0 = 10$ kV and $d = 10$ mm (typical values) the corona saturation current is approximately 40 μA.

Negative glow corona is an ordinary glow discharge complete with secondary electron emission from the cathode surface, cathode fall, negative glow, Faraday dark space, and sometimes a positive column. It is usually difficult to establish the negative glow corona in gases with low electron affinity, because of exponentially growing instabilities leading to sparking. In electron attaching gases the sparking is suppressed over a wide current range by negative space charge accumulating in the drift region (e.g. SF$_6$). The glow is oscillatory and unstable at low currents, and the resultant negative glow pulses are called Trichel pulses [2].

Positive glow corona may operate by the Townsend mechanism to the distant cathode, or by a continuous succession of bursts. It has no connection with an ordinary glow discharge, as the space charges present are inessential, and never energetic enough to move the ionization region to the cathode. Experiments show that most positive glow coronas have active volume that oscillates with frequencies depending on the gas, geometry, and average discharge current. Linear damped oscillations are due to ionization region capacitance and equivalent inductance. Nonlinear self-sustained oscillations are formed by periodic quenching by the generated positive ions [9].

Next to the glow coronas, *negative* and *positive corona streamers* can be generally realized by the streamer mechanism. The negative corona streamer occurs when number of electrons in the avalanche head grows to about 10^8, and the space charge field becomes of the order of the original field. Behind the avalanche front the electric field falls nearly to zero. It is area of nearly neutral plasma containing electrons and positive ions intermixed. Drift velocity and ionization nearly cease behind the avalanche head and increase in front of it. In addition photoelectrons generated ahead of the avalanche can increase the front propagation velocity to values greatly exceeding the electron drift velocity in the original electric field. Negative corona streamers may be realized directly in virgin gas by electric field strong enough, or may break out from a negative corona glow.

Positive corona streamers consist of an avalanche head containing about 10^8 positive ions, connected to the positive electrode by a low-field plasma channel. This head is shaped as a disk with diameter of 200 μm and 20 μm thick [10]. Also in this case the space charge field enhances the electric field in front of the streamer head (Figure 4) and thus creates an ionization region. Electrons liberated ahead of this region by photoionization, or photodetachment (from negative ions), or supplied by emission from the distant cathode will trigger new avalanches near the streamer head and thus extend the streamer by adding slow positive ions (with low mobility) to the head and mobile neutralizing electrons to the channel. Positive corona streamers often occur either as bursts of ionization or grow out from the positive glows at high currents.

2.2 Electric discharges in liquids

The breakdown mechanism in liquids is more complicated than in gases, because liquids are much denser. Experimental data on the electric breakdown of liquids that were accumulated, confirm that there are several different breakdown mechanisms that cannot be described in the context of a unified theory. At least five different mechanisms of the discharge initiation can be identified.

Microexplosive liquid discharge initiation

The *microexplosive* liquid discharge initiation mechanism is based on electron emission into the liquid [11] (in the case of discharge from the cathode) or on ionization of liquid molecules (in the case of discharge from anode) [12] [13] [14].
Current of induced charge carriers quickly heats up the liquid, that starts to expand and a shock wave is formed. A pressure dip behind the shock wave allows explosive vaporization of the liquid and consequently ionization of gas-vapor bubbles (initiation of a plasma channel). The most important condition for realization of the microexplosive discharge initiation is the strong electric field near the electrode that can be achieved at nanosecond voltage pulse durations. Favorable factors for realization of this condition, next to using of very high voltage power supply, are also a small tip radius (micrometers) of the initiating electrode, and a small (submillimeter) interelectrode distance.
The discharge initiated from the cathode is assumed to be based on the avalanche multiplication of electrons emitted from the cathode, when liquid is submitted to electric fields of the order of GV·m^{-1}. Electron flux from the cathode increases according to the relation (2.5). Avalanche breakdown of liquids, similar to the Townsend breakdown of gas, was observed under uniform electric field in liquid Xe, Ar, He and N_2 [14]. The initiation of the breakdown is the only part, which can be accounted for a pure electronic process (field emission, impact ionization) occurring near the electrode emission point (near a tiny surface bulge with sub-micrometer dimensions).
At weaker electric field strengths, the emitted electrons moving in the liquid cause its local superheating, expansion and bubble nucleation. The density of the substance consequently decreases to values at which the average free path of electrons is large enough for electrons to acquire the energy sufficient for collision ionization. Then avalanches are formed and avalanche-streamer conversion is observed by analogy with the discharge in gases. According to available experimental data the low voltage liquid conductivity has essentially no effect on the breakdown characteristics, and it is assumed that the role of the ion current is negligible. The electron autoemission from cathode plays the key role in the energy liberation and formation of the gas-phase nucleation centers. The microexplosive discharge initiation was observed near a negatively charged tip surface in liquefied gases, n-hexane, cyclohexane, and other liquids [12].
The discharge initiated from anode is assumed to be based on the electron emission from the liquid by tunnel transitions at electric fields >100 MV·m^{-1}. This 'semiconductor' approach approximates the liquid as a solid-state crystal with semiconductor properties [13]. Models of the liquid autoionization process on the anode are approximate, because character of the tunneling process and the classical formula for the image potential near the metal surface are rough (there is lack of a more precise model of the liquid interaction with the metal surface). The recent analysis resulted in the following expression for current density of electron emission [12]:

$$j = \frac{N_e E e^2 a^2}{2h\left[\ln\left(\frac{2E_i}{\tau}\right)-1\right]} e^{\left[\frac{-E_i}{Eea}\left(\ln\left(\frac{2E_i}{\tau}\right)-1\right)\right]} \qquad [\text{A·m}^{-2}], \qquad (2.14)$$

where E_i [eV] is the ionization energy in the liquid phase, E [V·m^{-1}] is the electric field strength, e [C] is the electron charge, a [m] is the spacing of liquid molecules, τ [eV] is the liquid valence band width, h [J·s] is the Planck constant, and N_e [m^{-1}] is the number of valence electrons in liquid unit volume. The

electron current density calculated for water (E_i = 8.76 eV, a = $3 \cdot 10^{-10}$ m, N_e =$1.3 \cdot 10^{29}$ m^{-3}, $\tau \approx 3$ eV) according to (2.14) is graphically depicted in the Figure 6 as a function of the electric field strength [12], which shows that the emission current density starts to be important at electric field values of the order of GV$\cdot$m^{-1}.
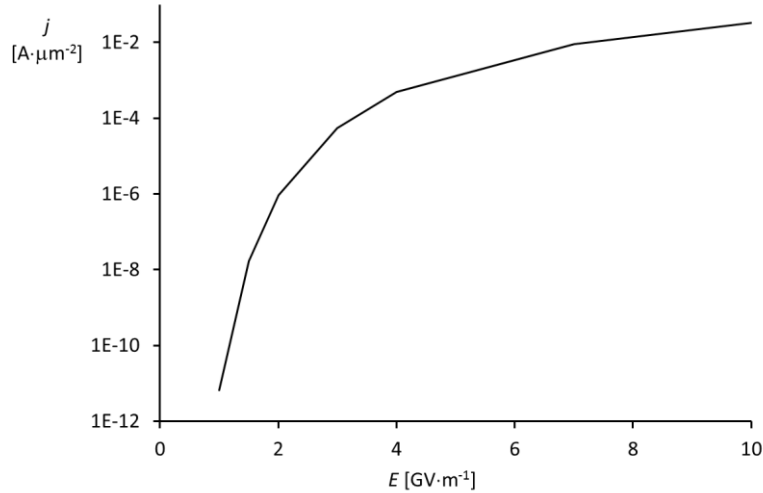
Figure 6 Electron ionization current density j for water as function of the electric field strength E.

Ionization liquid discharge initiation

The *ionization* liquid discharge initiation mechanism is, similarly as in the microexplosive mechanism, based on autoionization of liquid molecules (anode initiation) or collision ionization (cathode initiation) [12]. The difference is that the energy liberation, liquid-vapor phase transition, and shock wave generation are secondary processes, which are not necessary for the discharge initiation. The ionization processes occur at the density of liquid phase. The conditions for realization of this (ionization) discharge initiation mechanism are high electric field strengths (more than 1 GV$\cdot$m^{-1}) and short voltage pulses. Although the field strength is sufficient for ionization of liquid molecules, the exposure time is insufficient for the liquid-vapor phase transition. Therefore, this requires very restricting conditions in order to minimize probability of phase change, mainly small electrode gap distances (<mm), short pulsed voltages (~ns), purified, degassed and filtered liquids, and high hydrostatic pressures in the liquid.

The observed propagation velocity of the initial plasma with density of liquid water reaches 5000 km$\cdot$s^{-1} and it is similar to the velocity of streamer propagation in air [13]. The typical channel diameter is estimated as 50 – 100 µm. This yields the radial expansion velocity of the channel to be about 250 km$\cdot$s^{-1}. The formation of such a high density plasma channel in water is depicted in false colors in Figure 7. The next phenomenon causing a further local increase of electric field in water is dependence of water permittivity on electric field. Reduction in permittivity with increasing electric field intensity above 100 MV$\cdot$m^{-1} leads to next field enhancement by a positive feedback effect due to the continuity of electric displacement field εE. This finally results in significantly stronger local electric field at the sharp tip or a protrusion on an electrode [15].

9
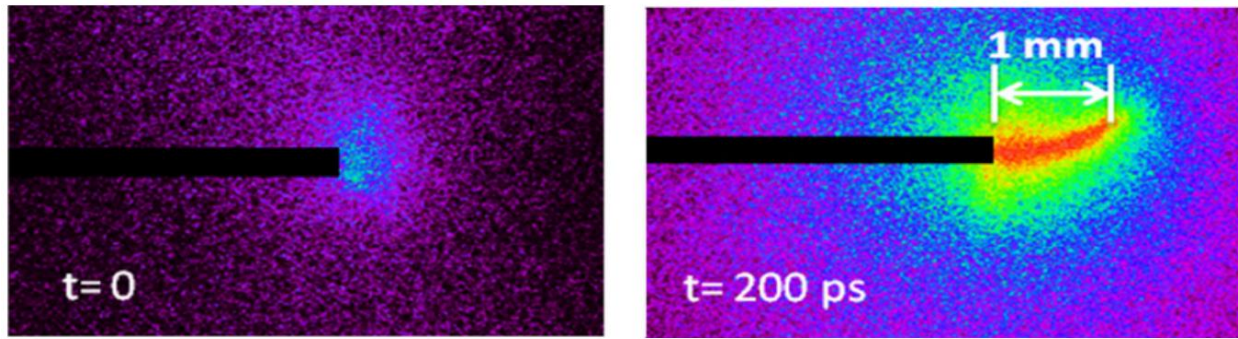
Figure 7 Velocity of plasma propagation in water (liquid phase); electrode voltage 220 kV with rise time 150 ps, streamer longitudinal growth rate ≈ 5000 km·s^{-1}. The inter-electrode distance was 4 mm, and the opposite grounded plate electrode diameter was 18 mm [13].

Electrostrictive liquid discharge initiation

This type of breakdown initiation in liquid is based on violation of liquid continuity in the vicinity of a sharp electrode (or bulge) due to the effective negative pressure caused by electrostrictive ponderomotive force pushing dielectric fluid to the regions with higher electric field. Electric discharge in gas phase is then realized. This volumetric force, which acts on a dielectric fluid containing free charges in a nonuniform electric field, is known as *Korteweg-Helmholtz (K-H)* force density [16]:

$$\vec{f} = qn_q\vec{E} - \frac{\varepsilon_0}{2}E^2\nabla\varepsilon_r + \frac{\varepsilon_0}{2}\nabla\left(E^2\rho\frac{\partial\varepsilon_r}{\partial\rho}\right) \ [\text{N·m}^{-3}], \tag{2.15}$$

where the first term is the force density acting on free charges with charge q [C] and number density n_q [m^{-3}], the second and third terms are volumetric density of the ponderomotive forces, ε_0 [F·m^{-1}] is the vacuum permittivity, ε_r [-] is the liquid relative permittivity, ρ [kg·m^{-3}] is the liquid density and E [V·m^{-1}] is electric field. The second term in equation (2.15) is associated with force acting on an inhomogeneous dielectric, and the third term corresponds to the ponderomotive force in a non-uniform electric field. If the liquid does not contain any free charges in the pre-breakdown stage, the first term disappears. For non-polar liquids, the dependence of the relative permittivity ε_r on the liquid density ρ is given by the *Clausius–Mossotti* equation [12]:

$$\rho\frac{\partial\varepsilon_r}{\partial\rho} = \frac{(\varepsilon_r+2)(\varepsilon_r-1)}{3}, \tag{2.16}$$

and for polar liquids it is approximately

$$\rho\frac{\partial\varepsilon_r}{\partial\rho} \approx \alpha\varepsilon_r, \tag{2.17}$$

where α is a coefficient of the order of unity. For water $\alpha \approx 1.5$ [17]. The K-H force density in non-polar liquids without free charges is using (2.16) given by

$$\vec{f} = -\frac{\varepsilon_0}{2}\left[E^2\nabla\varepsilon_r - \frac{(\varepsilon_r+2)(\varepsilon_r-1)}{3}\nabla E^2\right], \tag{2.18}$$

10

and in polar liquids using (2.17) it is

$$\vec{f} = -\frac{\varepsilon_0}{2}[E^2 \nabla \varepsilon_r - \alpha \varepsilon_r \nabla E^2]. \tag{2.19}$$

The dynamic of dielectric compressible liquid in a pulsed inhomogeneous electric field is described by the standard system of equations: continuity equation (conservation of mass), and conservation of momentum [16]:

$$\frac{d\rho}{dt} + \rho \nabla \cdot \vec{u} = 0, \tag{2.20}$$

$$\rho \left[\frac{\partial \vec{u}}{\partial t} + (\vec{u} \cdot \nabla)\vec{u} \right] = \mu_d \nabla^2 \vec{u} + \left[\frac{1}{3}\mu_d + \mu_v \right] \nabla(\nabla \cdot \vec{u}) - \nabla p + \vec{f}, \tag{2.21}$$

where $\vec{u}$ [m·s^{-1}] is the liquid velocity, μ_d [Pa·s] is the liquid dynamic viscosity, μ_v [Pa·s] is the liquid volume viscosity, p [Pa] is hydrostatic pressure and $\vec{f}$ represents the force density given by (2.18) or (2.19). The left side of the equation (2.21) describes the liquid acceleration, and is composed of time dependent and convective effects. The right side consists of summation of viscosity, gradient of the liquid pressure and the body force density. Since $\rho \frac{\partial \varepsilon}{\partial \rho} \approx const.$, the last two terms on the right side of (2.21) can be rewritten in the case of homogeneous liquid ($\nabla \varepsilon_r = 0$) as

$$-\nabla p + \vec{f} = -\nabla \left(p - \frac{\alpha \varepsilon_0 \varepsilon_r}{2} E^2 \right) = -\nabla(p + p_e) = -\nabla p_{tot}. \tag{2.22}$$

This substitution shows that the force density $\vec{f}$ can be replaced by an equivalent pressure p_e (electrostrictive pressure) with the same effect on liquid [18]. The value of the pressure p_e is always negative. The total effect of the hydrostatic and electrostrictive pressure on the liquid is given by the total pressure p_{tot}. Figure 8 depicts calculated distribution of electrostrictive pressure around a cylindrical needle electrode (needle-plate configuration) with semielipsoidal tip (tip radius of 5 µm) and with the needle potential of 7 kV.
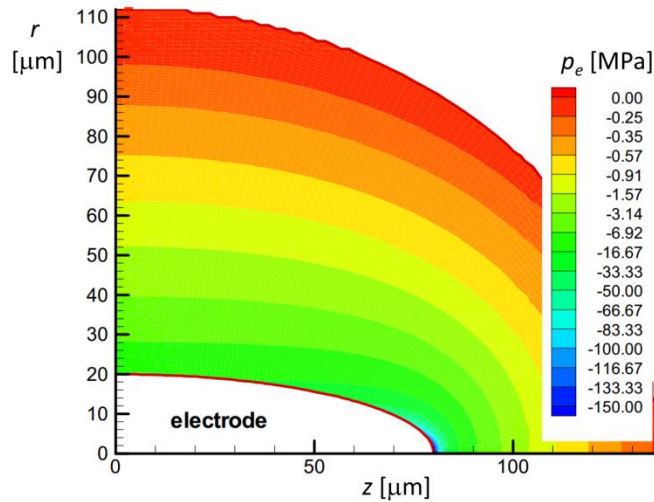
Figure 8 Contours of the electrostrictive pressure around a cylindrical needle electrode **[17]**.

In the moment when high voltage with rise time short enough is applied to the needle electrode, a negative electrostrictive pressure around this cylindrical needle electrode is established, while the hydrostatic pressure remains nearly constant. If $|p_e| \gg |p|$, then $\nabla p_{tot} \approx \nabla p_e$, and the liquid is accelerated toward the needle tip (in the direction of electric field gradient) in agreement with the equation (2.21). If then the applied voltage remains constant and the liquid is "irrupturable", the system will reach its equilibrium state after some time. The gradient of the hydrostatic pressure will compensate the gradient of the electrostrictive pressure, and $\nabla p_{tot} = 0$. However, in the equilibrium state, the gradient of the liquid density exists - with the same direction as the gradient of hydrostatic pressure given by the liquid equation of state. When the voltage at the needle electrode falls to zero rapidly enough, the electrostrictive pressure disappears and only the gradient of hydrostatic pressure remains; $\nabla p_{tot} = \nabla p$. This is also a non-equilibrium state, which is followed by emission of pressure wave propagating from the electrode tip. Experiments depicting this phenomenon were published in [19]. Schlieren images of the high-voltage electrode region in distilled water (1.0 µS·cm^{-1}) are depicted in the Figure 9.
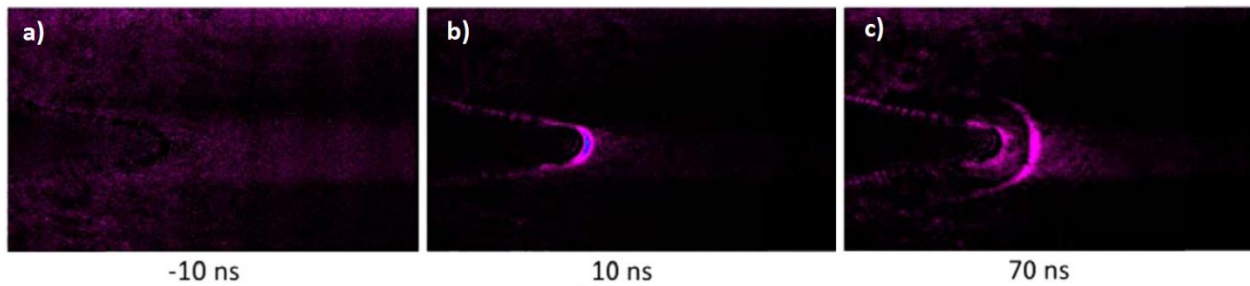
**Figure 9** Schlieren images of the high-voltage electrode region in water, the image sizes were of 750×500 µm; a) zero voltage at the electrode, liquid is homogeneous, b) +22.4 kV high voltage pulse with 10 ns duration applied to the electrode, increased liquid density on the electrode surface, c) zero voltage at the electrode, shock wave expands from the electrode surface **[19]**.

In these experiments there were used positive nanosecond pulses with 11.2 kV pulse amplitude in 50 Ω coaxial cable (i.e. 22.4 kV on the high-voltage electrode tip due to pulse reflection), 10 ns pulse duration, 3 ns rise time and 4 ns fall time. The high-voltage needle electrode was 1 mm thick tungsten wire sharpened to the radius of 35 µm, and placed 3 mm apart 18 mm diameter copper grounded electrode. The applied voltage 11.2 kV was below the breakdown voltage (i.e., the discharge was never ignited). In accord with the model, formation of a region with density perturbation near the surface of the high-voltage electrode was observed.

The stretching electrostrictive pressure, which is associated with the action of the volumetric forces (2.18) or (2.19), can lead to formation of micro ruptures (cavitation) in the fluid, when the tensile strength of the liquid is exceeded. Cavitation means creating of a new surface in a liquid volume. Despite the theoretical tensile strength which liquid water should withstand, is more than −1 GPa, in practice, the experimental limit stretching tension is much smaller [20]. The limiting mechanical tension that liquid water can sustain before cavitation occurs, was found to be −26 MPa at 0 °C and it monotonically changes to −17 MPa at 80 °C [21]. The reason for such significant decrease of the liquid tensile strength is a permanent existence of inception bubbles - cavities containing non-condensable gases or liquid vapor. The basic types of inception bubbles in water are depicted in the Figure 10. Tap unfiltered water commonly contain freely floating air bubbles and gas pockets in crevices in motes with dimensions of the order of 10 µm [22]. Maximum mechanical stress which they can sustain is less than −100 kPa. On the other hand, in carefully filtered water, which is not screened from the radioactive background (or cosmic rays), the main inception bubbles are temporary vapor bubbles with dimensions of the order of 10 nm.

These vapor bubbles are created by microexplosions of locally overheated liquid regions, where energy of energetic particles is deposited.
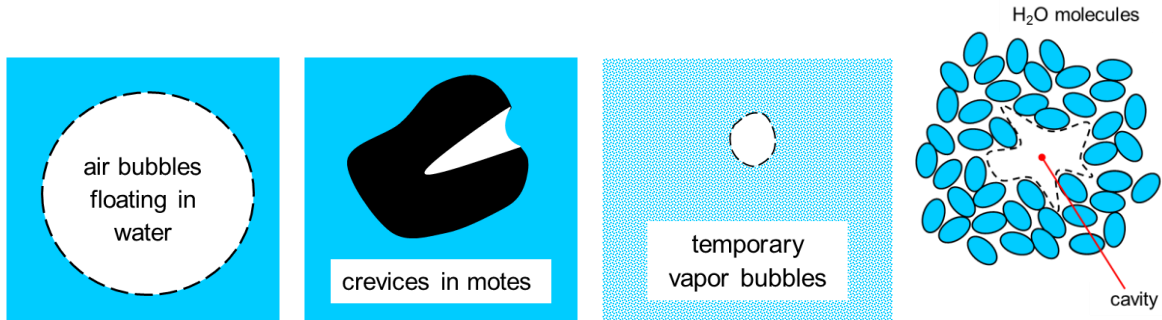
Figure 10 Basic types of inception bubble in water. Air bubbles freely floating in bulk liquid and crevices in motes containing gas are common in tap water. Carefully filtered water may contain temporary vapor bubbles produced by ionizing radiation or cavities spontaneously created by the liquid molecules fluctuations.

This phenomenon is utilized in bubble chambers used as particle detectors [23]. Maximum mechanical stress which filtered unscreened water can sustain, is of the order of MPa. Interesting is a cumulative and memory effect: water irradiated 30 minutes by 14 MeV neutrons with average rate 10^8 s^{-1} exhibited half tensile strength in comparison with its initial strength. When the neutron radiator had been removed, it took tens of minutes to restore the initial tensile strength [24]. In experiments with cosmic rays it was even several hours [25].

Fluctuations of the liquid molecules start to be important in carefully filtered water screened from any energetic particles. The nucleation sites have dimensions comparable with intermolecular distance (10^{-10} m) in this case, and the liquid should exhibit the maximum theoretical tensile strength of the order of -1 GPa [20] at normal temperature.

Free floating bubbles containing a mixture of both water vapor and gases that are dissolved in liquid are unstable for two reasons. Firstly, buoyancy can remove them from the liquid. It was shown that water, which had been left standing for several hours, contained only bubbles with radii < 5 μm [22]. Smaller bubbles are not affected by buoyancy, because liquid currents and Brownian motion become more important. Secondly, contractual force of the tension in bubble wall can cause the bubble dissolves away. Let us consider the bubble of the radius R_B shown in the Figure 11. There is an internal pressure $p_v + p_g$, where p_v is the pressure of liquid vapor, and p_g is the pressure of gas. The pressure within the bubble at rest is greater than the pressure in the liquid outside the bubble due to liquid surface tension.
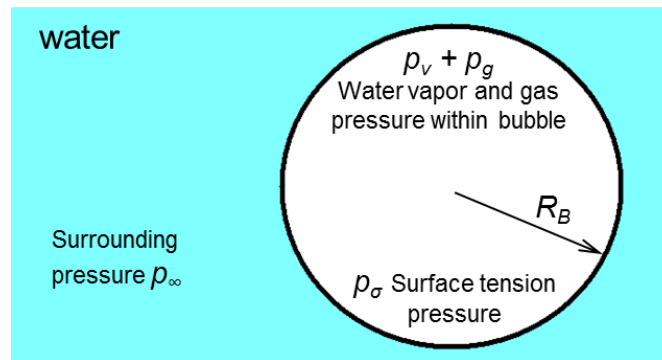
Figure 11 On the pressure balance of a static gas bubble in water.

If the surrounding (hydrostatic) pressure outside the bubble is p_∞, then in equilibrium state must be

$$p_v + p_g = p_\infty + p_\sigma, \tag{2.23}$$

where p_σ is the surface tension pressure

$$p_\sigma = \frac{2\sigma}{R_B}, \tag{2.24}$$

which is given by the liquid surface tension σ [N·m^{-1}] and the radius of the bubble R_B [m], whose value is positive for a convex surface as seen from the liquid. Hence, there must be an inequality of the gas pressure in a stable bubble and the hydrostatic pressure around it: $p_v + p_g > p_\infty$. The liquid vapor pressure is determined by the liquid temperature only. In the case of water it is $p_v \approx 2.34$ kPa at 20 °C. The gas pressure p_g is determined by the amount of the gas dissolved in the liquid. If the liquid is not supersaturated with the dissolved gas (gas inside the bubble is not in equilibrium with gas dissolved in the liquid), the equation (2.23) cannot be fulfilled permanently, because the gas will pass from the bubble interior to the liquid and the bubble will dissolve.

Nevertheless, static inception bubbles do exist, and two models of bubble stabilization are known. These are referred to as the variably permeable skin model and the crevice model [22].

The *variably permeable skin model* is based on existence of an elastic organic surface skin which, although initially permeable to gas, becomes impermeable as the concentration of organic molecules increases in the contracting bubble wall. Thus, compressed gas inside bubbles cannot penetrate through the bubble boundary, and the pressure p_g can be for a long time greater than the corresponding equilibrium gas pressure. However, if the liquid is subjected to tension, the bubbles are free to grow by an influx of gas previously dissolved in the liquid. Free-floating bubbles stabilized in some range of pressures were found even in distilled water; their radii range from 1 nm to 1 μm [22].

If the liquid pressure is reduced to negative values ($p_\infty < 0$), it can counteract the pressing effect of surface tension. When the bubble radius is larger than some critical radius (critical bubble), the surface tension pressure p_σ is so small, that the pressure balance across the bubble wall cannot be maintained: $p_\infty < p_v + p_g - p_\sigma$. Then the bubble will grow explosively. Temporary development of bubble radius is determined in the simplest form by the *Rayleigh-Plesset (R-P)* equation [22]:

$$\rho\left(R_B\ddot{R}_B + \frac{3}{2}\dot{R}_B^2\right) = p_v + p_g - \left(\frac{2\sigma}{R_B} + \frac{4\mu_d}{R_B}\dot{R}_B + p_\infty\right), \tag{2.25}$$

where ρ [kg·m^{-3}] is the liquid density, μ_d [Pa·s] is the liquid dynamic viscosity and p_∞ [Pa] is pressure far from the bubble.

Figure 12 illustrates the second way (crevice model) of bubble stabilization by a *gas pockets* contained within small-angled *crevices* in imperfectly wetted hydrophobic solids (motes), where the contact angle between liquid and solid is $\theta > 90°$. The hydrophobicity is ensured either by the nature of the solid material itself, or by hydrophobic organic contaminants, which are adsorbed on the solid surface. If the liquid surface is concave as seen from the liquid (Figure 12a), the radius of curvature is negative, therefore, from equation (2.24), $p_\sigma < 0$, which thus acts to reduce the gas pressure within the crevice: $p_v + p_g < p_\infty$. The dissolved gas leaves the liquid and enters the bubble; hence the liquid surface advances out of the crevice. In Figure 12b, the meniscus and the crevice geometries are such that radius of curvature of the liquid surface is infinite, and according to equation (2.24) the surface tension pressure $p_\sigma = 0$. The pressure within the gas pocket will equal the pressure in the liquid: $p_v + p_g = p_\infty$. Figure 12c illustrates a situation, when the radius of curvature of the liquid surface is positive (the surface is convex as seen from the liquid). The liquid surface tension will act to increase the pressure within the gas pocket above that in the liquid: $p_v + p_g > p_\infty$. The accumulated gas leaves the crevice and enters the

surrounding liquid; hence the gas surface recedes into the crevice. Enabling the meniscus to take a concave form is, therefore, the mechanism, how a crevice in a solid can stabilize a gas pocket against dissolution without need of saturation of the liquid by a gas.

a)   b)   c)
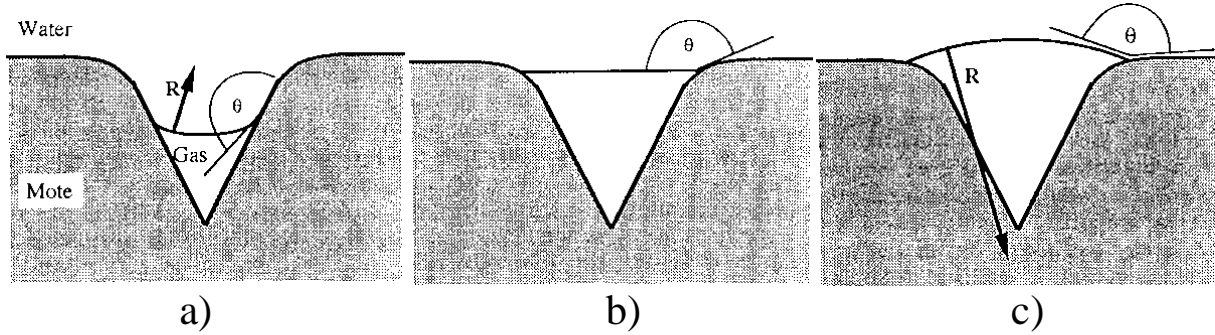
Figure 12 Schematic of a gas-pocket within a crevice in a solid (mote), illustrating the radii of curvatures R that may be found: a) negative; b) infinite; c) positive. The contact angle θ of the meniscus against the solid material is shown **[22]**.

Such a crevice can generate free-floating bubbles, which pass into the liquid volume. If the liquid pressure is reduced slightly, the liquid surface in Figure 12a will simply become less concave. However, if the pressure reduction is considerable, the bubble wall becomes convex (i.e. the radius of curvature of the liquid surface becomes positive), and the liquid recedes above the cavity. On reaching the top of the crevice, a bubble is pinched off in the space above the gas pocket (Figure 13). The liquid is cavitated. Subsequent temporal development of emitted bubble is determined by the R-P equation (2.25).
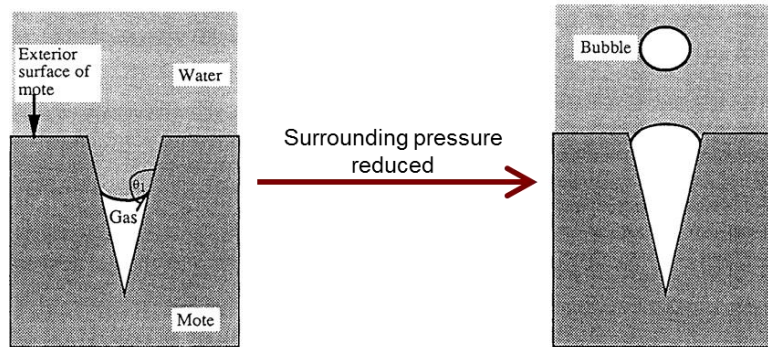
Figure 13 The figure illustrates the situation at the top of the crevice, where a free-floating bubble may be nucleated **[22]**.

When stretching electrostrictive pressure ruptures a liquid, expanding bubbles and gas from crevices in motes (or in electrode surface) naturally appear in region with strong electric field. These low-density cavities effectively facilitate electron avalanche sufficient to initiate breakdown [7].

Electrothermal liquid discharge initiation

The *electrothermal* liquid discharge initiation mechanism is based on boiling of a conductive liquid. Strong electric filed in liquid induces conduction current which heats up the liquid in the near-electrode or

near diaphragm regions with maximum electric field strength. Boiling of the liquid accompanied by creation of vapor gas cavities is followed by gas breakdown inside the cavities and, hence, formation of a plasma channel [12].

If heating of the liquid is so fast that convection flow and the liquid thermal conductivity is insignificant at the time scale of the heating, temperature of the liquid rises with time t as

$$\delta T = \int_0^t \frac{M\sigma_c E^2}{\rho c_{p,m}} dt \qquad [\text{K}], \qquad (2.26)$$

where M [kg·mol^{-1}] is the liquid molar mass, σ_c [S·m^{-1}] is the liquid conductivity, E [V·m^{-1}] is the electric field, ρ [kg·m^{-3}] is the liquid density and $c_{p,m}$ [J·K^{-1}·mol^{-1}] is the liquid molar heat capacity at constant pressure. Conductivity of a water solution is generally temperature dependent; it changes approximately of 2 %·K^{-1} in the temperature range of 283-303 K. A second order polynomial approximation must be used at larger temperature change [26].

Boiling of the liquid may be enhanced by presence of mentioned inception floating bubbles and gas pockets in motes. In accordance with equations (2.23) and (2.24) it happens when

$$p_v + p_g > p_\infty + \frac{2\sigma}{R_B}. \qquad (2.27)$$

Here, pressure of the liquid vapor p_v equals to the liquid saturation vapor pressure p_s, which nonlinearly depends on the liquid temperature only. The value of p_s (≈ 2.34 kPa at 20 °C) is negligible in comparison with the value of p_g (101 kPa) in water at atmospheric pressure; it starts to be important at temperatures near water boiling point [27]. Influence of water surface tension is also negligible at radii of inception bubbles of the order of tens of micrometers or greater in comparison with hydrostatic pressure at normal pressure (for $\sigma \approx 70$ mN·m and $R_B = 50$ μm the equation (2.24) gives $p_\sigma \approx 2.8$ kPa). This is the reason, why water boiling temperature is ≈ 100 °C at normal pressure. However, the situation is different in carefully filtered degased water. The critical saturation pressure p_{sc} is the liquid vapor pressure at the critical temperature, which is $p_{sc} = 22.06$ MPa at $T_c = 647.096$ K for water. The radius of inception bubbles which are able to withstand such high vapor pressure is from (2.24) $R_{Bmin} = 2\sigma / p_{sc} = 6.35$ nm, i.e. bubbles with radii R_{Bmin} are the smallest inception bubbles, which can work as boiling nuclei in water. Therefore, cavities spontaneously created by the liquid molecules fluctuations may be significant at some degree of the liquid superheating. The Dering–Volmer formula gives the bubble nucleation rate in unit volume of a superheated liquid [28] [20] [12]:

$$s = N \sqrt{\frac{2\sigma}{\pi m_m}} e^{-\frac{W^* + q'}{kT}} \qquad [\text{m}^{-3} \cdot \text{s}^{-1}], \qquad (2.28)$$

where N [m^{-3}] is the number density of the liquid molecules, m_m [kg] is the mass of the liquid molecule, k [J·K^{-1}] is the Boltzmann constant, T [K] is temperature of the superheated liquid, q' [J] is the vaporization heat of a single molecule, and

$$W^* = \frac{16\pi\sigma^3}{3(p_\infty - p_s)^2}, \qquad [\text{J}], \qquad (2.29)$$

is a work of formation of a critical bubble (bubble, where inequality (2.27) is obeyed) under hydrostatic pressure p_∞ [Pa]. In the body of a pure liquid completely isolated from any external radiation, the issue is reduced to the probability that the stochastic nature of the thermal motions of the molecules would lead to a local energy perturbation of magnitude $W^* + q'$. The equation (2.28) gives meaningful results only when temperature-dependent values of water surface tension and saturation pressure are used. Dependence of water saturation vapor pressure on temperature in the range between water triple point and T_c can be estimated by [29]:

$$p_s \approx p_{sc} e^{\frac{T_c}{T}(a_1\tau + a_2\tau^{1.5} + a_3\tau^3 + a_4\tau^{3.5} + a_5\tau^4 + a_6\tau^{7.5})} \qquad \text{[Pa]}, \qquad (2.30)$$

where $\tau = 1\text{-}T/T_c$, and where parameters a_1 to a_6 acquire the following values: $a_1 = -7.85823$, $a_2 = +1.83991$, $a_3 = -11.7811$, $a_4 = +22.6705$, $a_5 = -15.9393$, $a_6 = +1.77516$.
Interpolating equation of dependence of water surface tension on temperature is given by [30]:

$$\sigma \approx B(1 + b\tau)\tau^{\alpha} \qquad \text{[N·m}^{-1}\text{]}, \qquad (2.31)$$

where $B = 235.8 \cdot 10^{-3}$ N·m^{-1}, $b = -0.625$, $\alpha = 1.256$ and $T_c = 647.096$ K is the water critical temperature. Dependence of the bubble nucleation rate on temperature calculated by (2.28) using (2.29), (2.30) and (2.31) is plotted in the Figure 14. The nucleation rate is uninteresting at temperatures below 575 K. At higher temperatures the nucleation rate sharply rises; at temperatures higher than 591 K it is comparable with water molecule number density N ($\approx 3.3 \cdot 10^{28}$ m^{-3}). For example, probability of bubble nucleation reaches certainty at $T > 582$ K in front of a tip electrode with radius of 1 mm (volume of surrounding heated water is of the order of 1 mm^3) at time scale of 10 ns.
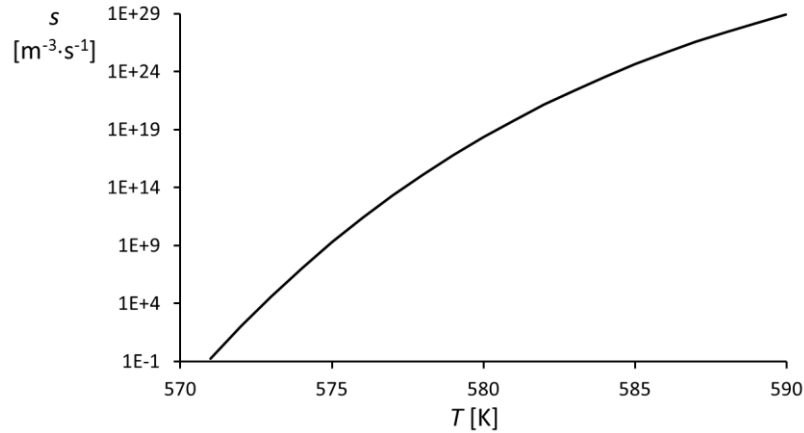
Figure 14 Dependence of the bubble nucleation rate on temperature according to equation (2.28).

However, vapor inside bubbles produced in superheated liquid may not necessarily facilitate breakdown of the bubbles, because value of the pressure p_s may reach several MPa. High density of the vapor inside the bubbles (with high electron collision frequency) can prevent electron avalanche to develop. Breakdown in water vapor at low pressures and at large gaps is well understood. Paschen curves for gaps greater than 5 mm and for tap and bi-distilled water were measured in [31]. On the other hand, the breakdown phenomenon in microgaps, which may be the most important for a liquid breakdown initiation, has not yet been sufficiently explored. The breakdown field strength, defined as the ratio of the breakdown voltage and the gap size, strongly depends on the inter-electrode separation. For gaps less than 5 μm, the breakdown phenomena are attributed to the ion-enhanced field emission from the cathode (by lowering of potential barrier for cathode-electrons when positive ion approaches the cathode surface), and are accompanied by a rapid fall of the breakdown voltage [32]. Violations of the Paschen law take place for that pd values, where the electron mean free path is comparable with the gap size. Figure 15 illustrates firstly a weak dependence of the breakdown field strength on the pressure for the gaps of the order of a few micrometers, and secondly the rapid fall of the breakdown voltage of smaller gaps; e.g. at the pressure of 10^3 Torr and the gap of 3 μm the breakdown voltage is of 165 V, but at the same pressure and the gap of 0.5 μm the breakdown voltage falls to 33 V.
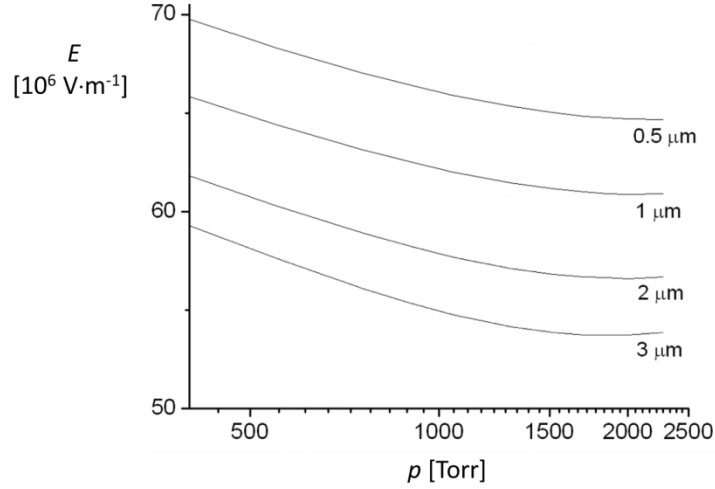
Figure 15 The breakdown field strength of water vapor as a function of the gas pressure for the gap sizes from 0.5 to 3 μm. The plot was theoretically derived in **[32]**.
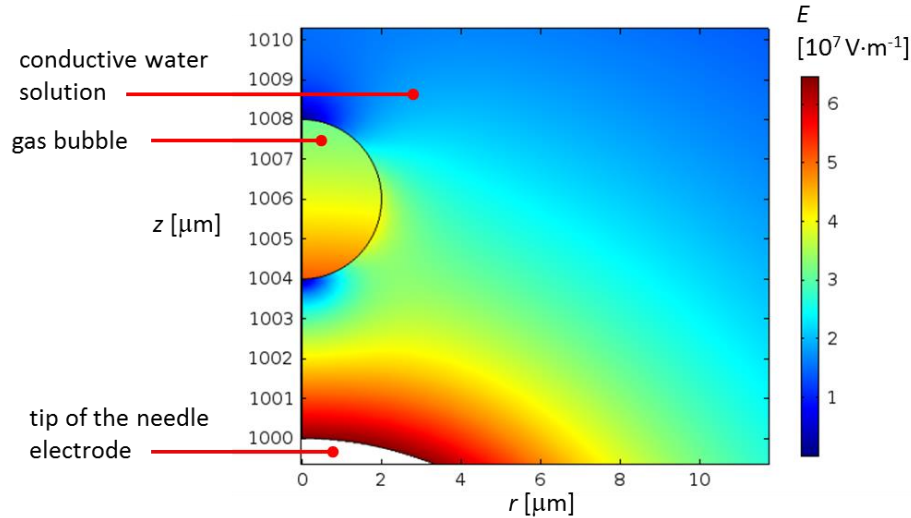
Figure 16 Stationary simulation of electric field inside and around dielectric gas bubble in conductive water solution in the vicinity of the tip of needle electrode (needle-plate configuration). The simulation was performed in cylindrical coordinates; the geometry was symmetrical around the axis *z*. Radius of the tip electrode was 8 μm, distance between the needle and the plane electrode was 1 mm and voltage between the electrodes was 2 kV. The simulation was performed using Comsol Multiphysics software.

In the simulation of electric field distribution in conductive water and in a bubble above the tip of needle electrode, shown in the Figure 16, so high voltage on this electrode was used that the electric field inside the bubble was comparable with values of breakdown voltage in the Figure 15. Electric field in the dielectric gas microbubble in conductive water solution is of the same order as the field in unperturbed surrounding liquid, as a consequence of the electric boundary conditions [33]. Tangential components of electric field must equal on both sides of the bubble boundary, if the temporal change of tangential

18

magnetic field on the boundary is negligible: $\partial B_{\parallel}/\partial t = 0$. Thus, the electric fields on the bubble equator (in the Figure 16) in z direction at the water and bubble side are $E_{\parallel e \text{ water}} = E_{\parallel e \text{ bubble}} \approx 40$ MV·m^{-1}. Normal current density has to equal on both sides of the bubble boundary, as the equation of continuity under static field requires: $\nabla \cdot \vec{j} = 0$. Resulting equality $j_{\perp e \text{ water}} = j_{\perp e \text{ bubble}} = 0$ (steam in the bubble is good insulator) determines normal electric field on the bubble equator to be zero $E_{\perp e \text{ water}} = E_{\perp e \text{ bubble}} = 0$. Similarly, normal electric field on the bubble poles (on the axis z) in water has to be zero: $E_{\perp p \text{ water}} = 0$. Normal electric field inside the bubble above the bottom pole, $E_{\perp p \text{ bubble}} \approx 50$ MV·m^{-1}, is then generated by the induced boundary surface charge $\sigma_q = \varepsilon_0 E_{\perp p \text{ bubble}} \approx 4.5 \cdot 10^{-4}$ C·m^{-2}.

## Bubble liquid discharge initiation

In the case of *bubble mechanism*, the discharge is ignited in the gas bubbles that already exist on the electrodes and in the liquid before field application, and basically this is already described Townsend or streamer gas breakdown. Ionization inside gas bubbles leads to their deformation and creation of primary plasma channels in the surrounding liquid. This discharge initiation mechanism is most probably realized in non-degassed liquids, where gas bubbles or gas pockets on electrode surface are common phenomenon (see Figure 12). One of the reasons for bubble occurrence is extraction of the gas from crevices and pores on the electrode surface under the action of electrostatic forces, which elongate bubbles, while their volumes remain constant. Due to the force densities (2.18) or (2.19), and electrostatic force acting on the bubble boundary [34], liquid overflows from weaker to stronger field regions. In the case of geometry in the Figure 16 it flows from the bubble poles to its equator, and, therefore, pressure near the bubble equator increases and it decreases at the bubble poles. If the field on the bubble boundary is redistributed due to the electrical conduction of the liquid, the bubble elongation will reach its equilibrium state after some time dependent on the dielectric relaxation time

$$\tau = \frac{\varepsilon}{\sigma_c} \qquad \text{[s]}, \qquad\qquad (2.32)$$

given by the ratio of the liquid permittivity ε [F·m^{-1}] and conductivity σ_c [S·m^{-1}]. The relaxation time of distilled water at normal temperature with conductivity of 500 µS·m^{-1} is of 1.4 µs. Figure 17 shows shadow photos of microbubbles with different radii ranging from 20 to 40 µm on the cathode surface before and 4 µs after voltage application [12]. The bubbles elongate in the direction of the electric field by a factor of 1.5–2 relative to the initial size, and flatten in the transverse direction. The bubbles divide in two parts or even detach from the electrode surface. The detachment of bubbles from the electrode surface arises in 15–20 µs. Similarly as in the case of the bubble in the Figure 16, electric field in bubbles on the electrode surface is of the same order as that in the surrounding liquid. Measurements of breakdown electric field in air microgaps were published in [35]; the found dependence of the breakdown electric field on the gap size is plotted in the Figure 18. The material used for the electrodes was deposited thin film of gold (with material work of 5 eV). For bubbles larger than 10 µm, the breakdown data approach the air Paschen curve, but at gaps below 10 µm the main cause of breakdown has to be the field emission of electrons. The breakdown field strength in sub-micrometer air gaps starts to be comparable with the field strength required for the initiation of the liquid ionization breakdown.
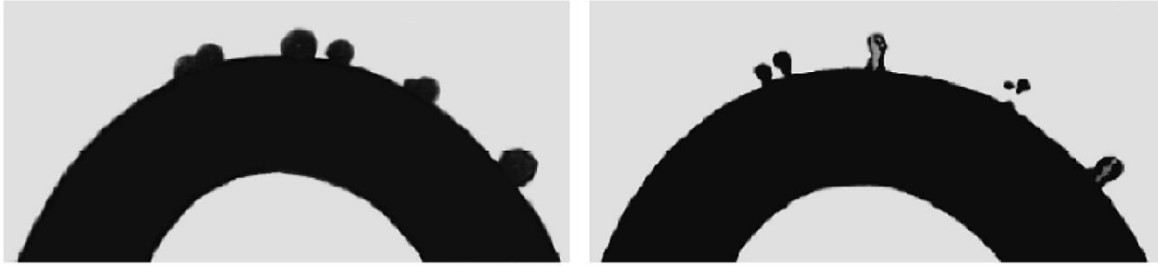
Figure 17 Bubbles on the cathode surface before (left) and 4μs after field application (right). The bubbles were generated as a result of pulsed heating of an electrode in the form of a U-shaped nichrome wire 0.2 mm in diameter with a bend radius of 0.5 mm. The maximum electric field (where the bubbles were located) was 30 MV·m^{-1}. The bubble elongation, perturbations on the bubble surface, and the bubble detachment are seen in the right part of the figure **[12]**.
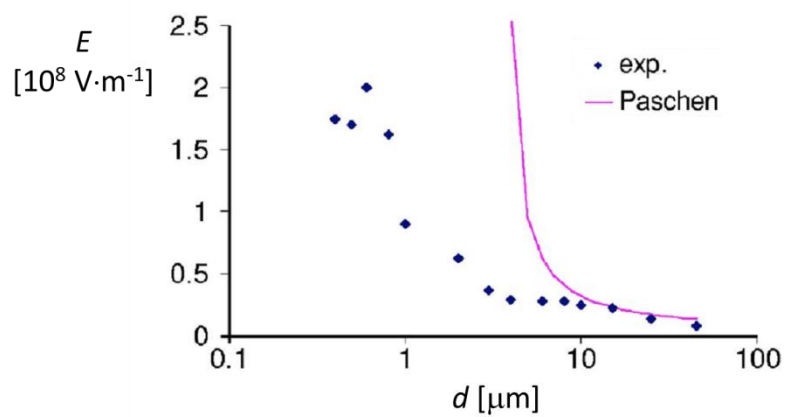
Figure 18 Breakdown electric field in air at atmospheric pressure as a function of electrode separation *d*. The dots are experimental results; the pink curve represents breakdown electric field according to the Paschen's law **[35]**.

3. Propagation of plasma channel in water

Propagation of plasma ignited on the surface of initiating electrode toward the opposite electrode may be realized in several different forms, most often as plasma streamers. The term "streamer" has been taken over from streamers in gases, because, similarly as in gases, the conductive streamers in liquids act as equipotential extensions of the electrode into the liquid [36]. Mechanism of the streamer propagation depends especially on the initiation electrode polarity, on the liquid conductivity and on the electric field near the initiating electrode. Low current stagnating or propagating electric discharges in liquids (not sparks between electrodes) are generally called ***corona-like discharges***. Since all the next article deals with corona-like discharges only, the term discharge is often used instead of corona-like discharge for simplicity. The next two sub-chapters (Chap. 3.1 and 3.2) summarize basic characteristics of corona-like discharges at both polarities.

3.1 Positive initiation electrode

Elongation of bubbles in the cathode direction

This type of propagation is the slowest one and arises from bubbles, in which the gas discharge has been ignited. After breakdown a constricted glow-like discharge in the bubble is observed. Such bubbles elongate from the spot, where the gas plasma attaches to the bubble wall. Experiments with bubbles filled with different gases in tap water with conductivity of 14.2 mS·m^{-1} were performed in [37]. The bubbles diameter was as large as a few millimeters and applied voltage of 15 kV was used. In many cases, the rotational temperature T_r was considered to be in equilibrium with the gas (kinetic) temperature T_g. From the analysis of OH bands emitted by bubbles filled with rare gases (He, Ar) it was suggested that the gas temperature T_g increased up to 3000K. Experiments with water solution of NaCl revealed that the rotational temperature of N_2 is of the same order of magnitude ($T_r = 1000\pm100$ K) [38]. The cathode directed elongation can be explained by the plasma heating process and evaporation of the bubble wall [39]. The surrounding water (conductive solution) as a resistive medium causes a limitation of the current. Therefore, the bubble elongation velocity is significantly dependent on the liquid conductivity (demonstrated in the experimental part in the next chapter).

It is worth mentioning the basic characteristics of discharges between metal pin anode and water cathode, which are analogous to the discharges in bubbles. For shutter opening times less than 100 μs the constricted contact points of the filamentary plasma dancing on the water surface are visible (gap 5 mm, current 20–140 mA) for both distilled water and electrolyte solutions [40]. Measurements performed at discharge current of 50 mA near water cathode revealed rotational temperature of N_2 to be $T_r = 2700\pm300$ K, and was nearly independent on the current changes. The result was similar when NaCl solution with conductivity of 1 S·m^{-1} as the liquid cathode was used. Moreover, the temperature T_r was decreasing at higher conductivities. Electron temperatures at the same current were determined to be $T_e = 6000$ K with distilled water cathode, and 6800 K with NaCl water solution (1.55 S·m^{-1}) cathode. Electron density was determined to lie between 10^{18}-10^{20} m^{-3} at the discharge current interval of 20-80 mA with different aqueous solutions (NaCl, HCl, HNO$_3$, H$_2$SO$_4$) [40] [41] [42] [43] [44].

Secondary electron emission coefficient of water and solutions is typically two to three orders of magnitude smaller than that of metal electrodes. Hence, relatively high cathode voltage drop of 760 V was measured at 50 mA with distilled water cathode, and 460 V with NaCl solution cathode (13.4 mS·m^{-1}) [40]. The thickness of the cathode dark space is of the order of 0.1 mm [42]. For comparison, in metal–metal glow discharges at atmospheric pressure the cathode drop for air is 300V with an iron cathode [45]. Glow discharges at atmospheric pressure are normally unstable; they are predisposed to glow-arc transition. Therefore, their operation requires stabilization techniques [46].
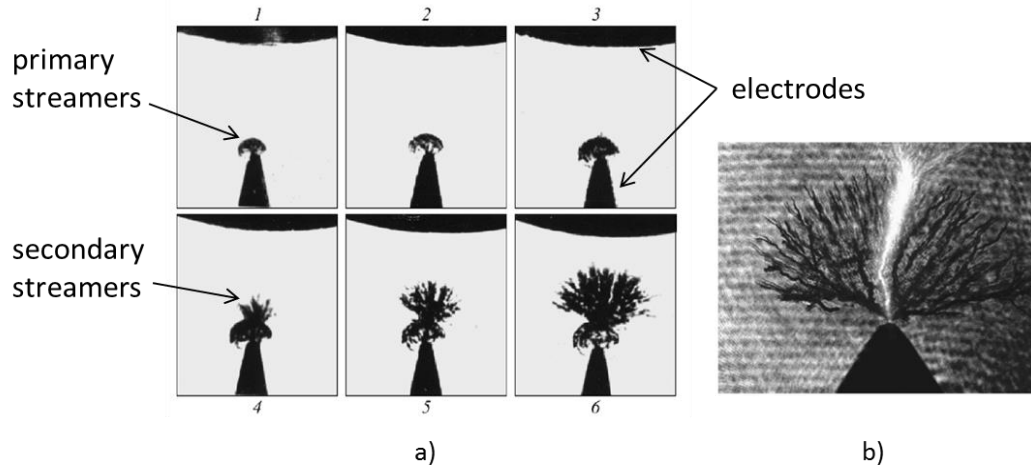
Figure 19 a) Fast laser schlieren photographs of the electric discharge from the anode in distilled water. The distance between electrodes was 2 mm, the frame exposition was 5 ns and the anode voltage was 27kV (field strength of 130 MV·m^{-1} near the tip electrode). The time interval between the first and second frame was 25 ns, and between other frames it was 10 ns [12]; **b)** A detailed schlieren photograph of anode primary streamers with bright stem of developed secondary streamers. Used voltage was 18 kV, radius of the tip electrode was 50 μm and the anode-cathode gap was 20 mm. The secondary streamer outshines the shadow image backlight illumination [47].

Primary streamers

The non-luminous *primary streamers* are often the early stadium of plasma propagation in water, which can, but need not start to propagate from an initial gas bubble with plasma streamers inside. The launch of primary streamers is triggered, when local electric field is of the order of 100 MV·m^{-1} [47]. Propagation of the primary streamers is accompanied by a phase transition, occurrence of microbubbles, and their hydrodynamic expansion. Primary discharges have hemispherical bush-like appearance, where the edges of the individual streamers can be clearly resolved (their channel diameters were measured to be 3-10 μm [48]), and propagate along radial directions at relatively low velocities (often subsonic, but some may reach even several kilometers per second) producing spherical shockwaves. Therefore, the initial disturbance has approximately spherical shape. Adjacent electric field may initiate next discharges or gas bubbles in the liquid and thus elongate the streamers plasma channel. The process stops when the breakdown voltage of the gaseous channel becomes higher than the voltage along the channel or when the electric field at the active tip of one of the streamer becomes so high that *secondary streamers* can be formed [49] [47] [12]. This process is illustrated in the Figure 19a, where the first and the second frames show primary discharge growing from the electrode tip. Propagation velocity of the primary streamers toward the cathode was 3 km·s^{-1}. The shadow of the generated shockwave is visible as a circle around the primary streamers. The Figure 19b depicts a more detail photo of individual primary streamers. The primary discharge propagation may be composed of more than one step [50]. After the semi-spherical bush-like structure was observed, most of the filamentary channels vanish except of a few channels. The survived channels keep elongating with a constant speed of 2 km·s^{-1} until a new bush-like structure develops resulting in formation of a tree-like structure. It is called the second step of primary streamer propagation, which cannot be seen in the Figure 19, but can be found in [50].

Secondary streamers

The secondary streamers are much more luminous as it can be seen in the Figure 19b, where secondary streamers start out of the primary streamers and their stem plasma channel outshines the background illumination. They have a filamentary structure (channel diameters larger than that of the primary streamers, roughly in the 5–25 μm range), and propagate much faster than the primary streamers, as it can be seen in the Figure 19a. In the third frame the secondary streamer initiation is visible and the last three frames show their fast growth: the propagation velocity was as high as 30-40 km·s^{-1}. Upper limit of the propagation velocity of secondary streamers is not known; it commonly ranges from a few kilometers per second to about 500 km·s^{-1} (depending on voltage used and on electrode geometry) [48]. Field induced dissociation and ionization of molecules in the bulk liquid are considered as mechanisms for secondary streamer propagation, because electric field around secondary streamer heads reaches 2 GV·m^{-1} [47]. The ion mobility in the liquid vapor in the streamer channel gives drift velocities of the order of 10^3 m·s^{-1} for heavy ions and 10^5 m·s^{-1} for protons, the main product of the water dissociation and ionization. The vaporization at the tip of a streamer head thus also takes place due to charged particle flow from the discharge plasma in the streamer channel (fast energy input into the water volume). This argument is based on the fact, that the discharge input energy is consistent with the energy required to vaporize the volume of water contained in the streamer channels [51]. Since the mechanism of the Townsend breakdown in water vapor is independent on the water conductivity, the streamer velocity also does not depend on the water conductivity. Electron densities in positive streamers were measured in [52] by fitting the single Voigt peak function to the observed H$_\alpha$ profiles. The estimated electron densities was of the order of $n_e \approx 10^{24}$ m^{-3} in water solution of NaH$_2$PO$_4$ (conductivity 10 mS·m^{-1}, gap 28 mm at 24 kV, measured 300 ns from the discharge onset), and rapidly rose with increasing conductivity. Electron number density in the tip of the secondary streamer was estimated in [47] as $n_e \approx 1.5 \cdot 10^{25}$ m^{-3} at about 100 ns after the streamer ignition (conductivity 0.2−80 mS·m^{-1}, gap 20 mm, voltage 17–25 kV). Plasma kinetic temperature in the streamer channel in pure water (conductivity 5 μS·m^{-1}) was found to range between 3000−4000 K [53]. The propagation length of the positive secondary streamer is very erratic with respect to the anode peak voltage, and decreases with increasing solution conductivity, especially for conductivities larger than 100 mS·m^{-1} [54] [55]. Growth process of the positive secondary streamer in
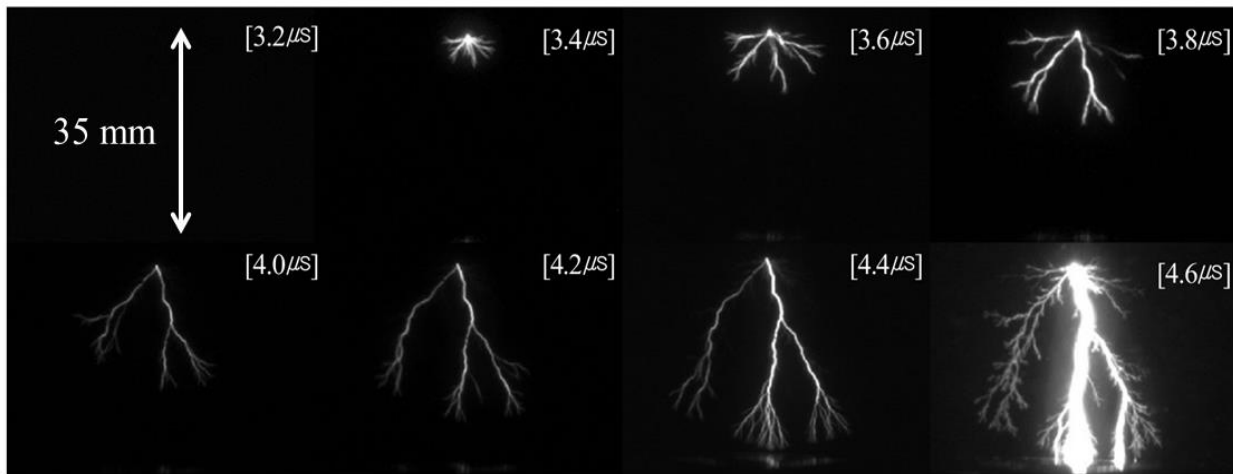
Figure 20 Growth process of the positive secondary streamer in water when the voltage of 37 kV was applied 3.2 μs after the first frame. The water conductivity was 100 μS·m^{-1} and the shutter time of used ICCD camera was set to 1 ns **[54]**. The primary discharge is indistinguishable.

water with the time step of 200 ns is shown in the Figure 20. The coronas were initiated at the tip of the needle anode 3.2 µs after the positive voltage pulse had been applied to the electrodes, and they began to propagate toward the plane cathode. When the streamer reached the opposite electrode (cathode) streamer to spark transition happened. Propagation of the secondary streamers is accompanied by generation of strong shockwaves with estimated peak pressure of about 3 GPa [47] (more in the next chapter).

3.2 Negative initiation electrode

**Elongation of bubbles in the anode direction**

Similarly as in the case of the positive initiating electrode, also this type of propagation is the slowest one (and even slower than in the case of the positive plasma channel). Bubbles, in which electrical breakdown occurred, elongate from the spot, where the gas plasma is connected to the bubble wall. The elongation is obvious in conductive water solutions and almost disappears in distilled water. Experiments with discharges in bubbles in water solution of NaCl (conductivity 30 mS·m^{-1}) made in [39] showed that in capillaries with the inner diameter of 0.38 mm and applied voltages up to 10 kV the bubbles preferentially shift to the cathode side of the capillary and even sometimes are ejected from the capillary into the liquid reservoir, when intense discharges occur. The shifting velocity is of the order of 25 mm·s^{-1}. The polarity change excluded geometrical effects that were suspected to cause this phenomenon. The finally accepted explanation is based on asymmetric plasma heating of bubble wall, which is more intense on the cathode side of the bubbles, and creates there stronger vapor flux. In support of this explanation it is possible to say, that it has been proved (see experimental part of the next chapter) that this phenomenon is more significant in solution with higher conductivity.

Plasma created between metal cathode and water anode has the typical spatial emission pattern of a diffuse glow discharge with unstable anode spot on the water surface [45]. The plasma structure has typical features of a glow discharge: a cathode fall, a negative glow, a Faraday dark space, a positive column and an anode glow region. Rotational temperature of N_2 near tap-water anode (51 mS·m^{-1}) was estimated to be $T_r = 1400\pm200$ K at the discharge current of 30.9 mA, and was nearly independent on the current changes at currents higher than 17 mA [45]. The only data on electron concentration and temperature in vicinity of water anode were obtained from experiments with both electrodes liquid. The average electron concentration in discharge between tap water electrodes was determined to be $5\cdot10^{17}$ m^{-3}, and the average electron temperature to be 4600 K at the discharge current 60 mA [56]. The authors also estimated electron-neutral collision frequency to be of the order of 10^{11} s^{-1}.

Negative streamers

Negative streamers readily emerge/grow from the discharges in bubbles, as it is shown in the experimental part. They do not exhibit the hemispherical shape as positive primary streamers do, but they are more bush-like. They have a smaller propagation velocity at moderate voltages (< 400 m·s^{-1}) [49], but their propagation may be even supersonic. If the electric field between electrodes is stronger than 30 MV·m^{-1}, then an increase in streamer velocity is directly proportional to this electric field. Contrary, positive secondary streamers accelerate in this manner twice faster than negative streamers; this is valid up to electric field about 60 MV·m^{-1}. Above this threshold, negative streamer propagation stagnates at a velocity of about 1000 km·s^{-1} [48]. Propagation velocity of negative streamers is independent on the water solution conductivity [54]. Negative streamers in water with higher conductivities are much thicker (the characteristic diameter of negative streamers in distilled water is as large as 50 µm) and decrease in their

length [49]. Luminosity of negative streamers is more intense in solutions with higher conductivities at the same applied voltage levels.

a)

b)
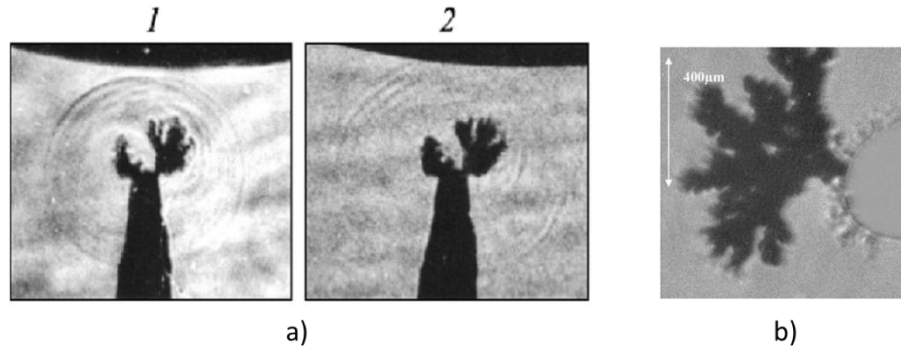
Figure 21 a) Schlieren photographs of an electric discharge from the cathode in distilled water; the distance between the electrodes was of 0.9 mm, electric field near the tip electrode was of 220 MV·m^{-1}, the frame exposition was 5 ns, and the time interval between frames was 90 ns. **b)** A detailed schlieren photograph of the negative streamer near the tip of the needle cathode [57].

Negative streamers are sometimes referred to as non-luminous, because they have much smaller luminosity than the positive secondary streamers. Therefore, for detection of their (negative streamers´) emitted light it is necessary to use ICCD (Intensified CCD) camera. Development of negative streamers is very diffused. Although plasma channel of a subsonic negative streamer may break, e.g. due to hydrodynamic instabilities that may form along the discharge channel, the streamer tip moves persistently across the gap between electrodes [58]. Schileren photographs of negative streamers generated on a tip electrode are depicted in the Figure 21. The average propagation velocity of the negative streamer in the Figure 21a is approximately 1 km·s^{-1}, and their propagation was accompanied by generation of shockwaves, which are visible as the dark circles. In the Figure 21b there is a photograph of a more enlarged negative streamer arising from the cathode tip [57], where the typical bush-like morphology can be seen. The Figure 22 illustrates the growth process of a negative streamer in water in a large gap. The last frame was taken with a longer interframe delay to record the final breakdown of the interelectrode gap. The number of streamers of the negative discharge is larger than that of the positive secondary discharge (in the Figure 20). Light emitted by the channels of the streamers is obviously less intense and streamers are terminated by bright tips.
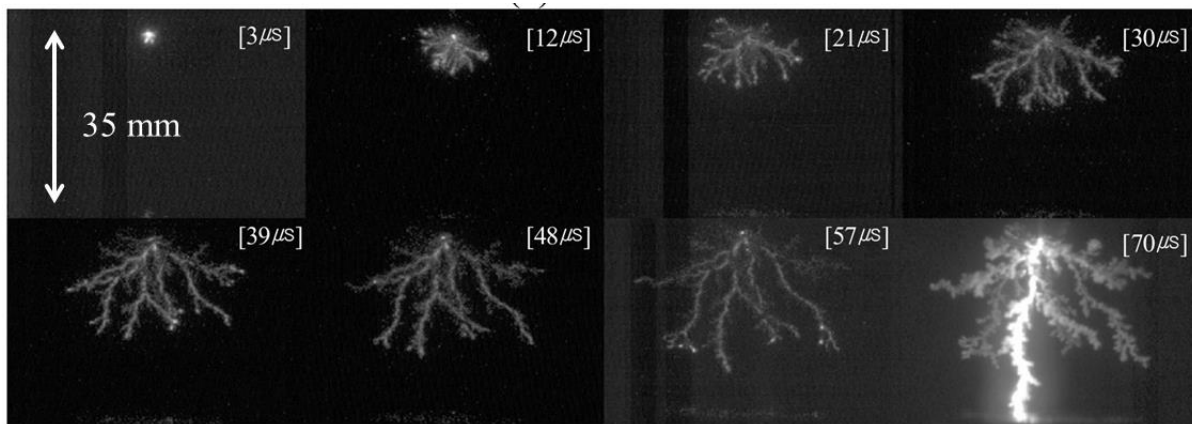
Figure 22 The growth process of negative streamers in water, 3 μs after the voltage of 85 kV was applied. The water conductivity was of 100 μS·m^{-1} and the shutter time of used ICCD camera was set to 2 μs **[54]**.

25

3.3 Experimental part 1

Propagation of plasma channels in water has not been fully explained yet, as it follows from the previous chapters. It has been said that ionization of molecules in bulk liquid by electric field of the order of GV·m^{-1} is responsible for high propagation speed of secondary streamers. Question is, what process on a plasma-liquid boundary causes development of tiny structures producing so strong electric field. Although all the mentioned mechanisms of discharge initiation in water (Chapter 2) require presence of strong electric field in liquid (10^8 V·m^{-1}; in the case of ionization mechanism it is even more - 10^9 V·m^{-1}), it does not mean that secondary streamers utilizing ionization of liquid water for their propagation must be initiated by a needle electrode producing comparable electric field around its tip. Even discharges initiated on electrodes in relatively large bubbles can transform to secondary streamers with time. Therefore, the main purpose of experiments described in this chapter was studying transitions of gas discharge in contact with surface of liquid electrode (distilled water, or a conductive water solution) to a streamer discharge in the liquid volume.

Experimental setup

The experiments were not conducted in gas phase within bubbles (where initial discharges often occur) for two reasons: firstly, the interior of bubbles cannot be clearly observed due to the light reflection and diffusion on the bubble boundary, and secondly, the streamer transition happens too quickly at voltages necessary for breakdown of bubbles at atmospheric pressure that it was beyond capabilities of the fast camera used. These issues are illustrated in the Figure 23, which also shows an influence of the liquid conductivity on the streamer formation.

Therefore, the bubble inner surface was imitated by meniscus of liquid water inside a glass capillary, because a meniscus, when small enough, has nearly spherical geometry. Besides that, the glass capillary
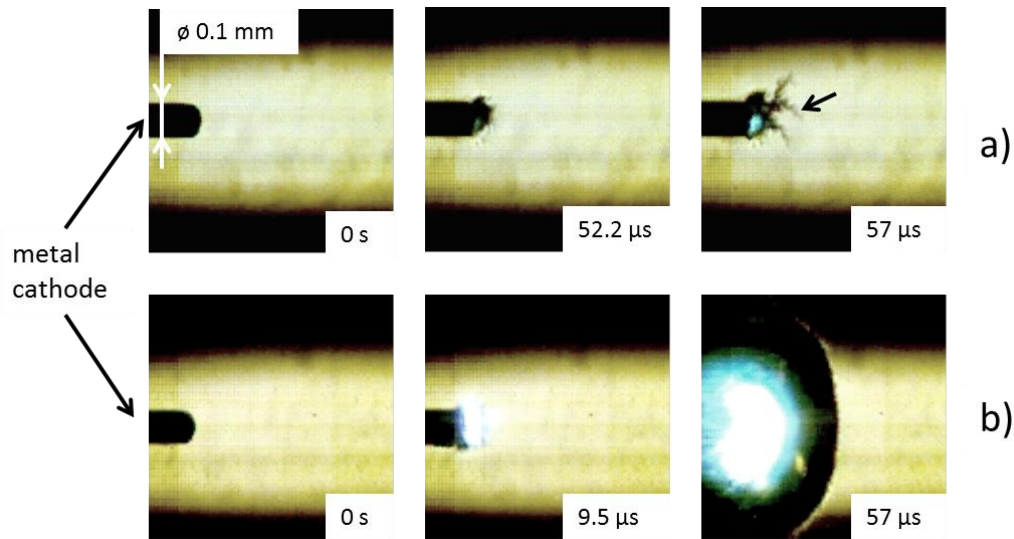
Figure 23 Two examples of the discharge development at the tip of a metal (copper) cathode, made under the same conditions (cathode-anode distance 15 mm, voltage 16 kV, high voltage capacitor 50 nF) but the liquid conductivity: **a)** 45 mS·m^{-1} (tap water used); joule heating resulted in the bubble formation on the cathode tip with consequent vapor breakdown (52.2 μs) - typical electrothermal liquid discharge initiation (chapter 2.2). Streamers (pointed by the black arrow) originated on the wrinkles of the bubble surface (57 μs). The transition bubble-streamer was indiscernible. **b)** 300 mS·m^{-1} (water + NaCl); bubble quickly formed on the cathode tip with vapor breakdown (9.5 μs). Then the bubble expanded without any streamer formation (57 μs).

limits the initial area of the liquid electrode surface; that is probably even more important property of this arrangement of the liquid electrode, since a discharge burning between water electrode with large free surface and metal-pin electrode above this surface remains dancing on the liquid surface [49]. Therefore, without any water-surface limitation, which in bubbles naturally exists, the discharge current is not concentrated to a small area, which is characteristic for bubbles. It is obvious, that any observation of shockwaves from corona discharges in glass capillaries is not possible with the fast camera used, because the camera's minimum opening is 1 µs. It is too long in comparison with the propagation speed of any shockwave, which is higher than the speed of sound in water ($\approx$1.51 km·s^{-1}); any trace of shockwaves would have been totally smudged. Next reason is that minimum interframe delay of the fast camera is 2 µs, which is too long for catching any shockwave on its way through the capillary. The whole experimental part described in this thesis was divided into two parts for this reason.

The experimental setup of the first experimental part is depicted in the Figure 24. The power supply consisted of a high voltage capacitor C, whose capacity was in 10 - 400 nF range, which was charged up to 50 kV by a high voltage DC power supply (Glassman WR125R2-220, not plotted). The discharge current was limited by a high voltage resistor 10 kΩ (a battery of Allen Bradley high voltage ceramic disc resistors) protecting the used glass capillary from damage just in the case of the liquid breakdown. Next, a pressurized spark gap was used as high voltage switch. Once the high voltage capacitor had been charged, pressure in the spark gap was manually decreased (trigger), which facilitated the spark gap self-breakdown. The electrode system itself consisted of the glass capillary, which was from the bottom side filled (by injection needle) with the conductive water solution, while its upper end remained opened. The opened end was connected by a pipe to a vacuum pump or to a nitrogen/argon cylinder. The upper high voltage electrode was placed closely above the liquid surface, the lower, grounded one was immersed in the liquid solution at the sealed end of the capillary. The voltage across the electrode gap was measured by a high voltage probe (North Star PVM-1), and the discharge current was calculated from the voltage on 1 Ω resistor. Although the immersed electrode was not directly grounded, the voltage on the current sensing resistor was negligible in comparison with the voltage on the high voltage (upper) electrode. Therefore, the high voltage measurement was practically uninfluenced by the voltage loss on the resistor. Both voltage signals were measured by an oscilloscope (Tektronix DPO 4034), which was triggered by the rising/falling edge of the signal from the high voltage probe. The oscilloscope then directly triggered the fast camera (Phantom v710). The fast camera enables recording in the infinite loop regime, which
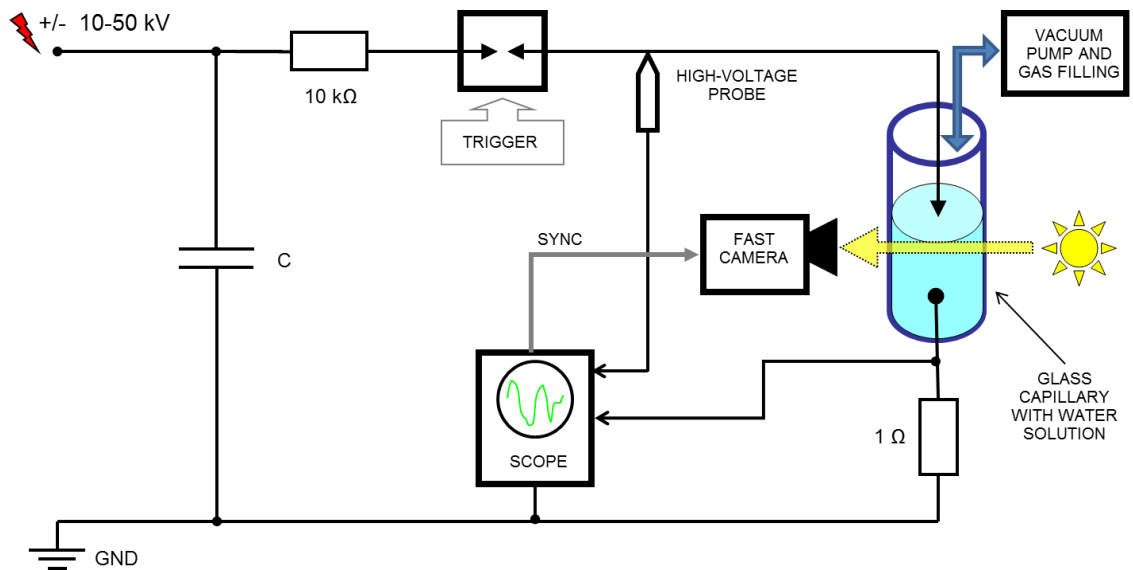

Figure 24 The experimental setup of the apparatus used for studying discharges in liquid water solution in a glass capillary.

means, that the output recording contains frames captured before the camera trigger as well as frames after that. The illumination of the capillary was provided by a white light bulb (15 W), which allowed distinguishing of the discharge colors, or by a green power LED (12 W), the higher light-power output of which allowed using of higher camera frame-rate (requiring shorter exposure time).

Experiments with negative high voltage electrode

The early experiments were only aimed at achieving and registering transition from the gas discharge to a streamer propagating from the meniscus surface into the liquid volume. They were conducted at four different conductivities of water solution: 300 mS·m^{-1}, 18 mS·m^{-1} (both solutions of NaCl), 45 mS·m^{-1} (tap water), and 170 µS·m^{-1} (distilled water).

The first experiment expectedly did not show any streamer in liquid, but it was useful for comparisons with the consequent experiments, where streamers appeared. The most important frames extracted from the captured video are depicted in the Figure 25. In the first frame taken 4.6 µs after the trigger a violet plasma channel connecting the metal cathode with the liquid surface can be seen. The channel did not touch the liquid surface in one or more discrete points; it rather crept along the surface (as expected). The second frame (46 µs after the trigger) shows deviated plasma channel with a different color, and a shadow (visible as a dark edge) of gas expanding out of the capillary at velocity of approximately 8.2 m·s^{-1}. Considering the change of plasma color, it was probably expanding water vapor produced by rising of vapor pressure (2.30) due to plasma heating of the liquid surface. This heating is confirmed by the third frame (1261 µs after the trigger), where brighter and darker boundaries of liquid volumes with different
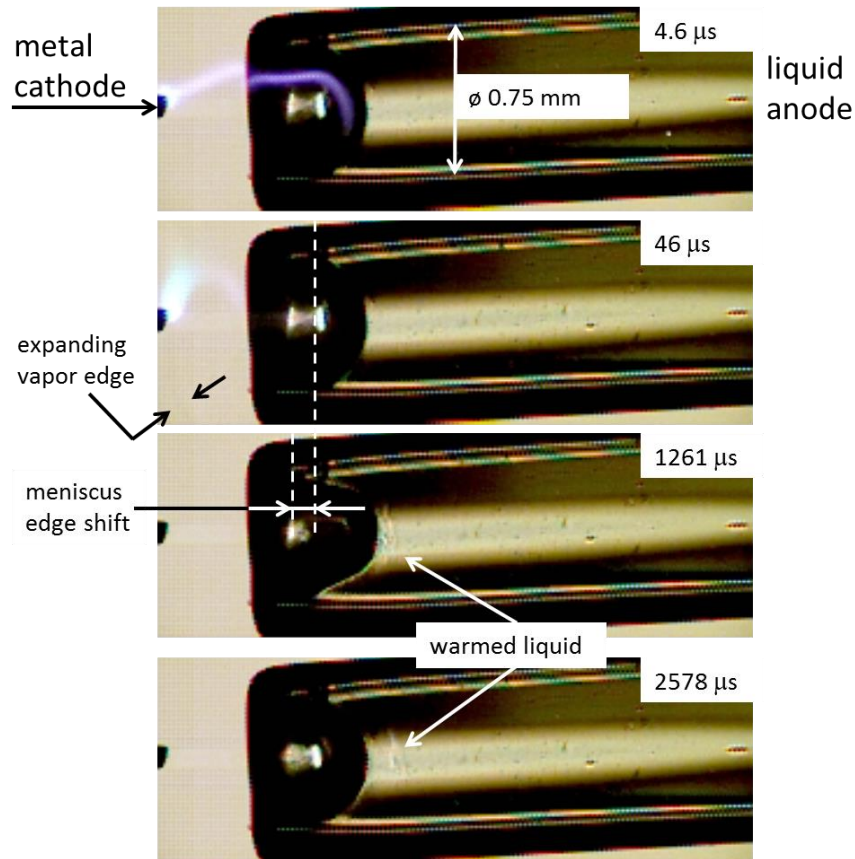

Figure 25 Photos of the discharge between the metal (copper) cathode and the liquid conductive anode within the glass capillary; conductivity of the water solution was of 300 mS·m^{-1}, heigth of the liquid column was 20 mm and the high voltage capacitor was charged to 11 kV. Exposer time was of 4.1 µs. The originally vertical photos are 90° rotated.

refraction indexes (due to different temperatures) near the liquid surface is visible. These changes in brightness appear at the meniscus bottom only, indicating, that there was maximum current density. This can be explained by the fact, that the creeping plasma channel (in the first frame) covered the liquid surface near the meniscus bottom, too. Then there must have been the strongest electric field on the meniscus bottom, and hence, the strongest current density. The third frame also shows a shift of the meniscus edge toward the capillary end along with an obvious shift of the meniscus bottom in the opposite direction. This fact points to a pressure pushing the liquid in the place of the meniscus bottom into the capillary resulting in the elevation of the surrounding liquid. This pressure can be reaction to the water evaporation near the meniscus bottom, as a consequence of the strongest plasma heating. The correlation with the current density is obvious: at the meniscus bottom, where the current density reaches its maximum, is also maximum flux of (hot) ions from the surface plasma into the liquid, and hence, the maximum heat flux (chapter 3.2). The liquid returns to its initial position after about 2.5 ms (fourth frame in the Figure 25), when the capacitor had been discharged. The liquid level and the meniscus appearance are undistinguishable from the initial state, which means, that only imperceptible amount of the liquid evaporated.

Next experiments were conducted in a thicker capillary with the inner diameter of 2 mm, where it was possible to better observe processes near the capillary inner wall. The liquid conductivity must have been decreased to achieve the surface-streamer discharge transition. It was successful in tap water with conductivity of 45 mS·m^{-1} or solutions of NaCl with the same or lower conductivity. The next two described experiments were performed under the same conditions with exception of the height of the liquid column. The common parameters were: charging voltage 20 kV, capacity of the high voltage capacitor 10 nF and water solution conductivity 18 mS·m^{-1}. While surface-streamer transitions were found to appear at column heights lower than 15 mm (electric field >1 MV·m^{-1}), they did not happen at heights greater than 20 mm. Therefore, the column lengths of 10 and 25 mm were chosen for the demonstration here. The Figure 26 shows what happens in the capillary after the spark gap breakdown. In the case of the high (25 mm) liquid column (Figure 26a) the mean initial discharge current is of 40 mA, as depicted in the plot at the bottom of the figure. This value corresponds to applied voltage, the liquid conductivity and the dimensions of the liquid column. The penetration of the plasma channel starts at the meniscus bottom point (second frame), and the hollowed cavity (bubble) proceeds in elongation always from its tip(s) at a maximum propagation speed of 5.5 m·s^{-1}. Similarly as in the first experiment, liquid surrounding the elongating cavity is pushed in opposite direction out of the capillary. The average diameter of the cavity is ~1 mm. When the cavity length reaches ~4 mm, hydrodynamic instabilities due to pressure of the liquid surface tension (2.24) develop. This causes throttling of the long hollowed cavity, which is shown in the third frame (2085 μs). Until lapse of time ~ 2.5 ms, the cavity keeps its continuity by a process of rebounding surrounding liquid at the throttled points. Then, obviously due to insufficient discharge current (capacitor discharged), the cavity finally brakes in many parts at the throttled points. The total breakdown did not happen. The gas from the destroyed cavity remains in the liquid in form of many bubbles, as shown in the fourth frame (2630 μs).

Although the voltage between the electrodes is falling, the current flowing through the capillary remains approximately constant or even is slightly increasing (bottom plot in the Figure 26a). The total load resistance decreases during 1.8 ms from 450 kΩ (the initial resistance) to 236 kΩ. Such high decrease could not be explained either by reducing of height of the liquid column as the cavity elongated, or by rising of the liquid temperature (joule heating). The height of the liquid column decreased during 1.8 ms to 84 % of the initial height. According to (2.26), temperature of the rest of the liquid column raised by 3.5 K over the same time. Using the approximation of 2 %·K^{-1}, the liquid conductivity increased to 107 % of the initial value. These two values mean that the initial load resistance should decrease from the initial value of 450 kΩ to 353 kΩ only. This discrepancy is probably caused by rising of ionic concentration in the liquid by electrolysis of the immersed copper electrode (dissolving of positive copper ions) and by an injection of ions from the plasma channel into the liquid. The spikes appearing after 600 μs in the current
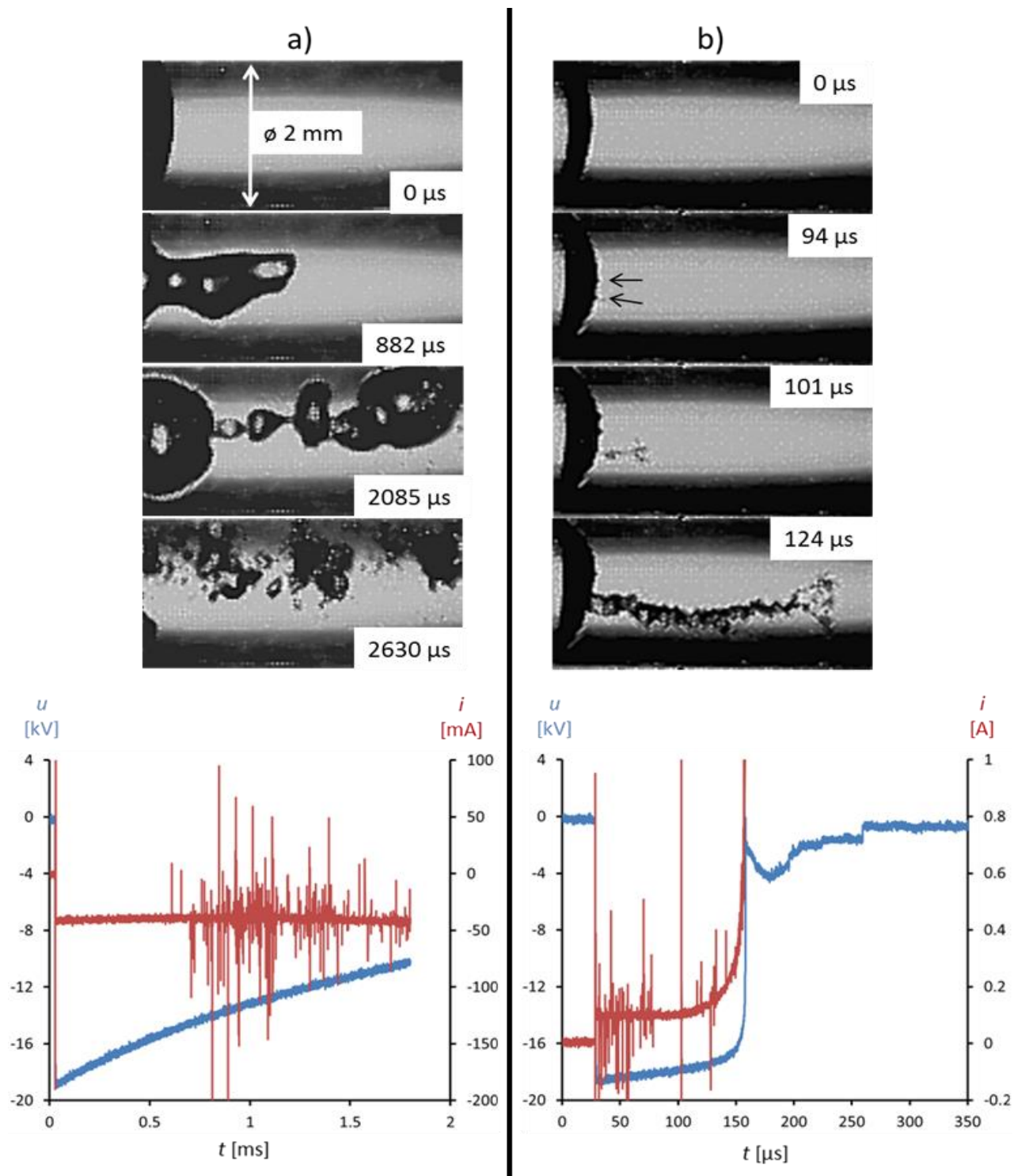
Figure 26 Plasma channel penetrating into the volume of conductive water solution by **a)** bubble elongation (liquid column height 25 mm), and **b)** as the negative streamer (liquid column height 10 mm). Other parameters are common: capillary diameter 2 mm, charging voltage 20 kV, capacity of the high voltage capacitor 10 nF and water solution conductivity 18 mS·m⁻¹.The metal (copper) electrodes are not visible; the cathode was placed just above the meniscus surface (on the left side, see Figure 25). The corresponding measured V-A waveforms are attached to each video sequence at the bottom. The originally vertical photos are 90° rotated. Water surface on the left.

waveform were probably associated with fine breakdowns taking place in tiny gas crevices or microbubbles in the liquid [48].

Figure 26b demonstrates transition to negative streamer realized in the short (10 mm) liquid column. The mean initial discharge current was proportionally larger: 100 mA. Although the liquid surface at the meniscus bottom started to shift slightly in the inward direction, another fundamental phenomenon definitely changed the next development. Tiny dips with diameter of about 50 μm early appears in the liquid surface. These dips are pointed by black arrows in the second frame (at 94 μs) of the Figure 26b. Very fine negative streamer then grows from one of the dips at the initial speed of 93 m·s⁻¹. It reaches anode in 157 μs and causes capillary breakdown accompanied by a significant increase of the current (bottom part of the Figure 26b).The initial diameter of the streamer channel cannot be exactly determined, because its projection on the camera image sensor is smaller than the side of one pixel. Therefore, it can be concluded that the initial streamer diameter is smaller than 31 μm.

The presence of the spikes in the current waveform immediately after the spark gap breakdown gives evidence of a rapid creation of gas crevices in the liquid surface, in which immediately an electrical breakdown occurs. These crevices may work as an inception of the surface dips, which, however, do not appear in solutions with higher conductivity. The growing mechanism of the dips seems to be similar to the mechanism of the cavity elongation, but acting in a smaller scale. It seems that plasma conductivity (above water surface) to water conductivity ratio may be the key factor, which decides, if water-surface is smoothened and dug in large area - that results in continuously elongated cavity, or if water surface is dug locally in places of inception dips – that results in formation of narrow tunnels of negative streamers. Let's assume that the vapor flux from the liquid surface is approximately proportional to the normal current density, and that the plasma conductivity just above the liquid surface is nearly constant over a wide range of current densities. Let's assume that the inception dip has the conical form with the
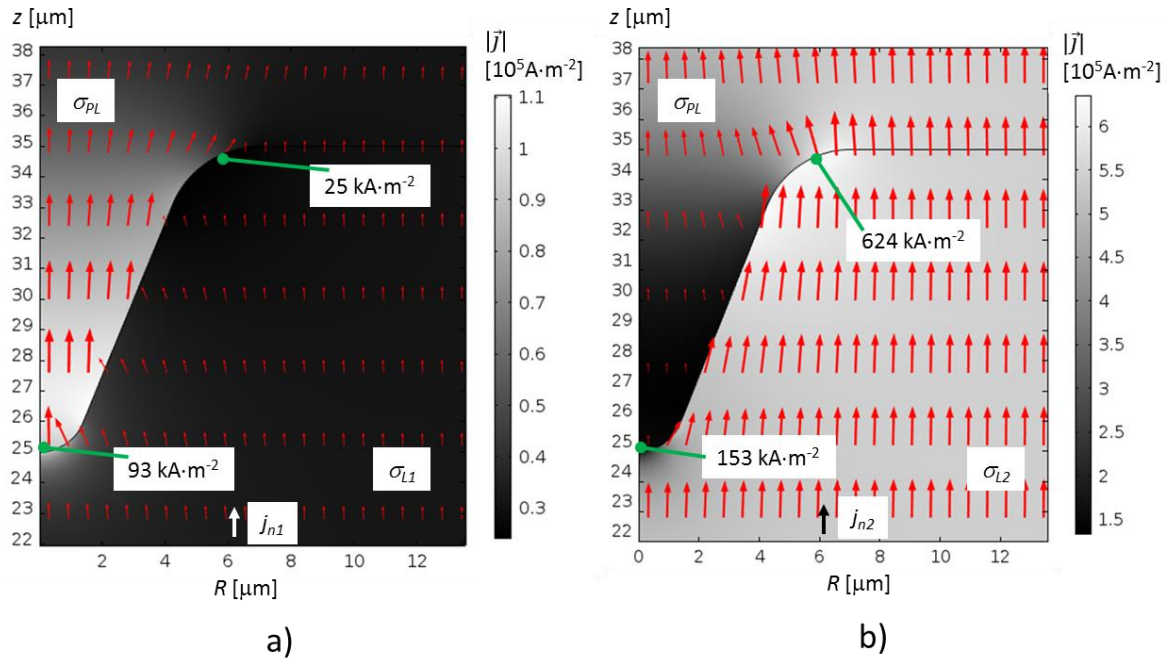
Figure 27 Stationary simulation of current density distribution in the place of a small perturbation of plasma-liquid boundary. Liquid conductivities were **a)** $\sigma_{L1} = 18$ mS·m⁻¹, **b)** $\sigma_{L2} = 300$ mS·m⁻¹ and the plasma conductivity was in both cases $\sigma_{PL} = 74.5$ mS·m⁻¹; boundary normal current densities were **a)** $j_{n1} = 31.8$ kA·m⁻² and **b)** $j_{n2} = 541$ kA·m⁻². The simulation was performed using Comsol Multiphysics software with liquid at the bottom and plasma at the top. The geometry was modeled in cylindrical coordinates (z - axis of symmetry, R – radial distance).

31

basement radius of 5 μm, and with the vertex height of 10 μm (Figure 27 – such a structure may represent a remnant of a deflated microbubble). Then it is possible to simulate situations/behavior at two different liquid conductivities - the same as in the described experiments: σ_{L1} = 18 mS·m⁻¹ and σ_{L2} = 300 mS·m⁻¹. The plasma conductivity was chosen as the geometric mean of the two liquid conductivities: σ_{PL} = $\sqrt{\sigma_{L1}\sigma_{L2}}$, which is σ_{PL} = 74.5 mS·m⁻¹. This choice ensured the same ratio of conductivities used in each simulation: $\sigma_{PL}/\sigma_{L1} = \sigma_{L2}/\sigma_{PL}$. The simulations used boundary normal current densities j_{n1} and j_{n2} instead of a voltage sources. The current density j_{n1} = 31.8 kA·m⁻² was chosen in accord with the current of 0.1 A measured in previous experiment (Figure 26b), and the current density j_{n2} = 541 kA·m⁻² corresponded to the ratio of the liquid conductivities σ_{L2}/σ_{L1} (neglected resistance of the plasma channel). The calculated current density distribution in the liquid with conductivity lower than the plasma conductivity ($\sigma_{L1} < \sigma_{PL}$) is shown in the Figure 27a. The highest current density is expectedly on the cone vertex (93 kA·m⁻²); the current density everywhere around the cone is nearly four times lower. Therefore, under these conditions the liquid evaporation is most intense right in the vertex and its close vicinity. The inception dip is deepened and sharpened, as can be seen in the Figure 26b. The opposite situation is shown in the Figure 27b, when the liquid conductivity is higher than the plasma conductivity ($\sigma_{L2} > \sigma_{PL}$). Although the current density on the cone vertex is higher than that in the previous case, the current density on the edge of the cone basement (edge of the dip) is four times higher than the current density on the vertex. This results in more intense evaporation of liquid from the surrounding of the inception dip than from its vertex, and hence, in smoothing of the liquid surface instead of the dip deepening.

Conductivity of weakly ionized plasma, where non-coulomb collisions dominate, and where electric current is formed mainly by electrons, is given by [1]

$$\sigma_{PL} = \frac{e^2 n_e}{m_e \nu_{en}} \quad [\text{S·m}^{-1}], \quad (3.33)$$

where e [C] is the elementary charge, n_e [m⁻³] is the plasma electron concentration, m_e [kg] is the electron mass and ν_{en} [s⁻¹] is the electron-neutral collision frequency. Using parameters cited in the Chapter 3.2 ($n_e \approx 5\cdot10^{17}$ m⁻³, $\nu_{en} \approx 10^{11}$–10^{12} s⁻¹) the equation (3.33) gives $\sigma_{PL} \approx 14$–140 mS·m⁻¹, which roughly coincides with the interval of liquid conductivities (σ_{L1}, σ_{L2}) used in the experiments and simulation described above.

The negative streamers apparently do not appear until a sharp tip on a dip is developed, i.e. until strong enough local electric field is created. Negative streamers keep the fine structure at their tips during their propagation after the initiation, as is shown in the fourth frame (124 μs) in the Figure 26b. The easiest explanation of the principle of negative streamers propagation, next to the ionization mechanism described in the Chapter 2, is that it is the same mechanism as that of propagation of the cavities or the dips. The distribution of the current density on the plasma-liquid boundary is unstable due to liquid evaporation. Any initial surface disturbances boost the current density in surface valleys causing simultaneously a detriment of the surrounding current density. Consequent stronger liquid evaporation from the valleys causes their deepening, and hence, next enhancement of the current density distribution inhomogeneity.

The next experiments were conducted with distilled water and at low pressure. The capillary had been evacuated down to the water saturation pressure at room temperature (≈ 3 kPa), and then after water stopped boiling, the gas discharge was initiated. The surface-streamer transition took place obviously easier than at atmospheric pressure; it was possible to achieve the transition even with the liquid column height 25 mm. In addition, nearly no ripples on the liquid surface were observed, and dimensions of the dips were in average smaller in the moments of the streamers initiation. The other experiments with negative electrode in argon at atmospheric pressure above the liquid anode did not show any differences in the surface-streamer transitions, when compared with the experiments conducted in air at atmospheric pressure.

Experiments with positive high voltage electrode

The first experiment with the liquid cathode was conducted with the same experimental setup as the first experiment with the liquid anode (Figure 25). Although this experiment showed no surface-streamer transition in liquid, it was useful for comparison with the experiment with liquid anode. The most important frames extracted from the captured video are depicted in the Figure 28. In the first frame taken 10 μs after the trigger, a violet creeping plasma channel can be seen, similarly as in the configuration with the liquid anode (Figure 25). After 30 μs, color of the plasma channel changed from violet to yellow indicating sodium evaporation from the liquid (see also [40]). Then, the liquid evaporation caused sinking of the liquid surface and creation of holes in it (110 μs and 215 μs). The liquid evaporation and tunneling was incomparable with that described in the case of liquid anode at the same current; the vapor flux was so intense that it tore off surrounding liquid out of the capillary (400 μs). Nevertheless, no bubbles accompanying boiling of the liquid near the meniscus bottom were observed, which means, that only the liquid surface was heated by plasma. A significant shift of the liquid around the created cavity toward the capillary end points to substantial pressure exerted on the liquid surface on the meniscus bottom as a reaction to the liquid evaporation.

The obvious difference of the surface plasma heating between the liquid anode and the liquid cathode has not yet been explained. The presence of the cathode dark space adjacent to the liquid cathode surface, which does not exist in the case of liquid anode, can play some role. Nitrogen N_2^+ ion-neutral mean free path at neutral gas temperature of 300 K was used for estimation of the mean energy of ions impacting the liquid surface. Choice of this temperature can be satisfactory due to cooling of adjacent plasma by flux of water vapor. The mean free path is of the order of $\lambda_{in} \sim 50$ nm [59]. Accounting the potential drop across this area ≈ 500 V and its thickness ≈ 0.1 mm (see chapter 3.1), the typical electric field above a liquid cathode is $E_c \approx 5$ MV·m^{-1}. Since the potential drop along the mean free paths is $E_c\lambda_{in} = 0.25$ V, the mean
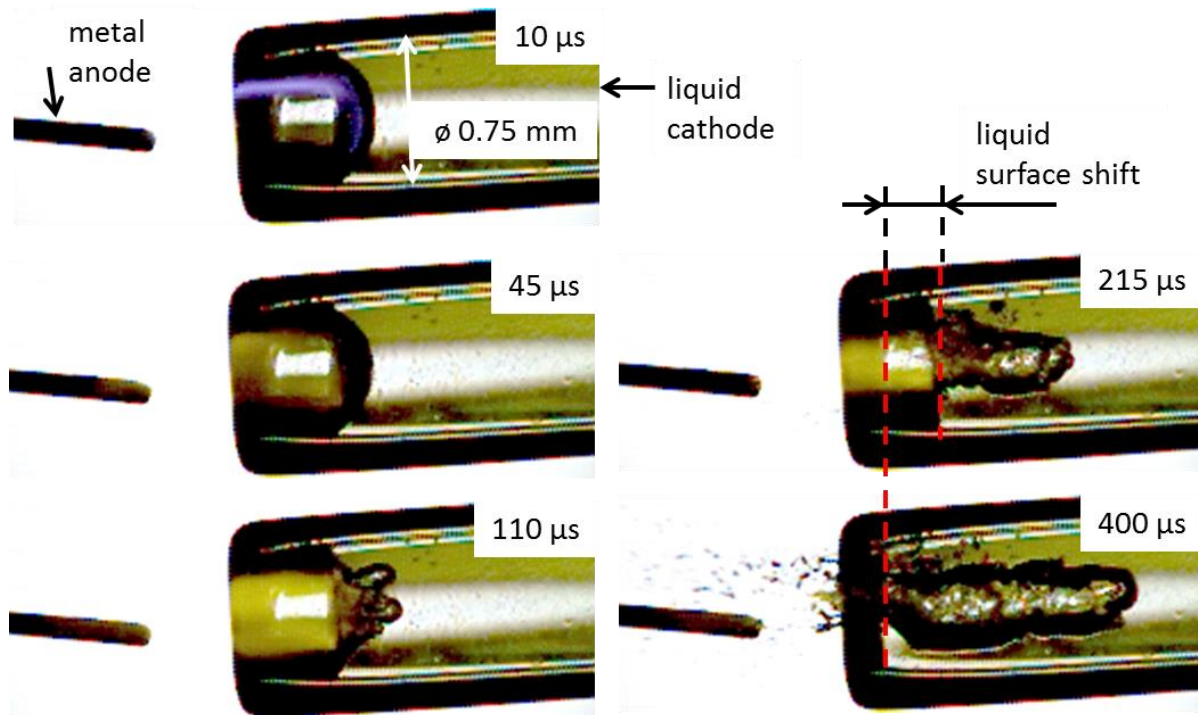
Figure 28 The discharge between the metal (copper) anode and the liquid conductive cathode within the glass capillary; conductivity of the water solution was of 300 mS·m^{-1}, height of the liquid column was of 20 mm and the high voltage capacitor was charged to 11 kV. Exposer time was 4.5 μs. The originally vertical photos are 90° rotated.

energy of the ions is of 0.25 eV. Nevertheless, the plasma ion concentration, which is of the same order as the electron concentration (due to quasi-neutrality), is by eight orders of magnitude smaller than the number density of water molecules. Hot ions with so small concentration can warm the water surface only negligibly.

This experiment showed that the intensity of evaporation from the liquid surface had no influence on the surface-streamer transition. Thus, the process shown in the Figure 28 represents just propagation of the plasma channel by the described bubble elongation mechanism; if the liquid column would have been short enough, the total breakdown would happen.

Next three described experiments with liquid cathode were conducted under conditions, when negative streamers easily developed; i.e. in degassed tap/distilled water (conductivity <50 mS·m^{-1}) with the liquid column height less than 15 mm. In the first case, the high voltage capacitor with capacity of 500 nF was used to keep the high voltage until breakdown. The capacitor was charged to 20 kV, and the column of distilled water (170 μS·m^{-1}) was 10 mm high (Figure 29a). This experiment showed also the bubble elongation toward the cathode, but it was accompanied by incessant creation of spikes similar to the dips, which worked often as streamer predecessors in the case of the liquid anode. These spikes did not emerge from calm liquid surface as the dips did; they developed from more extensive surface deformations only.

This is why the spikes and the dips are here consistently distinguished. Importance of this experiment lies in confirmation, that in the case of liquid cathode no spike-streamer transition occurs, if any spike develops. The spikes appear in places of the next cavity elongation. Similarly to dips in the case of the liquid anode, the spikes develop only in the liquid cathode with low conductivity (compare Figure 28 and Figure 29).

Therefore, the consequent experiment was performed with small column height (2.5 mm) to enhance the electric field at the tips of the spikes. Results are shown in the Figure 29b, where the immersed metallic cathode was added. Up to time of 177 μs after the spark gap trigger, the picture is the same as in the previous experiment (Figure 29a). The only difference is that the liquid deformation and the spike develops significantly faster (compare the time labels). Then, during following about 3 μs, the total electrical breakdown happens (180 μs). It indicates development of a positive streamer (primary or secondary) with minimum propagation speed of 667 m·s^{-1}. Nevertheless, also another scenario is possible: creation of gas bubbles on the metallic cathode surface and their breakdown (bubble discharge initiation) with consequent bubble-negative streamer transition. The electrothermal discharge initiation is not eligible, because according to equation (2.26), the liquid temperature rises only by 0.5 K in the lapse of time of 180 μs. Anyway it means that in this experimental setup (cylindrical capillary, distilled water, Phantom v710 fast camera) it was impossible to register the surface-positive streamer transition, because the camera was not fast enough to catch any streamer before breakdown.

The last experiment with liquid cathode in the cylindrical capillary was performed using tap water with conductivity of 43 mS·m^{-1}, the high voltage capacitor with capacity of 10 nF was charged to 45 kV and the liquid column was 15 mm high (Figure 29c). Since the camera was focused on the middle part between the meniscus and the immersed metallic cathode, the initial meniscus cannot be seen. The plasma channel propagated from the meniscus toward the metallic cathode at the average speed of 28 m·s^{-1} by the bubble mechanism. Although, the main pattern of the cavity was similar to that in the Figure 29a (thickness of the cavity, creation of spikes), the liquid surface inside the cavity was significantly rippled. There can be seen many of tiny protrusions with dimensions of the order of 10 μm on the surface of the developed cavity. These tiny protrusions probably do not represent the anode potential extensions. Diameter of protrusions taken from the second frame (174 μs) was approximately 50 μm, and their distance from the immersed cathode at that time was 8 mm. According to the V-A waveforms plotted in the bottom of Figure 29, the anode voltage was of about 35 kV at the time of 174 μs. Assuming that this potential was on the protrusion surfaces, the surface electric field estimated by the equation (2.11), where $a = 25$ μm and $b = 8$ mm, should be 400 MV·m^{-1}. According to chapter 3, this value should be sufficient to trigger primary streamers, which, however, were not observed in this case.
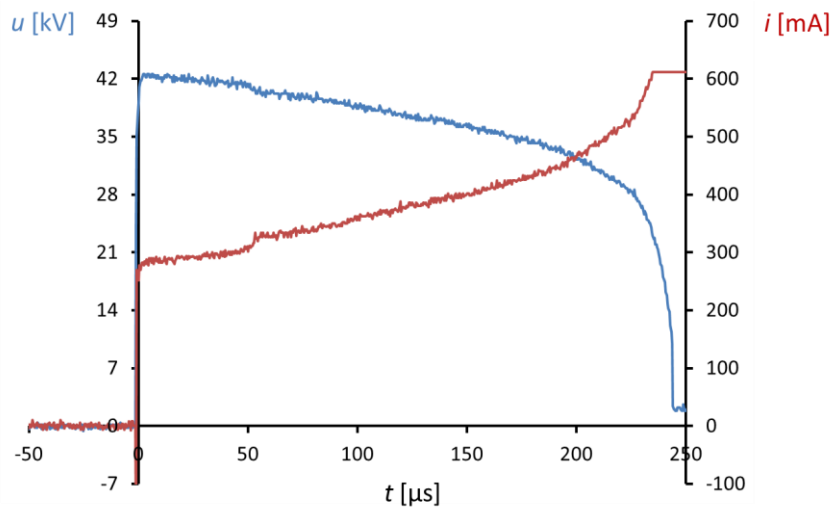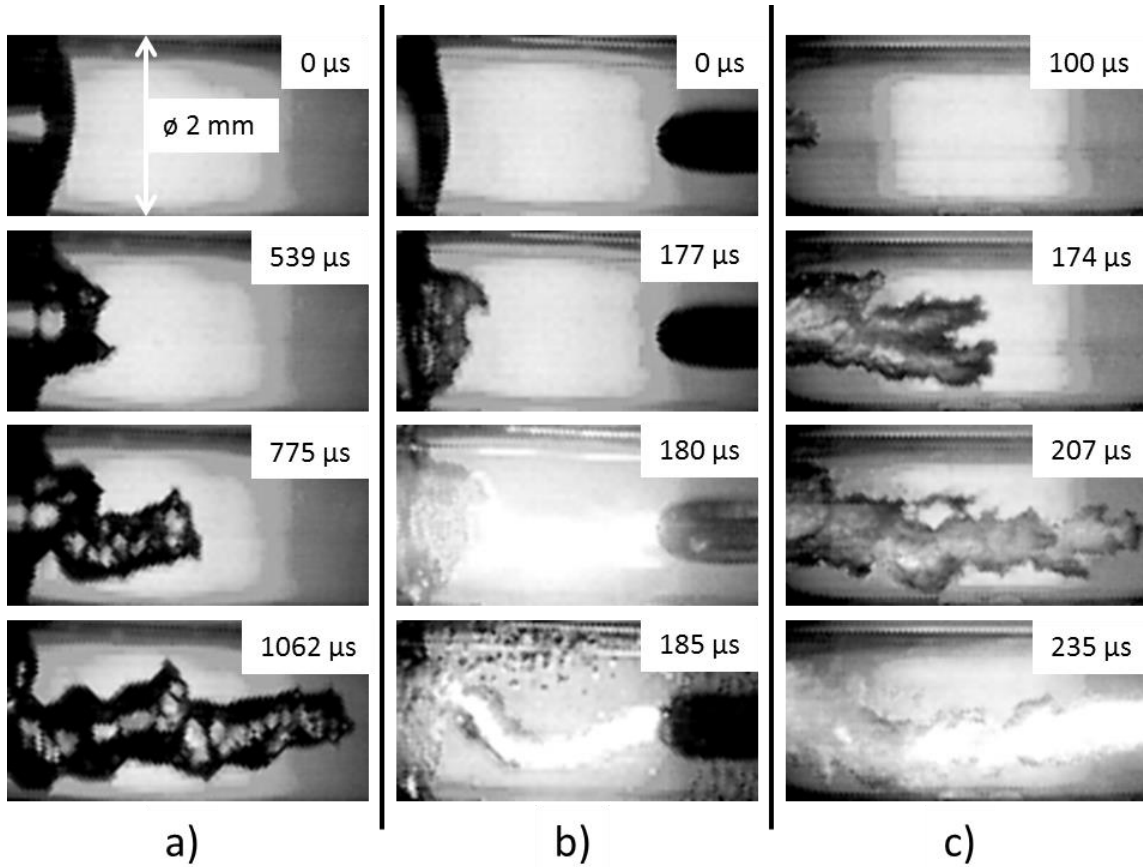
Figure 29 The discharge between the metal (copper) anode and the liquid conductive cathode within the glass capillary. **a)** the liquid column height 10 mm, water conductivity 170 μS·m^{-1}, charging voltage 20 kV, capacity of the high voltage capacitor 500 nF; **b)** metal cathode visible on the right side, the liquid column height 2.5 mm, water conductivity 170 μS·m^{-1}, charging voltage 20kV, capacity of the high voltage capacitor 500 nF; **c)** the liquid surface out of view, the liquid column height 15 mm, tap water conductivity 40 mS·m^{-1}, charging voltage 45 kV, capacity of the high voltage capacitor 10 nF. Exposure time was 0.87 μs in each case.

The measured V-A waveforms belong to the sequence c). The originally vertical photos are 90° rotated. Water surface on the left.

As the cavity tip approaches the metal cathode, current in the plasma channel increases, as is shown in the graph in the bottom of Figure 29. The final flat part in the current waveform was caused by an overflow of the oscilloscope A/D converter. The intensity of light emitted by the plasma channel was comparable with the background illumination just before the capillary breakdown (207 µs). The current waveform does not contain any spikes known from the waveforms in the Figure 26. This indicates absence of gas crevices created in the liquid surface, the subsequent breakdown of which is probably source of the current spikes in the experiments with liquid anode.

The fact that in case of high electric field (Figure 29b) we were not able to register the streamer development made us to modify the experiment creating high field (~8 MV m^{-1}, similar to value in the Figure 29b, where column height is 2.5 mm and voltage is 20 kV) in the meniscus region, where surface-streamers originate, and low field (~1 MV m^{-1}) in the region, where streamers propagate. Since streamer propagation speed depends on the electric field at its head, the streamer retards in low field region and can be captured by Phantom v710 fast camera. Such inhomogeneous electric field is created in capillary narrowing at its mouth (see Figure 30), where meniscus of conducting liquid is located, and where conditions for streamer-birth have to be fulfilled. Transition from a bubble to the positive streamer and its propagation in the broadened part of glass capillary are depicted in the top of the Figure 31. The capillary was filled with distilled water (170 µS·m^{-1}). It was expected, that it could take relatively long time (milliseconds) than any positive streamer developed. Therefore, the high voltage capacitor with capacity of 400 nF was used in this experiment to set up the circuit time constant large enough. The capacitor was charged to 35 kV. The initiation was preceded by deformation of the liquid surface accompanied by creation of tiny lobes. These lobes consequently separated from the surface and created bubbles, which remained connected with the surface by thin plasma channels. These bubbles are visible in the second (52 µs) and the third (159 µs) frame, where it is marked by the red arrow. Fine structures similar to primary streamers (the fan shape shown in the Figure 19) appear and disappear on the bubbles surfaces. With respect to the limited maximum resolution of the fast camera at high frame rates, it was impossible to recognize individual streamers in these structures. The positive streamer suddenly appeared at time of 162
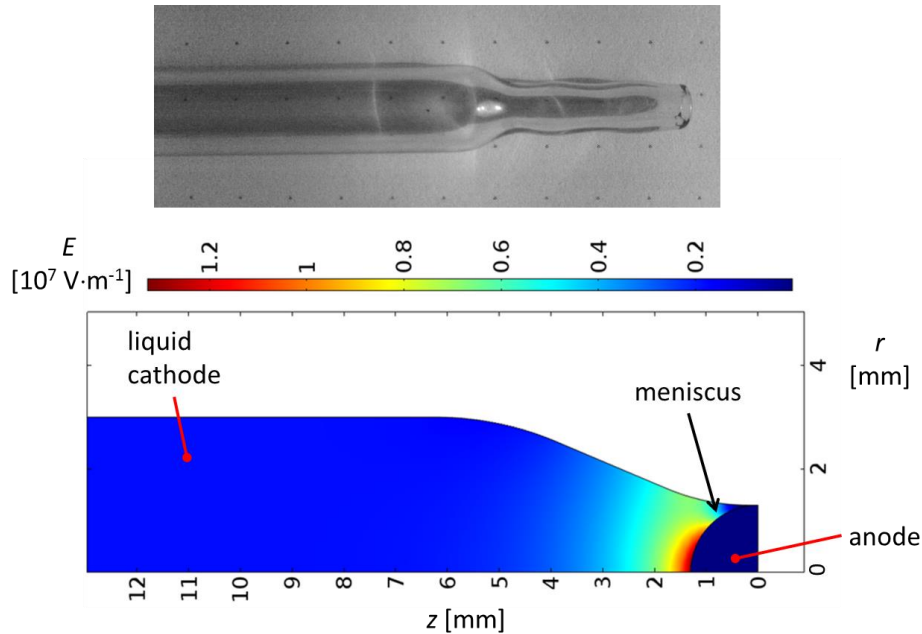
Figure 30 Photo of the glass narrowing capillary (top); the large dimension of depicted area is 5 mm. Distribution of electric field in the narrowing capillary filled with conductive liquid (170 µS·m^{-1}) at the anode-cathode voltage of 50 kV (bottom). The meniscus surface has the anode potential. The total length of the capillary is 20 mm; only a part is depicted. The simulation was performed using Comsol Multiphysics software.
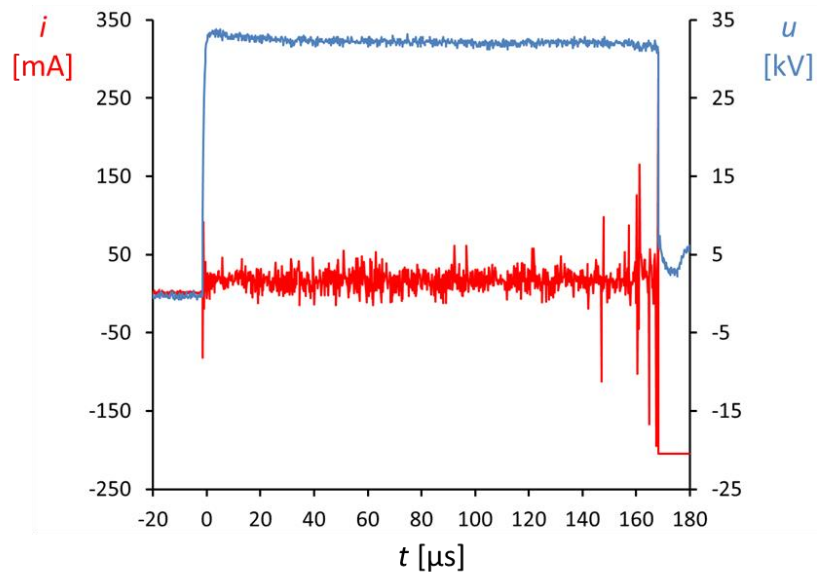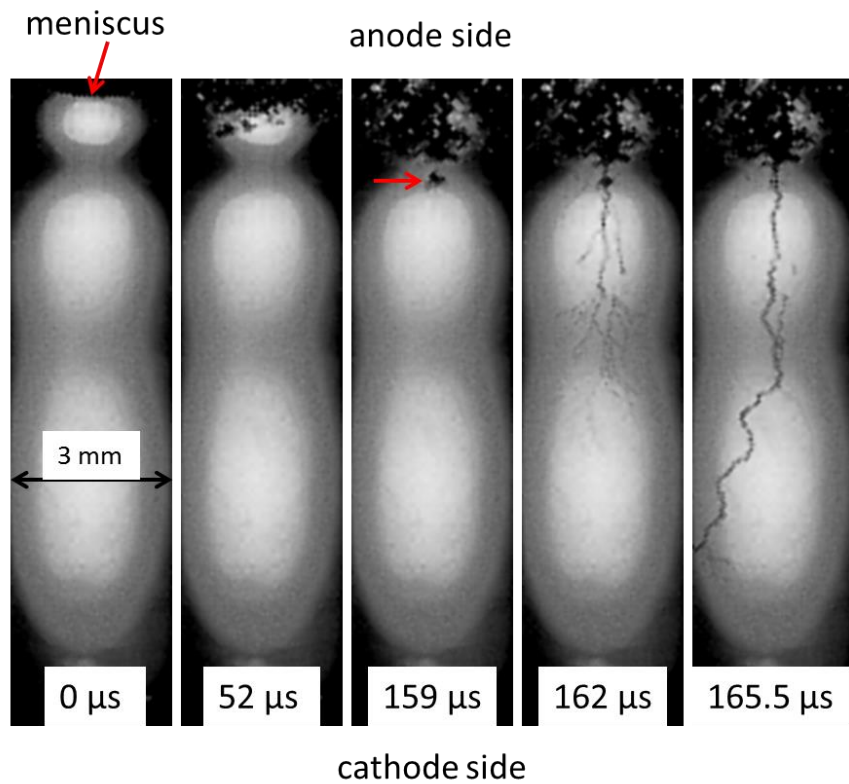
Figure 31 Transition from a bubble to the positive streamer and its propagation in the broadened part of glass capillary (top). The capillary was filled with distilled water (170 μS·m⁻¹), the high voltage capacitor (400 nF) was charged to 35 kV and the total height of the liquid column was of 15 mm. The capillary background illumination was not uniform due to the capillary curvature. Measured V-A waveforms are attached (bottom).
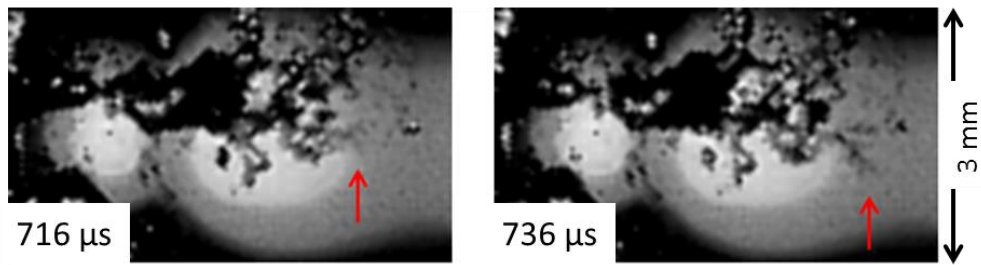
Figure 32 Transition from bubble to a slow positive streamer in the wide part of the narrowing glass capillary with narrowed mouth. The capillary was filled with distilled water (170 μS·m⁻¹), the high voltage capacitor (400 nF) was charged to 45 kV and the total height of the liquid column was of 15 mm. The originally vertical photos are 90° rotated. Water surface on the left.

μs after the trigger. Its appearance corresponds to the secondary streamers in the Figure 20. Due to low camera resolution (128×64 pixels) it cannot be concluded whether the secondary streamer was preceded by formation of the primary streamers. Although it emerged from the surface of the marked bubble in this experiment, another experiment showed positive streamer emergence from nearly calm surface at time of 8 μs after the trigger. The secondary streamer was split into many branches, but only one reached the immersed cathode finally. Minimum propagation speed calculated from the streamer shift between the third and fourth frame is 1.7 km·s⁻¹. If the ionization processes in liquid phase (chapter. 2.2) take place on the streamer head, then the streamer channel would be highly conductive. The propagation mechanism is then similar to the streamer mechanism mentioned in the chapter 2.1.

The current waveform at the bottom of the Figure 31 shows the significant current spikes just before the bubble-streamer transition. The current spikes thus work as a precursor of streamers. This indicates that the microcavities, the breakdowns of which are source of the current spikes, are created in the liquid cathode at much stronger electric fields than in the liquid anode. This also indicates that the microcavities are obviously essential for any streamer initiation. If the theory of secondary streamer propagation by ionization processes in liquid water (Chapters 2.2, 3.1) is valid, then the dimensions and the resistivities of microcavities, in which electrical breakdown occurred, must be as small as the electric field intensity on their surface is of the order of 1 GV·m⁻¹.

Besides the secondary streamers, tree-like structures similar to the negative streamers described in the previous part were rarely observed. Propagation speed of these structures was about 60 m·s⁻¹. Such a slow positive streamer is marked by the red arrow in the Figure 32. A spike developed on the elongating cavity fluently transformed into a slow positive streamer, just like dips in liquid anode. Although the charging voltage in this experiment was even higher than before - 45 kV, no secondary streamers appeared. The slow positive streamer was growing for about 15 μs, then it stopped, and decayed in bubbles. This means that slow positive streamers are relatively low-conductive in comparison with the positive secondary streamers; therefore, it does not effectively extend the anode potential to the streamers ends.

Conclusions of the experimental part 1

Experiments with liquid anode and cathode in glass capillaries have been done. The experiments were aimed at penetration of the plasma from the liquid surface (meniscus) into the liquid volume.
Experiments with liquid anodes showed, that liquid surface in the place of the largest current density (at the plasma-liquid interface) recedes. This receding is caused by liquid evaporation resulting in reaction pressure. Thus, long cavities with plasma inside can be formed or even can cause the total electrical breakdown. Propagation speed of the elongating cavity is of the order of 1 m·s⁻¹. The liquid surface of the

meniscus or cavity stays smooth when the liquid conductivity is larger than the conductivity of adjacent plasma. The plasma conductivity was estimated to lie between of $14-140$ mS·m^{-1}.

In the opposite case (if the liquid conductivity is smaller than the conductivity of adjacent plasma), small dips can be created on the liquid surface. These dips subsequently elongate, and often fluently transform into negative streamers, when electric field larger than 1 MV·m^{-1} appears near the liquid surface. Negative streamers propagate toward the immersed metal anode at the speed of the order of 100 m·s^{-1}. Creation of negative streamers is preceded by spikes in the discharge current waveform, caused by electrical breakdowns of microcavities.

Experiments with liquid cathodes showed significantly more intense liquid evaporation than the experiments with liquid anodes – under otherwise the same conditions. Therefore, propagation speed of gas cavities is also significantly higher. Although development of spikes on the liquid surface is also determined by the ratio of plasma-liquid conductivities, it is followed by transition to secondary positive streamers only when larger electric field than 10 MV·m^{-1} appears near the liquid surface. Also creation of positive secondary streamers is preceded by spikes in the discharge current waveform.

Besides the positive secondary streamers, slow positive streamers of low conductivity were rarely observed to grow from the liquid surface spikes. Propagation speed of these structures is of the order of 10 m·s^{-1}.

4. Shockwaves in water generated by corona-like discharges

Formation and propagation of discharges in water solutions is accompanied by generation of shockwaves, the nature of which depends on mechanism of the discharge initiation and propagation. The main attention was aimed at discharges in highly conductive NaCl solutions, because there is a lack of information on this topic in literature, and because the current corona-based generator of shockwaves uses highly conductive water solution.

4.1 Shockwaves in water

This chapter contains theoretical description of properties of shockwaves in water at presence of electric field. Final relations (4.28) - (4.30) link together pressure, liquid velocity and electric field at a shock front; this is important for later interpretation of some experimental results.

The Rankine-Hugoniot jump conditions and shock formation

The Rankine-Hugoniot jump conditions of a shockwave propagating in conductive liquid under electric field generally deal with discontinuity of pressure, liquid velocity, and with discontinuity of electric and magnetic field. When the liquid conductivity is large enough and when the shock wave thickness is small enough, then the lines of magnetic flux are considered to be frozen in the liquid. In such a case, the Rankine-Hugoniot jump conditions for ideal magneto-hydrodynamics are used for the description of relations on a shockwave discontinuity. Nevertheless, in the case of experiments it is not necessary to describe them in this chapter. There are the following reasons. First, magnetic fields generated in these experiments are relatively weak; the contribution of magnetic pressure to the total liquid pressure can be neglected. Second, at the used liquid conductivities the diffusion of magnetic field is much faster than the rate of the liquid compression by the shockwave. It is caused by a finite thickness of the shock front (the d_s in the Figure 33), which is always larger than the mean free path of liquid molecules. The molecule mean free path is approximately given by [60]

$$\lambda_m = \frac{\mu_d}{\rho_0 c_0} \qquad \text{[m]},\qquad\qquad (4.1)$$

where μ_d [Pa·s] is the liquid dynamic viscosity, ρ_0 [kg·m^{-3}] is the liquid density and c_0 [m·s^{-1}] is the speed of sound in the liquid. In water $\lambda_m \approx 0.7$ nm; hence, the shockwave thickness in the Figure 33 is
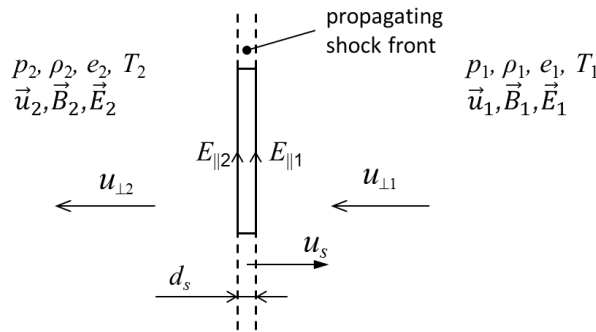
Figure 33 Change of quantities on a shock front; the shockwave can be considered either as a propagating shock front at the speed u_s (observer connected with the liquid), or as a stationary shock front with $u_{\perp 1} = -u_s$ (observer connected with the shock front).

$d_s \geq 0.7$ nm. Since moderate shockwaves in water propagate approximately at the speed of sound in water, the transition time of the shockwave pressure is $t_t \geq d_s/c_0 \approx 0.5$ ps. Time of diffusion of magnetic field out of the shockwave transition region is approximately:

$$t_D = \sigma\mu_0 L^2 \qquad [\text{s}], \tag{4.2}$$

where σ [S·m^{-1}] is liquid conductivity and L [m] is the region characteristic dimension. Using $L = d_s$, and $\sigma = 4$ S·m^{-1} (maximum used liquid conductivity), equation (4.2) gives $t_D = 2\cdot10^{-24}$ s $\ll t_t$, i.e. diffusion of magnetic field would be much faster than liquid compression by the shockwave. Furthermore, the magnetic Reynolds number, which gives an estimate of the effects of magnetic advection to magnetic diffusion, is also much less than unity at considered conditions. It is defined by

$$R_m = \sigma\mu_0 Lu \quad [-], \tag{4.3}$$

where u [m·s^{-1}] is liquid velocity. It is less than 100 m·s^{-1} at moderate shockwave pressures in water. Considering $L < 1$ mm (maximum observed shockwave radius), the Reynolds number is $R_m < 10^{-11}$. This gives the evidence of no magnetic advection.

However, electric field has to be considered in the case of shockwaves propagating in the vicinity of corona-like discharges, because electric stress at the shock front can form a significant part of the total pressure. The Rankine-Hugoniot jump conditions of electrohydrodynamic shockwave supplemented by the Poynting vector are given by (see in more detail Appendix 1):

the conservation of mass and charge:

$$[\rho u_\perp]_1^2 = 0, \quad [j_\perp]_1^2 = -\frac{\partial \xi}{\partial t}, \tag{4.4) (4.5}$$

the conservation of momentum:

$$\rho u_\perp [u_\perp]_1^2 + [p]_1^2 - \frac{\varepsilon_0}{2}\left[\varepsilon_r\left(E_\perp^2 - E_{||}^2\right)\right]_1^2 = 0, \tag{4.6}$$

$$\rho u_\perp \left[\vec{u}_{||}\right]_1^2 - \left[\varepsilon_0\varepsilon_r E_\perp \vec{E}_{||}\right]_1^2 = \vec{0}, \tag{4.7}$$

the conservation of energy:

$$\left[\rho u_\perp\left(e + \frac{p}{\rho} + \frac{1}{2}u_\perp^2 + \frac{1}{2}u_{||}^2\right) + \vec{E}_{||} \times \vec{H}_{||}\right]_1^2 = 0, \tag{4.8}$$

and boundary conditions of electric and magnetic fields:

$$[D_\perp]_1^2 = \xi, \quad \left[\vec{E}_{||}\right]_1^2 = 0, \tag{4.9) (4.10}$$

$$\left[\vec{H}_{||}\right]_1^2 = 0, \quad [B_\perp]_1^2 = 0. \tag{4.11) (4.12}$$

Meaning of the used symbols is as follows: $[a]_1^2 = a_2 - a_1$, ρ is the liquid density, $\vec{u}$ is the liquid velocity vector relative to the shock front, symbol $\perp$ resp. $||$ represents the part of a vector perpendicular resp. tangential to the shock front; tangential vectors need not be parallel in all cases, $\vec{j}$ is the current density, ξ is the surface charge density, t is time, p is pressure, ε_0 is the vacuum permittivity, ε_r is the liquid relative permittivity, $\vec{E}$ is the electric field vector, e [J·kg^{-1}] is the liquid internal energy per kg, $\vec{H}$ is the magnetic field vector, $\vec{D} = \varepsilon_0\varepsilon_r\vec{E}$ and $\vec{B} = \mu_0\vec{H}$ (see Figure 33). This system of equations can be further simplified, when some obvious presumptions are accepted. No charge accumulates on the shock front means, that surface charge $\xi = 0$. Then from the equation (4.9) it follows that $\varepsilon_{r1}E_{\perp1} = \varepsilon_{r2}E_{\perp2}$. When there is no changing magnetic field on the shock front, the tangential parts of electric field on both sides of shock front equals each other according to (4.10). Hence, the

second term on the left side of the equation (4.7) $\left[\varepsilon_0\varepsilon_r E_\perp \vec{E}_{||}\right]_1^2$ equals to zero, and thus, $\vec{u}_{||}$ is also the same on both sides of the shockwave. Next, from equations (4.10) and (4.11) it follows that the tangential parts of the E and H vectors do not change over the shock front. Therefore, the product $\vec{E}_{||} \times \vec{H}_{||}$ can be removed from the equation (4.8). The system of equations (4.4) – (4.12) reduces to:

the conservation of mass and charge:

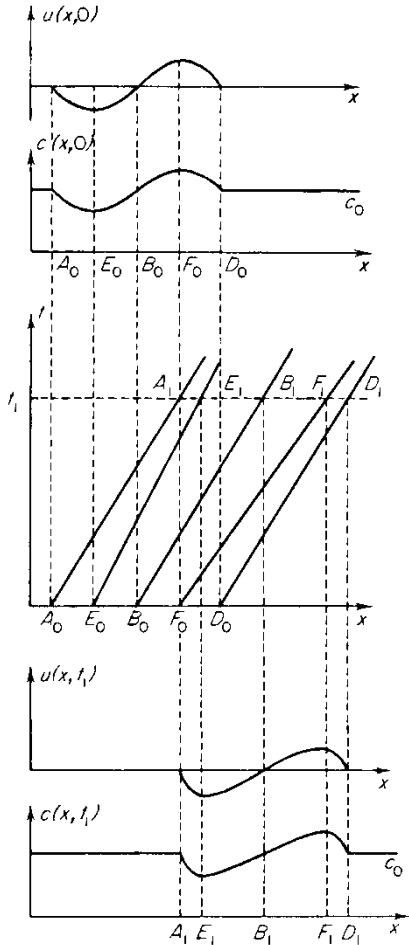$$[j_\perp]_1^2 = 0, \quad [\rho u_\perp]_1^2 = 0, \tag{4.13}\ (4.14)$$

the conservation of momentum:

$$\rho u_\perp [u_\perp]_1^2 + [p]_1^2 - \frac{\varepsilon_0}{2}\left[\varepsilon_r\left(E_\perp^2 - E_{||}^2\right)\right]_1^2 = 0, \tag{4.15}$$

$$\rho u_\perp \left[\vec{u}_{||}\right]_1^2 = \vec{0}, \tag{4.16}$$

the conservation of energy:

$$\left[e + \frac{p}{\rho} + \frac{1}{2}u_\perp^2\right]_1^2 = 0, \tag{4.17}$$

and boundary conditions of electric and magnetic fields:

$$[D_\perp]_1^2 = 0, \quad \left[\vec{E}_{||}\right]_1^2 = 0, \tag{4.18}\ (4.19)$$

$$\left[\vec{H}_{||}\right]_1^2 = 0, \quad [B_\perp]_1^2 = 0. \tag{4.20}\ (4.21)$$

The equations (4.14) - (4.17) are then the same as that used in hydrodynamics, with exception of the term $-\frac{\varepsilon_0}{2}\left[\varepsilon_r\left(E_\perp^2 - E_{||}^2\right)\right]_1^2$ in the equation (4.15). The Rankine-Hugoniot relationships across curved shocks are the same as those for a plane shocks, even for a very small radii of curvature [61].
The shockwave discontinuity develops due to nature distortion of the waveform in a traveling wave of finite amplitude. The qualitative character of the phenomena is graphically explained in the Figure 34, where the motion of a simple wave traveling to the right is depicted. The initial profiles of the liquid velocity $u(x, 0)$ and of the speed of sound $c(x, 0)$ are shown at the top. The straight lines in the center plot are so called C_+ characteristics, which show propagation of small disturbances in the direction of the x axis from each point on the axis. Their slope is determined by the liquid velocity and the speed of sound: $dx/dt = u + c$. The C_+ characteristics which start in the points A_0, B_0, and D_0 (where $u = 0$ so that $dx/dt = c_0$) emerge parallel to each other, and also parallel to the other C_+ characteristics (which

Figure 34 Propagation of a wave traveling to the right. The waveforms at the top indicate initial velocity and speed of sound profiles. The C_+ characteristics are depicted at the center, and distorted profiles at t_1 are shown in the bottom plot [60].
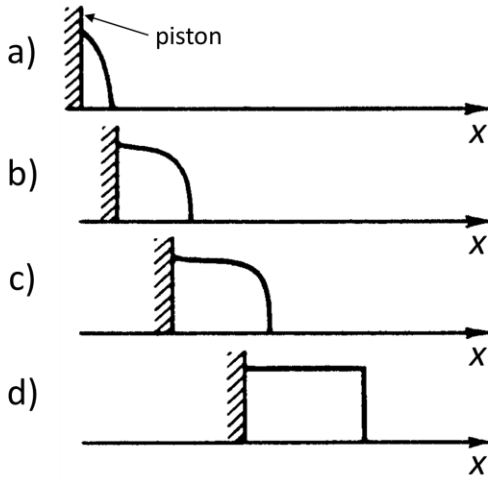
Figure 36 Gradual steepening of the velocity profile in a compression wave generated by an accelerating piston; (a) – (c) formation of the wave and its progressing distortion, (d) discontinuity - the final shape of the velocity profile **[60]**.

are not drown for clearance of the picture), starting in the points on the x axis belonging to the undisturbed region. The position of the C_+ characteristics in the time t_1 determines the liquid velocity and speed of sound profiles $u(x, t_1)$ and $c(x, t_1)$ in the time t_1, which are graphically constructed in the bottom of the Figure 34. It can be seen, that while front (D) and the back (A) of the wave adjacent to the undisturbed regions, where $u = 0$ and $c = c_0$, have been displaced along the x axis by distances equal to $c_0 t_1$, the relative positions of the maxima and minima are different. The profiles have been distorted. The steepness of the compression waveform increases with time, as it is shown in the Figure 36, where development of the velocity profile of a pressure wave generated by an accelerating piston is depicted. The C_+ characteristics approach each other and tend to intersect. When it happens, the discontinuity (shockwave) of velocity as well as of pressure is developed (Figure 36d).

The distance necessary for the formation of a plane shockwave can be estimated by [62]:

$$d = \frac{\rho_0 c_0^3}{\frac{\delta p}{\delta t}\left(1+\frac{1B}{2A}\right)} \quad \text{[m]}, \qquad (4.22)$$

where ρ_0 [kg·m^{-3}] and c_0 [m·s^{-1}] are the liquid density and the speed of sound at normal pressure, $\delta p/\delta t$ [Pa·s^{-1}] is the slope of the initial pressure, and B/A is parameter. For distilled water at 293 K the $B/A = 5.0$.
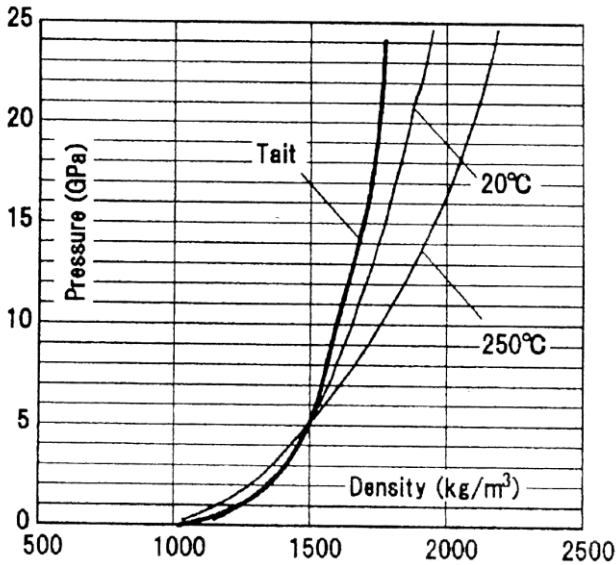
Figure 35 Relations between pressure and density of water at pressures up to 25 GPa. The approximation given by the Tait equation is satisfying at pressures up to 5 GPa **[61]**.

Equation of state of water

The Tait's equation is often used for its simplicity as the approximation of relation between pressure and density in water. The Tait's equation is given by [61]:

$$\frac{p+A_w}{p_0+A_w} = \left(\frac{\rho}{\rho_0}\right)^n, \qquad (4.23)$$

where p [Pa] and ρ [kg·m^{-3}] are the pressure and the liquid density, $p_0 = 0.1$ MPa and ρ_0 [kg·m^{-3}] is the liquid density at p_0 and 293 K (initial condition), A_w and n are constants. For $p < 2.5$ GPa, $A_w = 296.3$ MPa and $n = 7.415$.

Comparison of the measured data and the results obtained by the Tait's equation is plotted in the Figure 35. It is possible to embed the equation (4.23) into the equations

(4.14) − (4.17) and so to find direct relations among velocities, pressures and internal energies. If an observer moves with the velocity $-u_s$ of the shock front into a region where the liquid is quiescent and has density ρ_0, the incoming relative velocity with respect to the observer is $u_{\perp 1} = u_s$. If the liquid velocity behind the shock front is $-u_p$ with respect to the quiescent liquid ahead of the shock front (the "piston" velocity), the outgoing relative velocity with respect to the shock front (to the observer) is $u_{\perp 2} = u_s - u_p$. If the pressure, density and liquid velocity ahead and behind the shock front are labeled according to the Figure 33, the equations (4.14) - (4.17) can be re-written into a more useful form as (see in more detail Appendix 2):

the conservation of mass:

$$\rho_2(u_s - u_p) = \rho_1 u_s, \tag{4.24}$$

the velocities u_s and u_p:

$$u_p^2 = \frac{p_2 - p_1 + p_{E2} - p_{E1}}{\rho_1}\left(1 - \frac{\rho_1}{\rho_2}\right), \tag{4.25}$$

$$u_s^2 = \frac{p_2 - p_1 + p_{E2} - p_{E1}}{\rho_1\left(1 - \frac{\rho_1}{\rho_2}\right)}, \tag{4.26}$$

where $p_E = -\frac{1}{2}\varepsilon_0\varepsilon_r\left(E_\perp^2 - E_{||}^2\right)$. The relations (4.25) and (4.26) show that liquid velocity and propagation speed of a shockwave can be enhanced by electric field on its shock front.
The conservation of energy requires:

$$e_2 - e_1 = \frac{1}{2}(p_1 + p_2)\left(\frac{1}{\rho_1} - \frac{1}{\rho_2}\right) + \frac{1}{2}(p_{E2} - p_{E1})\left(\frac{1}{\rho_2} + \frac{1}{\rho_1}\right). \tag{4.27}$$

Derivation of the equations (4.25) - (4.27) is described in the Appendix 2. If a shockwave propagates in undisturbed water at atmospheric pressure, then $p_1 = p_0$ (= 0.1 MPa), $\rho_1 = \rho_0$ (= 998.2 kg·m^{-3}), and temperature change across the shock front can be neglected, the Tait's equation of state of water (4.23) can be applied. The velocities u_s and u_p are then given by:

$$u_p^2 = \frac{p_2 - p_1 + p_{E2} - p_{E1}}{\rho_1}\left[1 - \left(\frac{p_2 + A_w}{p_1 + A_w}\right)^{\frac{-1}{n}}\right], \tag{4.28}$$

$$u_s^2 = \frac{p_2 - p_1 + p_{E2} - p_{E1}}{\rho_1\left[1 - \left(\frac{p_2 + A_w}{p_1 + A_w}\right)^{\frac{-1}{n}}\right]}, \tag{4.29}$$

$$e_2 - e_1 = \frac{(p_1 + p_2)}{2\rho_1}\left(1 - \left(\frac{p_2 + A_w}{p_1 + A_w}\right)^{\frac{-1}{n}}\right) + \frac{(p_{E2} - p_{E1})}{2\rho_1}\left(1 + \left(\frac{p_2 + A_w}{p_1 + A_w}\right)^{\frac{-1}{n}}\right). \tag{4.30}$$

Geometrical interpretation of the change of the internal energy is depicted in the Figure 37, where the isentrope (P) and the Hugoniot (H) curves starting at the same initial point (A) are plotted. The Hugoniot curve, which represents the dependence of the shockwave pressure p on the liquid specific volume $V = 1/\rho$, always lies above the isentrope and isotherm at such conditions. Equation (4.27) for the Hugoniot curve (when $p_{E1} = p_{E2}$) shows that the increase in the specific internal energy $e_2 - e_1$ during the shock compression of the liquid from the state A to the state B is equal to the area delimited by M-A-B-N, which is hatched with horizontal lines. If the liquid is compressed isentropically from state A to state Q then the work performed is numerically equal to the area delimited by M-A-Q-N, which is hatched with vertical lines. This area also gives the increase in the internal energy of the liquid

44
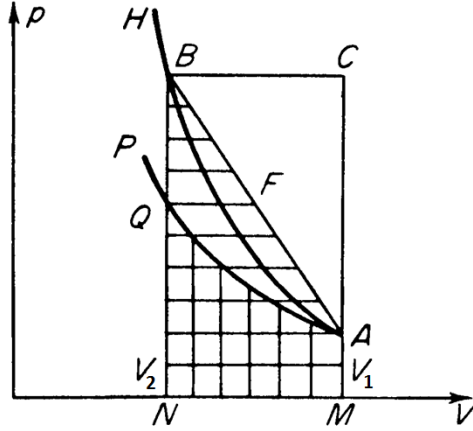
Figure 37 Geometrical interpretation of the energy increase across a shock wave. *H* is the Hugoniot curve and *P* is the isentrope **[60]**.

$$e_Q - e_1 = -\int_{V_1}^{V_2} p\, dV, \tag{4.31}$$

when the integration is performed at constant entropy. For shifting liquid to the final state *B* it is necessary to heat it at constant volume V_2 by adding an amount of heat numerically equal to the area *A-B-Q*. Since the change of the internal energy is generally given by the fundamental thermodynamic relation [63]:

$$de = T\, dS - p\, dV, \tag{4.32}$$

it means that the area *A-B-Q* determines the entropy increase of the liquid by the shockwave compression. Hence, the rest of the internal energy is

$$e_2 - e_Q = \int_{S_1}^{S_2} T\, dS = T_A(S_2 - S_1), \tag{4.33}$$

where T_A is a certain average temperature lying between *Q* and *B*, and $V = V_2$. It means that temperature at shock front with the appropriate liquid density is always higher than temperature of the liquid compressed isentropically (or isothermally) to the same density. For this reason, using of the Tait's equation (4.23), which is thermally independent, is not perfect. However, at moderate pressures up to ~1 GPa, the temperature change can be neglected, and the equations (4.28) – (4.30) are valid [64].

Electric field at shock front

Since shockwaves represent discontinuous change of liquid density, they are naturally accompanied by discontinuous change of liquid permittivity, as follows from the equation (2.17). At normal pressure, when water permittivity is ε_0, and water density ρ_0, the derivative

$$\frac{\partial \varepsilon_r}{\partial \rho} = \frac{1.5\varepsilon_{r0}}{\rho_0}.$$

Then, water relative permittivity as a function of density is given by

$$\varepsilon_r = \varepsilon_{r0}\frac{\rho}{\rho_0}. \tag{4.34}$$

When the transition time of pressure at shock front t_t is much shorter than the dielectric relaxation time τ given by (2.32), then, because $\nabla \cdot \vec{D} = 0$, the ratio of electric fields is determined by

$$\frac{E_{\perp 1}}{E_{\perp 2}} = \frac{\varepsilon_{r2}}{\varepsilon_{r1}} = \frac{\rho_2}{\rho_1}. \tag{4.35}$$

Since relation (4.35) gives only the ratio of electric fields in front of and behind a shock front, magnitude of electric filed has to be determined for the concrete geometry.

In the opposite case, when the transition time t_t is much larger than the relaxation time τ, the electric field is distributed according to distribution of the liquid conductivity. Although conductivity of aqueous NaCl solutions also depends on pressure, it changes little with increasing pressure bellow 1.5 GPa [65].

Conclusion

The derived relations (4.28) - (4.30) link together pressure, liquid velocity and electric field at a shock front. These relations show that electric field at a shock front can enhance liquid velocity u_p and propagation speed u_s of the corresponding shockwave. The ratio of electric fields in front of and behind a shock front is given by (4.35) at slightly conductive water solutions ($t_t \ll \tau$). In the opposite case ($\tau \ll t_t$) it can be considered to be uninfluenced by a shockwave (<1.5 GPa). Magnitude of electric filed has to be determined for a concrete geometry. The relations (4.28) - (4.30) are valid when influence of temperature rise in a shock front can be neglected, i.e. at shock pressures up to ~1 GPa.

4.2 Relationship of shockwaves and corona-like discharges

Generation of shockwaves by spark discharges in water is well known phenomenon with important practical application (e.g. in shockwave lithotripsy). However, shockwaves are generated also by low-current corona-like discharges. The appearance of shockwaves in vicinity of corona-like discharges has been mentioned already in the Chapter 3, where shockwaves are visible as shadows in the Figure 19a,
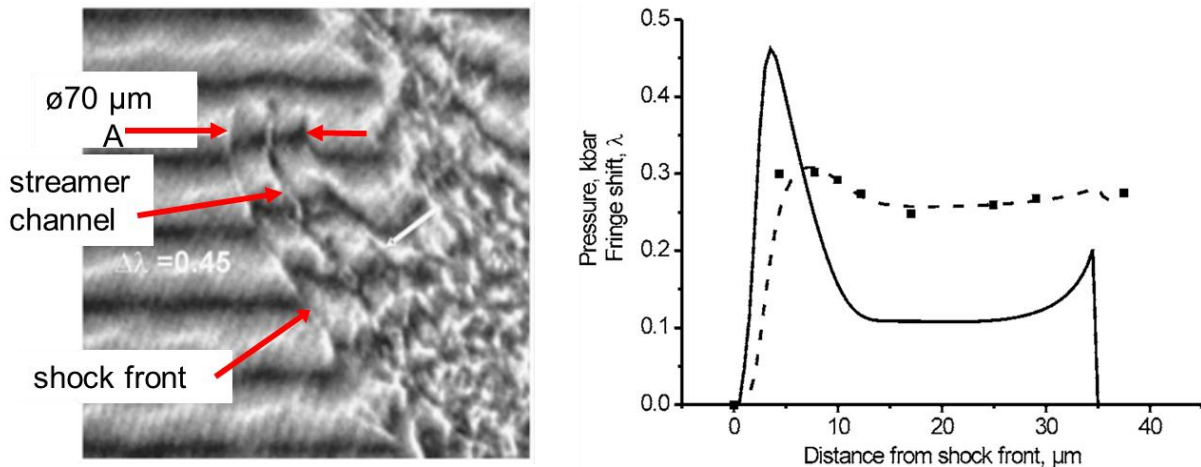

Figure 38 Interferogram of an inactive positive streamer and its surrounding pressure field (left). Fringe shifts and the corresponding pressure profile of the inactive streamer at the position A (right). The anode-cathode distance was 10 mm, voltage 20 kV and water conductivity 450 μS·m⁻¹. Gating time of the used ICCD camera was 3 ns, and the laser wavelength was 532 nm **[47]**.

46

and in the Figure 21a.

In the case of the positive primary supersonic streamers, shockwaves are generated in the form of many Mach cones, as there are often many primary streamers on the anode tip. Then these shockwaves compose into a few spherical shockwaves with their center on the anode tip.

Pressure distribution around positive secondary streamers was studied in more detail in [47] by means of Mach-Zehnder interferometry. Evaluation of fringe shifts in an interferogram of the streamer surroundings leads to the desired pressure profile. The authors distinguished two kinds of streamers: active and inactive. Active streamers had been propagating, when the diagnostic laser was triggered. Active streamers could be recognized by the conical shape (Mach cone) of the shock front evolving from them. Inactive streamers had (nearly) stopped propagating, when the laser was triggered, and hence, spherical shape of the pressure wave at the streamer head was observed. Conductivity of water solution used in these experiments varied from 200 μS·m^{-1} (distilled water) to 80 mS·m^{-1} (tap water). Interferogram of positive inactive streamer surroundings in water with conductivity of 450 μS·m^{-1} is depicted in the Figure 38, where plot of fringe shift with appropriate pressure profile is also added. The peak pressure of the shock front, when it reached radius of 35 μm, was 46 MPa. The streamer propagation speed was found to be about 25 km·s^{-1} according to the diameter of the cylindrical pressure wave at two different positions along the streamer, and the distance between these positions. Shockwaves generated by negative coronas are generally weaker, because negative streamers are often subsonic. Thus, spherical shockwaves or weak pressure waves instead of Mach cones are often emitted from the tip of each propagating streamer, as is depicted in the Figure 39. The waves are not emitted from sides of negative streamers [57], as in the case of positive streamers (Figure 38).

As it will be shown in the experimental part 2, propagation of plasma discharges in water solutions with different conductivities is related to the penetration of plasma into water volume examined in the experimental part 1. It means that formation of streamers (negative or positive) is difficult at higher conductivities. Therefore, shockwaves are thus better produced by fast expanding bubbles filled with plasma, than by propagating thin plasma channels.
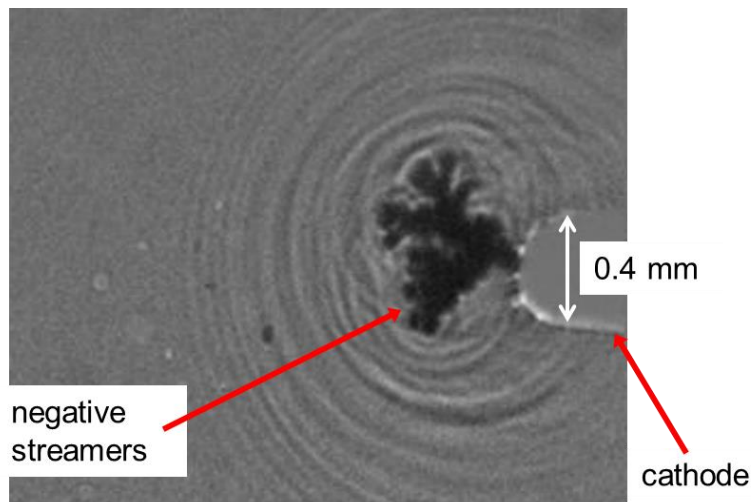
Figure 39 Shadowgraphy image of spherical pressure waves around negative discharge in water. The anode-cathode voltage was 40 kV and water conductivity was 5 mS·m^{-1}. Gating time of the used camera was 20 ns **[57]**.

4.3 Experimental part 2

The main purpose of experiments described in this chapter was studying of pressure field in vicinity of corona-like discharges in distilled water and in highly conductive NaCl water solutions with conductivities up to $3.8\ \text{S·m}^{-1}$. The Mach-Zehnder interferometer was used for the pressure field detection. This required changing the glass capillary for a glass cuvette with plan-parallel windows.

Experimental setup

The experimental setup of the second experiment is depicted in the Figure 40. The pulse power supply was based on the same principle as in the first experiment; it consisted of a high voltage capacitor C, which was charged up to 50 kV by a high voltage DC power supply (Glassman WR125R2-220). The discharge current had to be limited by a high voltage resistor R (a battery of Allen Bradley/Willow Technologies high voltage resistors) protecting the used cuvette from damage just in the case of liquid breakdown. The value of R was changed according to actual water solution conductivity. The pressurized spark gap was used as a high voltage switch again; it was triggered by decreasing of the pressure in the spark gap. The investigated volume consisted of the uncovered glass cuvette, which was filled (by injection needle) with the conductive water solution. The high voltage electrode was immersed in the liquid; it was stainless-steel wire insulated with exception of the sharpened tip. The lower, grounded electrode was formed by a stainless-steel slab, which also formed the base of the cuvette. The voltage across the electrode gap was measured by the high voltage probe (North Star VD-100), and the discharge current was measured by the current monitor (Pearson probe, model 4997, sensitivity $10\ \text{mV·A}^{-1}$). Both voltage and current signals were registered by the oscilloscope (Tektronix TDS 3054C), which was triggered by the rising/falling edge of the signal from the high voltage probe. Voltage on the 10 Ω resistor was used for indirect triggering of the high-speed camera (Phantom v710). Since it was necessary to insulate the high-speed camera from the high voltage circuit, an optocoupler was inserted between the resistor and the camera. Although the lower electrode was not directly grounded, the voltage on the 10 Ω resistor was negligible in comparison with the voltage on the high voltage (upper) electrode. Therefore, the high voltage measurement was practically uninfluenced by the voltage loss on the resistor. The Mach-Zehnder interferometer used the 532 nm pulsed laser (Elforlight, SPOT-10-200-532) as a source of coherent radiation. This laser produces pulses 6.2 μJ/1.76 ns at the maximum repetition rate $5·10^4\ \text{s}^{-1}$. Diameter of the beam splitters was of $\varnothing$65 mm. Image on the camera CMOS chip was created by a set of lenses with diameter of $\varnothing$80 mm, and with the total focal length of 107 mm. The distance between the cuvette and the set of lenses was set to the smallest achievable distance of 149 mm; this enabled the lenses to collect the maximum of light bended on strong inhomogeneities in the liquid filling of the cuvette. The high-speed camera was equipped with the interference filter tuned on the laser wavelength 532 nm, which suppressed most of the light emitted by the discharge.

Interferogram analysis

Generally, optical interferometry is based on interference of reference (direct) and measuring (propagating through the analyzed optical inhomogeneity) light rays with different phases. The phase shift is caused by their propagation through regions with different refraction indexes. The interference can be constructive or destructive, which leads to creation of bright and dark regions on the plane, where they interfere (CMOS chip of the camera). When mirrors and beam splitters of the interferometer are adjusted appropriately, and when both the reference and measuring beams propagate through optically homogeneous environment, then the interference pattern contains parallel fringes only [66] with adjustable pitch. Any optical inhomogeneity in one of interfering beams results in a shift of fringes; this shift can be used for evaluation of the phase shift in each point of the interference pattern.
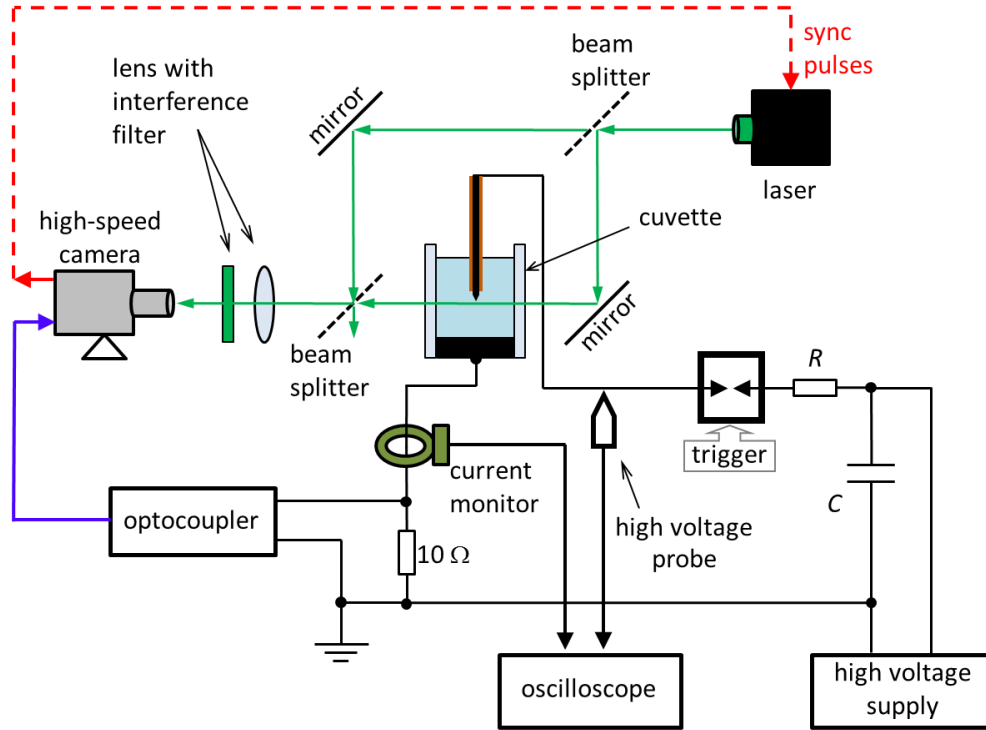
Figure 40 Experimental setup of the apparatus used for detection of pressure field around corona-like discharges in liquid water solution in a glass cuvette (top). Photograph of the Mach-Zehnder interferometer with the cuvette.

When a reference ray propagates through undisturbed region with refraction index n_0, and the measuring ray propagates through a medium with refraction index n, then the phase shift between the two rays expressed in number of wavelength, which emerges on a small distance dx, is given by

$$dS = \frac{1}{\lambda}\delta n dx \quad [\text{-}], \tag{4.36}$$

where λ [m] is the radiation wavelength in vacuum, much shorter than the cutoff wavelength in the probing medium , and $\delta n = n - n_0$. Total shift δS between rays l_0 (reference ray) and l_1 (measuring ray)

in the Figure 41a, where the ray l_1 propagates through the cylindrically symmetric inhomogeneity between points $A = [x_A, y_1]$ and $B = [x_B, y_1]$, is given by integration of (4.36) as

$$\delta S = \frac{1}{\lambda} \int_{x_A}^{x_B} \delta n(x, y_1) dx = \frac{2}{\lambda} \int_{0}^{x_B} \delta n(x, y_1) dx \quad [\text{-}]. \tag{4.37}$$

Shift by one fringe in the interference pattern means that $\delta S = 1$. The equation (4.37) can be numerically solved by the onion peeling method. This method can be used every time, when an inhomogeneity with cylindrical or spherical symmetry is studied [66]. The method is based on division of the inhomogeneity to co-centric circular layers, and subsequent progressive calculation of mean refractive indexes in each layer. The equation (4.36) for the ray l_1 propagating through the first layer in the Figure 41b gives $\delta S_1 = \frac{1}{\lambda} \delta n_1 d_{11}$, which allows calculation of

$$\delta n_1 = \lambda \frac{\delta S_1}{d_{11}}.$$

Once δn_1 is known, it is possible to calculate δn_2:

$$\delta n_2 = \frac{1}{d_{22}} (\delta S_2 \lambda - \delta n_1 d_{12}).$$

This process can be generally written in a form of recursion formula:

$$\delta n_k = \frac{1}{d_{k,k}} \left(\delta S_k \lambda - \delta n_1 d_{1,k} - \delta n_2 d_{2,k} - \cdots - \delta n_{k-1} d_{k-1,k} \right). \tag{4.38}$$

Since interferograms provide information about deviations of the refractive index inside an inhomogeneity, it is possible to calculate profile of liquid density and hence, the appropriate pressure profile. Relation between liquid density and its refractive index is given by the Lorentz-Lorenz formula [67]:

$$\frac{n^2-1}{n^2+2} = \frac{4\pi \alpha N_A}{3M} \rho, \tag{4.39}$$

with n the refractive index of liquid, M [kg·mol^{-1}] is the liquid molar mass, $N_A = 6.022 \cdot 10^{23}$ mol^{-1} is the Avogadro constant, ρ [kg·m^{-3}] is the liquid density, and α [m^3] is the liquid polarizability. Since the experiments described in the next chapter were conducted in water solutions with different conductivities, i.e. with different salinities, the appropriate polarizabilities must have been initially calculated for each solution separately. The polarizability at normal pressure, but at different salinities and temperatures is given by

$$\alpha_S = \frac{n_S^2-1}{n_S^2+2} \frac{3M_S}{4\pi N_A \rho_S}, \tag{4.40}$$

where the molar mass $M_S = M_S(S_a)$, the liquid density $\rho_S = \rho_S(T, S_a)$, and the refractive index $n_S = n_S(T, S_a, \lambda)$ are functions of salinity S_a, temperature T, and wavelength λ. These functions and determination of salinity are described in Appendix 3 by empirical formulas (A3.1) - (A3.4).
Once the polarizability is known, the equation (4.39) enables calculation of the liquid density from the deviation of refractive index derived by (4.38):

$$\rho_S + \delta \rho = \frac{(n_S+\delta n)^2-1}{(n_S+\delta n)^2+2} \frac{3M_S}{4\pi N_A \alpha_S}. \tag{4.41}$$

Then, if δp is positive, the Tait's equation (4.23) can be used for calculation of the liquid pressure, with $\rho_0 = \rho_s(T, S_a)$. In the opposite case, water bulk modulus $K = 2.2$ GPa can be used for the liquid pressure linear approximation (from definition of bulk modulus):

$$\delta p \approx \frac{K}{\rho_s} \delta \rho. \tag{4.42}$$

Validity of this pressure estimation is problematic, especially when the calculated absolute pressure $p + \delta p$ is below the liquid vapor pressure (2.30), where potential cavitation can significantly influence both the bulk modulus and the refractive index of liquid.
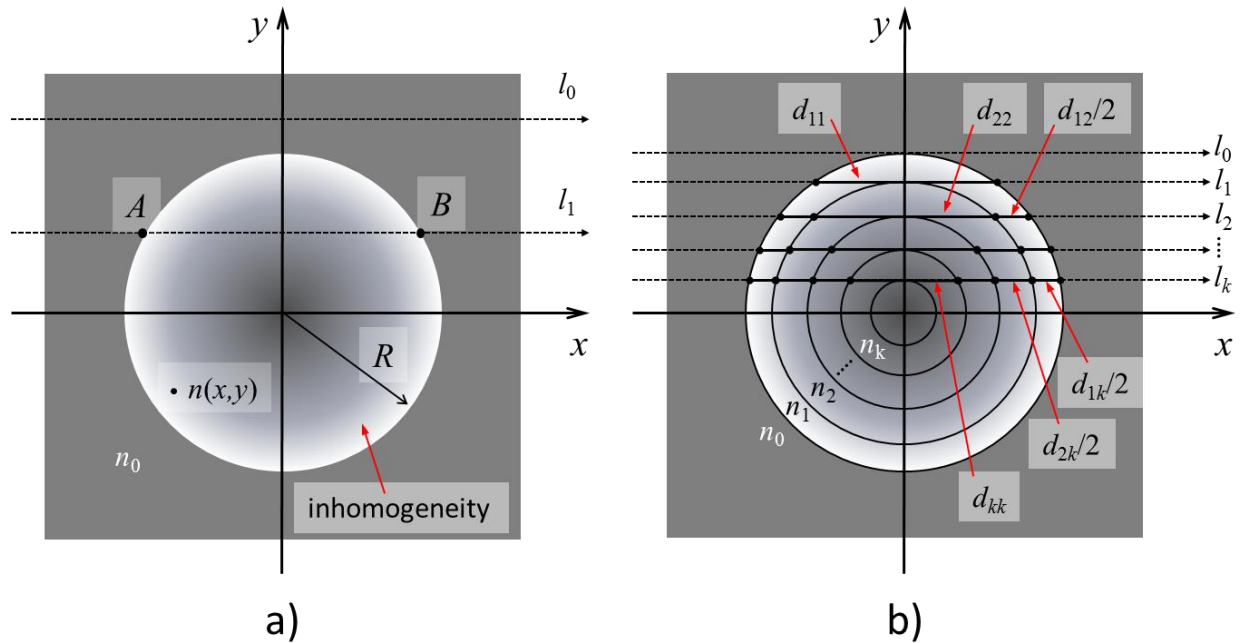
Figure 41 a) Cross section of a cylindrically symmetric inhomogeneity with radius R, and with refraction index n expressed by the gray scale (only for illustration), **b)** division of the inhomogeneity to co-centric circular layers used for the numerical solution of the equation (4.37).

Experiments with distilled water - positive needle electrode

Streamers in distilled water (positive as well as negative) form long filaments, which could extend to get out of the depth of field of the camera lens. Due to that in these experiments the cuvette with rectangular cross section 10x4 mm was used, when the shorter dimension was that along the propagating laser beam. Resistance of the resistor R was 10 kΩ; this value was with respect to the liquid conductivity (170 μS·m^{-1}) small enough. The capacity of the high voltage capacitor C was 10 nF and it was charged to 23 kV.

The gap size between electrodes in the cuvette was 6 mm in the first experiment. Radius of the needle electrode was approximately 15 μm. The measured temporary V-A waveforms are depicted on the left bottom of the Figure 42. The voltage waveform has relatively slow rise time, which corresponds to the time constant of the resistor $R = 10$ kΩ and the total load capacity of about 50 pF. Although capacity of
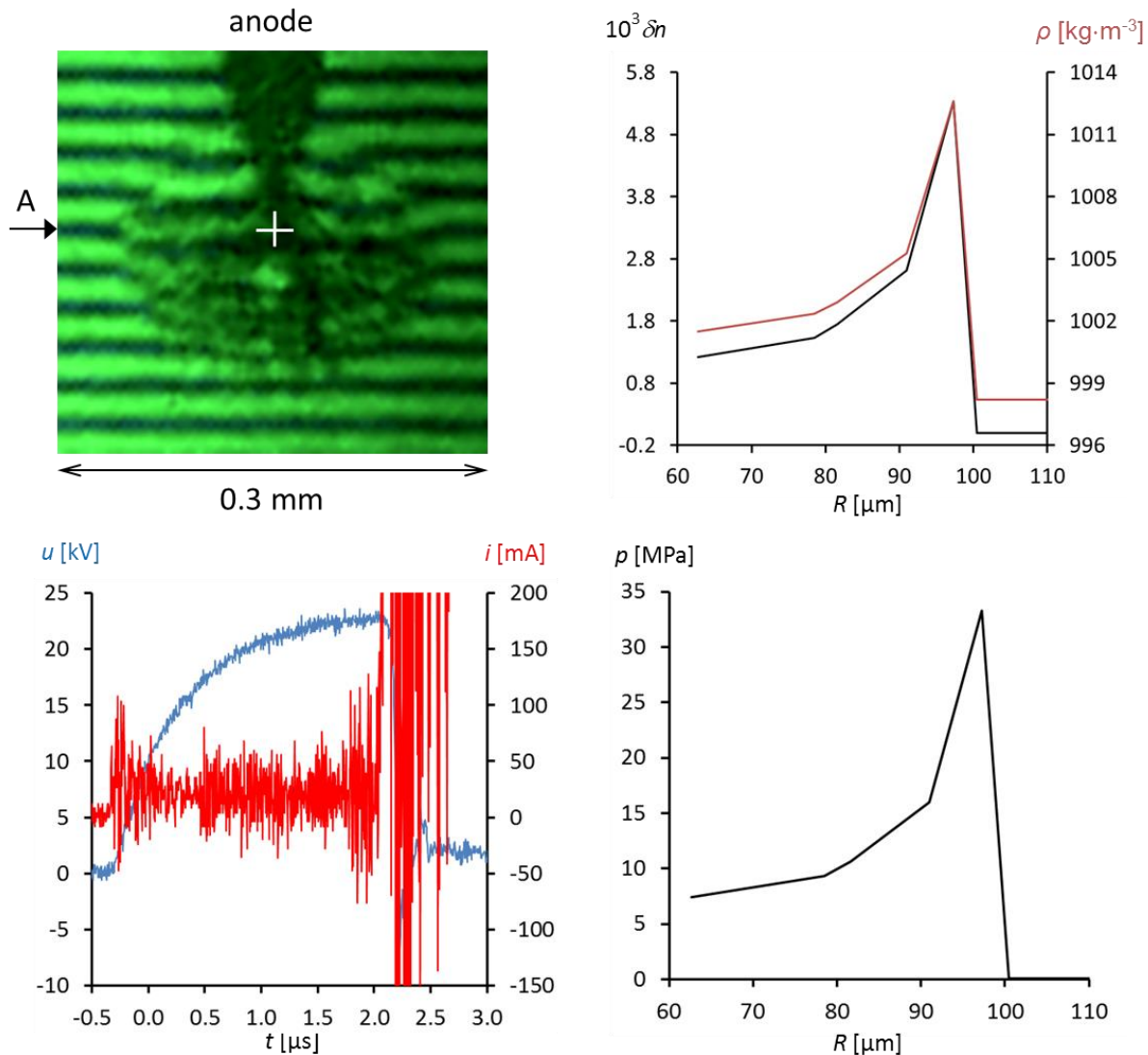
Figure 42 Interferogram of surroundings of primary streamers on a needle anode (top left), radial profiles of the refractive index deviations and of the liquid density at position A along fringes are plotted as a function of R (radial distance from the center of curvature) (top right), the radial pressure profile at position A of the interferogram (bottom right), and V-A temporal waveforms (bottom left). The cross in the middle of the interferograms lies on the axis of symmetry.

the high voltage probe was 25 pF only, the additional capacity of wire connections among the high voltage resistor, the probe, and the electrode in the cuvette provided probably the remaining capacity. The pre-discharge current waveform is typically noisy, as was discussed in the chapter 3.3. The final current jump was caused by the gap total breakdown, which happened 2.5 µs after the spark gap had switched.

The interferogram of a shockwave around primary streamers grown on the needle anode is shown on the left top part of the Figure 42. The edge of the spherical shockwave can be clearly recognized. Most of the primary streamers were located inside the sphere, but some of them protruded out of it, especially at the bottom of the sphere. These streamers had to be significantly supersonic. The shockwave was probably result of a composition of many elementary shockwaves produced by each primary streamer in a form of Mach cones, instead of expansion of one central cavity.

The radial profile (at position A along fringes) of deviations δn of refractive index calculated by the technique described in the previous chapter is plotted in the right top part of the Figure 42. The radial profile of density according to (4.41) is shown in the same graph, and the liquid pressure profile calculated with the help of the equation of state (4.23) is plotted in the right bottom part of the Figure 42. It turns out that the liquid peak pressure reached 33 MPa, and the shock front transition region had thickness $d_s = 2.7$ µm. If the propagation speed of the shock front was approximately $u_s \approx c_0$, then the shock transition time was $t_t = d_s/u_s = 1.82$ ns. This is much less than the dielectric relaxation time $\tau = 4.7$ µs given by the equation (2.32). Therefore, change of normal electric field on the shock front can be determined by the equation (4.35) – as it is shown below.

Before determination of the shock propagation speed, it is necessary to deal with electric field on the shock front first, as the equation (4.29) requires. The issue in this case is that the primary streamers are conductive, and hence, the electric field in the area is significantly inhomogeneous. Therefore, two extreme cases of distribution of electric field are discussed. In the first case, let's suppose that there are lot of primary streamers, the tips of which are so close to each other that they form conductive spherical surface with radius equal to the radius of the shock front, and with maximum potential of 23 kV. It possible to neglect the difference of the permittivities before and behind the shock front for the estimation
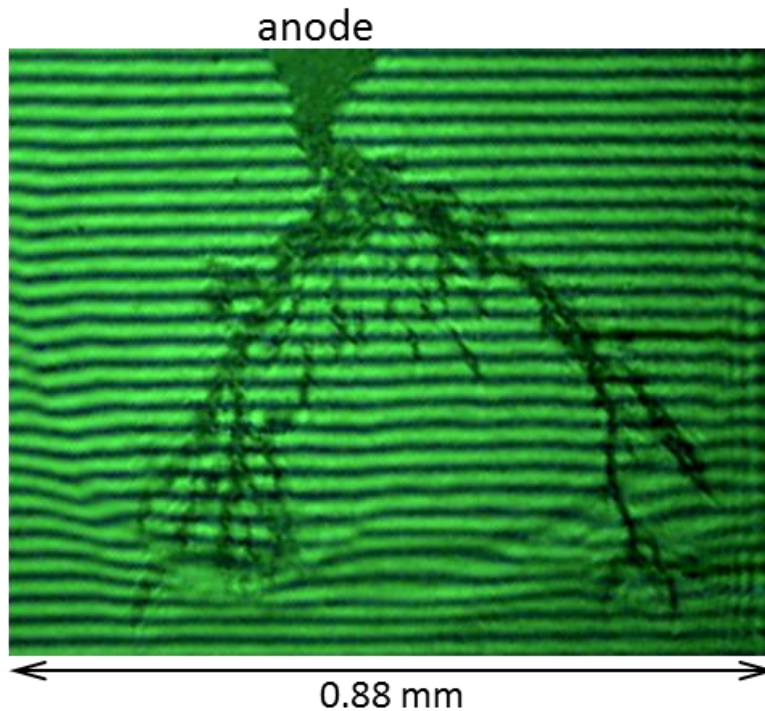

Figure 43 Interferogram of surroundings of corona secondary streamers in distilled water.

of electric field, because the permittivities differ by ~1.5 % only, as follows from the equation (4.34). Then, according to (2.11), the normal electric field on the spherical surface is $E_{\perp 1} = 72.98$ MV·m^{-1}. According to the equation (4.35), the ratio of densities before and behind the shock front determines normal electric field just behind the shock front to be $E_{\perp 2} = 71.85$ MV·m^{-1}, and resulting difference of the electric pressures $p_{E2} - p_{E1} = -\frac{1}{2}\varepsilon_0\varepsilon_r\left(E_{\perp 2}^2 - E_{\perp 1}^2\right) = 65.9$ kPa. This value is negligible in comparison with 33 MPa of water pressure at the shock front. The shockwave propagation speed and the liquid velocity behind the shock front according to the equations (4.28) and (4.29) are then $u_s = 1526$ m·s^{-1} and $u_p = 21.6$ m·s^{-1}.

In the second case, let's suppose existence of strong electric field on tips of the primary streamers. It can be estimated from the Figure 19b that average diameter of primary streamers is 3 μm. Normal electric field at the shock front located in the vicinity of streamer tip under the same conditions as in the previous case is according to (2.11) of the order of $E_{\perp 1} = 2.755$ GV·m^{-1} and $E_{\perp 2} = 2.712$ GV·m^{-1}. The appropriate difference of the electric pressures $p_{E2} - p_{E1} = 94$ MPa is a few times larger than water pressure at the shock front. The shockwave propagation speed and the liquid velocity behind the shock front are thus $u_s = 2989$ m·s^{-1} and $u_p = 42.4$ m·s^{-1} at presence of strong electric field. This allows the primary streamers to propagate in water at significantly supersonic speed even if no high-pressure area in front of the streamers´ tips is created. Nevertheless, the electric field around the primary streamers´ tips considered in the second case is high enough for ionization of water in liquid phase, and the transition to secondary streamers occurs. Therefore, the mechanism of supersonic propagation of primary streamers is temporary only.

In the Figure 43 the interferogram of pressure field around secondary streamers is depicted. Total breakdown happened 15.5 μs after the spark gap had switched. The pressure field is very complex; evaluation of pressure levels around streamer tips was impossible due to missing cylindrical or spherical symmetry, which is required by the onion peeling method. The interferogram shows a lot of branches emerging from plasma channels and formation of pressure waves in front of them. These pressure waves form a boundary of the streamer tips, similarly as the shockwave in the interferogram in the Figure 42 does. This can be explained by the equation (4.29), which shows strong dependence of pressure in shock front on the propagation speed of the shockwave. When propagation speed of a streamer tip exceeds the speed of sound, shockwave around the tip is established. Subsequent increase of the streamer propagation speed is accompanied by significant pressure increase in the shock front preceding the streamer tip; the streamer propagation speed is thus limited to sonic speeds. This phenomenon at zero electric field was verified by simulations of steady liquid flow around rigid tip with radius 1 μm emulating a streamer tip. The results are shown in the Figure 44. The simulations were done in Comsol Multiphysics software. The built in computational fluid dynamics module (CFD) uses the Tait's equation (4.23) at positive pressures as the liquid equation of state; the approximate relation (4.42) is used at negative pressures. For more information about the used CFD module see [68]. The simulations were performed at eight different speeds of the liquid flow expressed by the Mach number $M = v_1/c_1$, where v_1 resp. c_1 is speed of the liquid flow resp. speed of sound in front of shockwave or far from the solid tip (when a shockwave is not present). Pressure on the solid tip increases relatively slowly with increasing flow speed at $M < 1$. At $M > 1$ a shockwave is created, and pressure at the shock front and on the solid tip is much more sensitive to an increase of the flow speed (although real liquid water cannot sustain a high-negative pressure region at the tip side).

This fact again points to obvious differences between possible regimes of propagation of positive streamers. Propagation of fast positive streamers, which may propagate at speeds far beyond speed of sound in water, does not take place in a form of pushing liquid out of the streamer tip vicinity. Formation of conductive channel by ionization processes directly in liquid phase without any liquid movement is, hence, more probable mechanism of secondary streamer propagation [47].
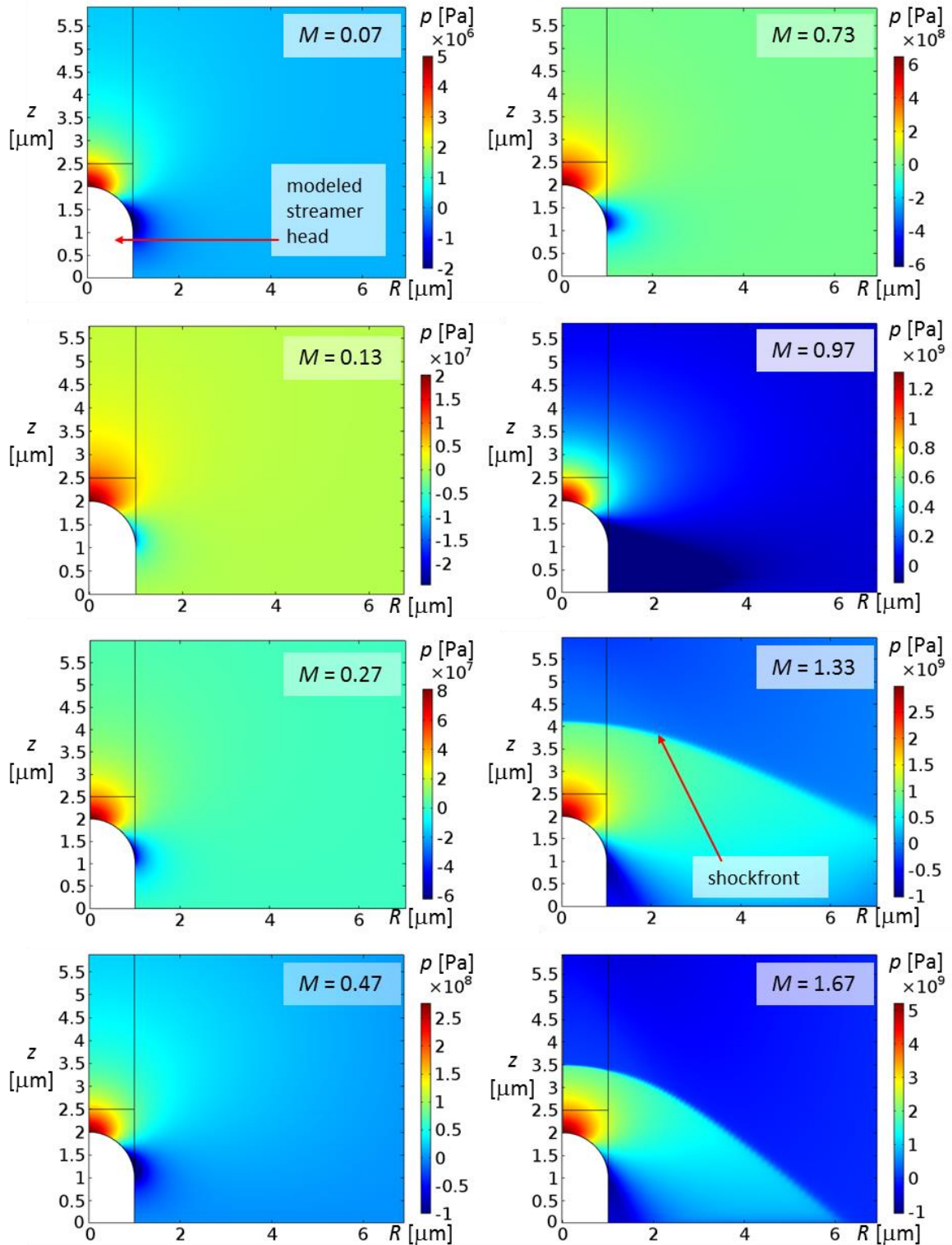
Figure 44 Simulations of steady liquid flow around rigid tip emulating a streamer tip at eight different speeds of the liquid flow expressed by the Mach number *M*. The geometry was modeled in cylindrical coordinates (*z* - axis of symmetry, *R* – radial distance); simulation was performed in Comsol Multiphysics software. The black lines ahead of the rigid tip are domain boundaries used to define mesh element size for the simulation only. Note an increasing exponent at the pressure scale.
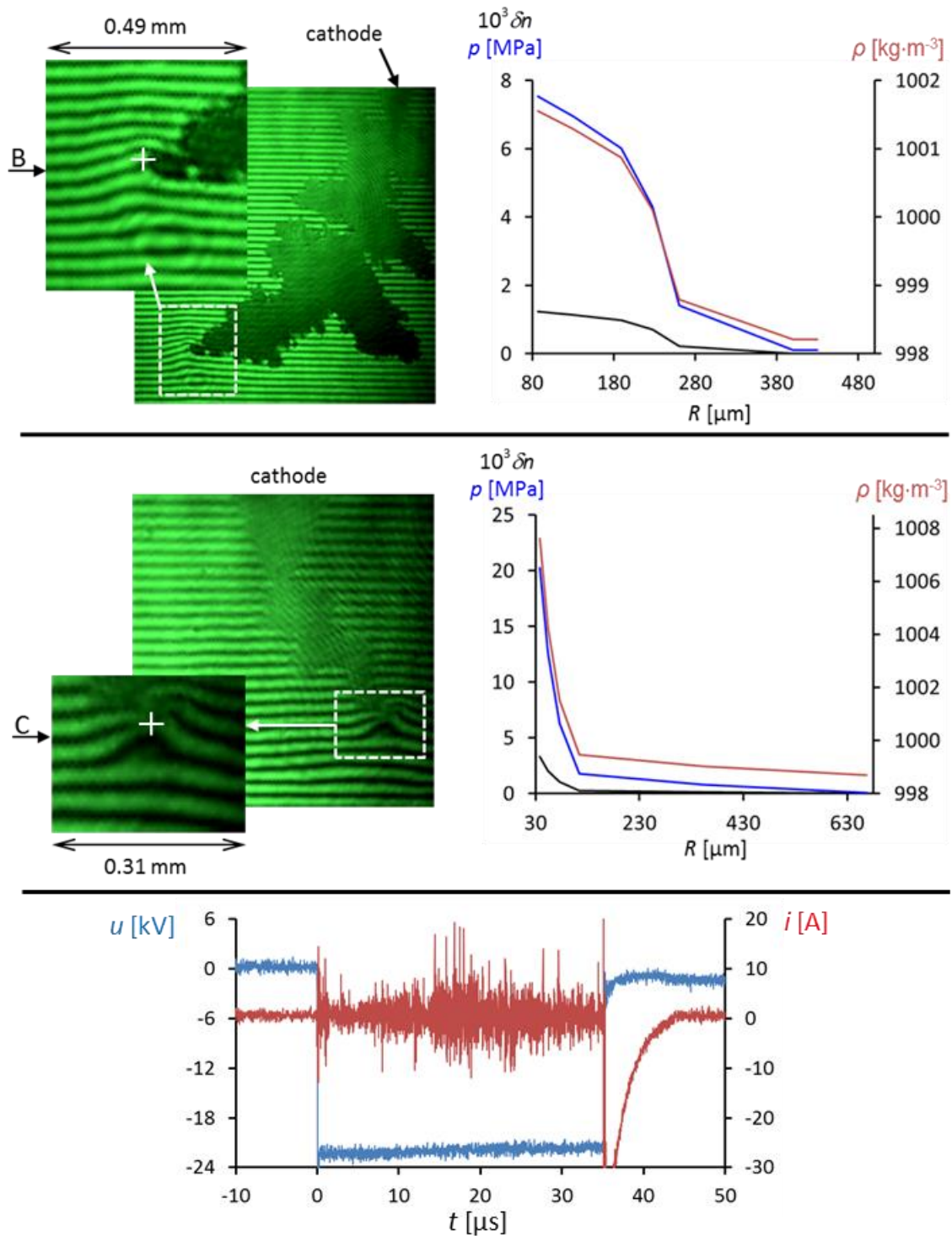
**Figure 45** Examples of interferograms of negative corona-discharges surroundings in distilled water (top and middle). Radial profiles of refractive index deviations, water density, and pressure at positions B and C along fringes are plotted as functions of *R* (radial distance from the center of curvature marked by the crosses); typical V-A temporal waveforms of negative corona discharge in the bottom.

Experiments with distilled water - negative needle electrode

Experiments with the negative needle electrode were conducted under the same conditions as in the case of the positive needle electrode. Two interferograms of negative corona discharges and their surroundings with attached radial profiles of refractive index deviations, liquid density, and liquid pressure are depicted in the top and middle parts of the Figure 45. The pressure waveforms are rather smooth, without any significant discontinuity comparable to that of the pressure waveform in the Figure 42. This gives evidence of subsonic streamer propagation speed. Moreover, the pressure profiles in the top and bottom plots in the Figure 45 bear witness to considerable differences between rise times in these two cases as well as between their peak pressures, which are probably consequence of unstable propagation speed of the captured streamers. The peak pressure in front of the streamer tip along the path C in the middle of the Figure 45 reached 20 MPa. Since the high pressure area has small dimensions (~100 μm), because pressure falls rapidly with increasing distance from the streamer tip as it has been shown in the Figure 44, the deviations of refractive index are noticeable near the streamer tips only. Although no shockwaves have been observed in conducted experiments, it does not mean that subsonic streamers cannot produce shockwaves. Simulation shown in the Figure 46 demonstrates formation of a transient shockwave around rigid tip in water, which is suddenly accelerated to the speed of 105 m·s^{-1} ($M = 0.07$) relative to the tip. The shockwave propagation velocity is supersonic (with respect to the incoming fluid), and hence, it moves away from the tip. After the shockwave has passed away, a steady state shown in the Figure 44 is established. While pressure on the tip propagating steadily at the speed of 105 m·s^{-1} reaches ~5 MPa only (Figure 44), pressure on the tip just after the fast acceleration to the same speed reaches ~165 MPa (Figure 46).

The V-A temporal waveforms depicted in the bottom part of the Figure 45 are characteristic for negative corona discharge in distilled water. The current waveform shows significantly higher level of noise in comparison with the current of positive discharges, which is in agreement with results of the Experimental part 1.
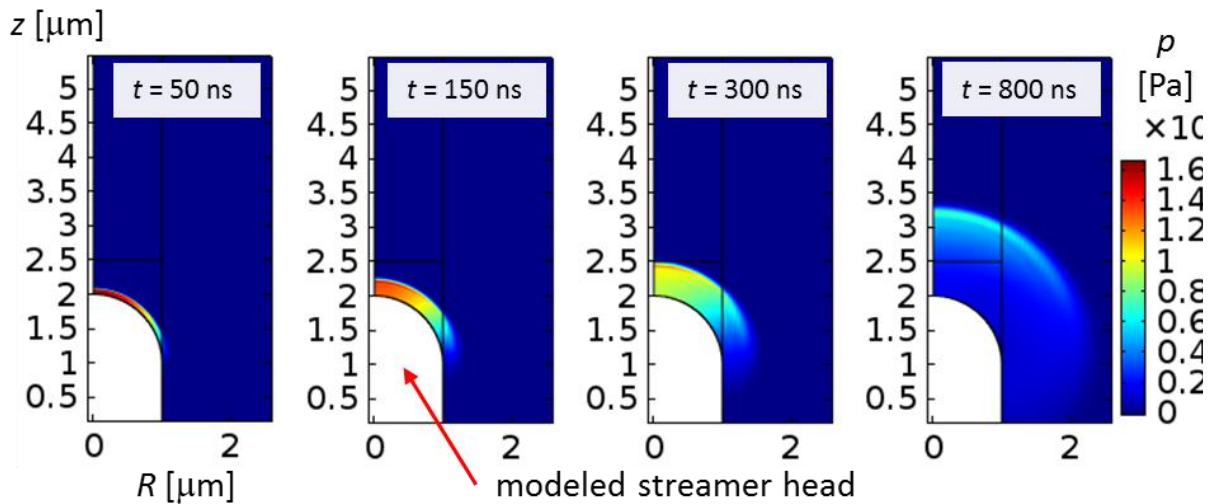
Figure 46 Simulation of transient shockwave produced by sudden acceleration of the liquid to the speed of 105 m·s^{-1} against a rigid tip. The geometry was modeled in cylindrical coordinates (z - axis of symmetry, R – radial distance); simulation was performed in Comsol Multiphysics software. The black lines ahead of the rigid tip are domain boundaries used to define mesh element size for the simulation only.

Experiments with salt water - positive needle electrode

Experiments with discharges in salt water were conducted with four different conductivities: 0.4, 0.8, 1.8, and 3.8 S·m^{-1}. The resistor R in the scheme in the Figure 40 had to be lowered to 200 Ω to reduce voltage loses on it. The capacity of the high voltage capacitor C was 10 nF, and it was charged to 23 kV. Cross section of the cuvette used in these experiments had dimensions 10×30 mm, where the larger one was that along which the laser beam propagated. The first reason for this change was that the glass windows could be damaged by heat from discharges, or by generated shockwaves, at high proximity between corona discharge and glass surface. Secondly, next experiments with composite electrode instead of the needle electrode required cuvette with larger opening. The gap size was set to 9 mm, and radius of the needle electrode was approximately 30 μm.

The experimental results of discharges at positive needle electrode in salt water solution with conductivity of 0.4 S·m^{-1} are shown in the Figure 47. The distance between the needle anode and the plate cathode was
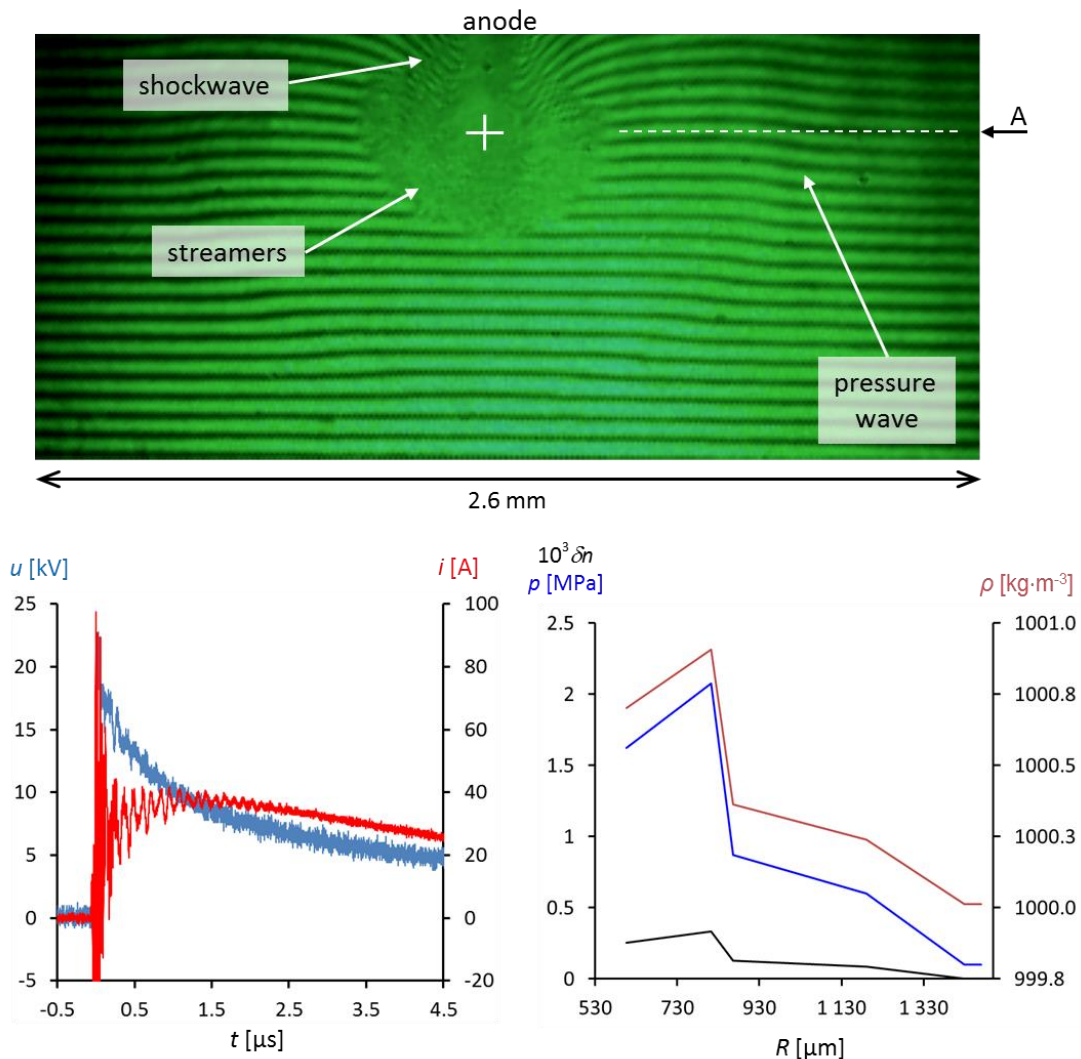
Figure 47 Interferogram of surroundings of streamers on a needle anode (top) in salt water solution with conductivity of 0.4 S·m^{-1}; radial profiles of the refractive index changes, of the liquid density, and of pressure at position A along fringes are added as functions of R (radial distance from the center of curvature marked by the cross) (bottom right); V-A temporal waveforms (bottom left).

9 mm. The interferogram at the upper part of the Figure 47 shows opaque area filled with many streamers, the ends of which can be recognized on the area boundary. Although the fringes are visible also in some places of the disturbed area, the interference field is too broken for any numerical analysis. The discontinuity of fringes just above the opaque area points to existence of spherical shockwave, the origin of which is not clear. The radius of opaque area is approximately two times larger than that of the shockwave. If it was created by superposition of many shockwaves generated by each streamer, it would mean that the streamers propagated approximately two times faster, i.e. ~3 km·s^{-1}. Although it could be possible due to presence of strong electric field, as it has been shown in the case of primary streamers in distilled water (Figure 42), one shot was insufficient for drawing any conclusions. Another weak spherical pressure wave with peak pressure of 20 MPa and radius of 0.86 mm can be recognized in the interference field (center of curvature is depicted by the white cross in the interferogram). Radial profiles of the refractive index deviations, density, and pressure at position A of the interferogram are depicted in the bottom right of the Figure 47. This pressure wave could be produced by water Joule heating, which caused significant fringe shift visible around the needle anode.

anode

3.14 mm
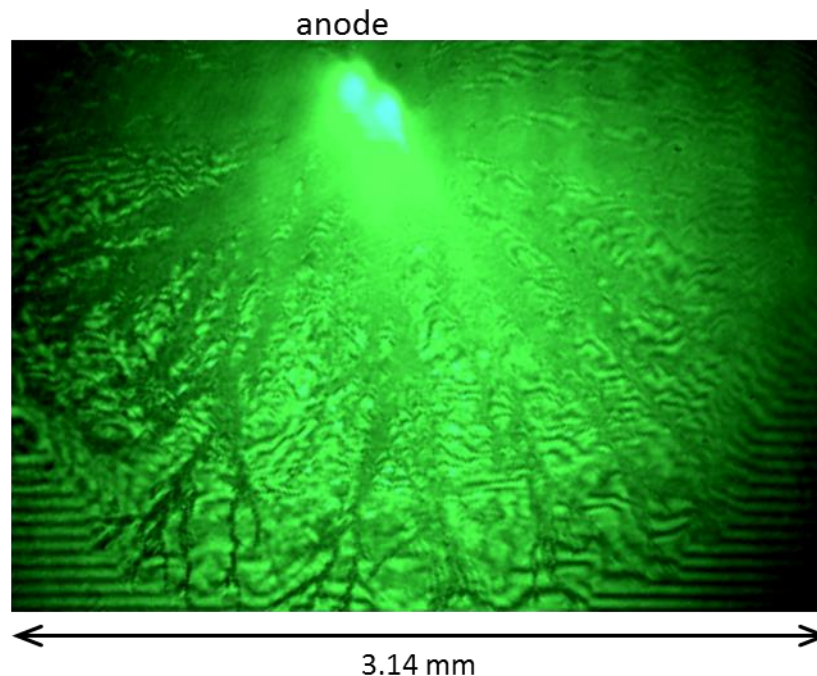
Figure 48 Interferogram of later stage of discharge in salt water solution with conductivity of 0.4 S·m^{-1}.

Interferogram of the later stage of the discharge is shown in the Figure 48, where individual streamers can be recognized. Superposition of shockwaves generated by each streamer created a complex pressure field in the area among the streamers, which totally destroyed the interference field.

The current waveforms plotted in the bottom left of the Figure 47 shows noticeable oscillations next to the known pre-breakdown noise. The oscillation period corresponds to the oscillation period of the driving circuit, the leakage inductance of which was of the order of ~1 μH, and parasitic capacitance 50 pF. In the previous experiments these oscillations could not appear due to high total circuit resistance, which perfectly damped any oscillations. Noticeable is also a relatively (in comparison to the voltage waveform) slow rise time of the current mean value, approximately 1.2 μs.

Similar results were obtained in experiments with salt water solution with conductivity of 0.8 S·m^{-1}. Interferogram of the discharge surroundings is depicted on the left of the Figure 49. As in the previous experiment, a lot of streamers created spherical opaque area. In contrast to the interferogram in the Figure 47, individual streamers can be recognized in the area. Fringes in the region adjacent to the needle anode are considerably compressed; that indicates strong changes of liquid density. Although the fringes can be clearly recognized, they are discontinuous at the area-boundary and other places. Therefore, no evaluation of refractive index could have been done.
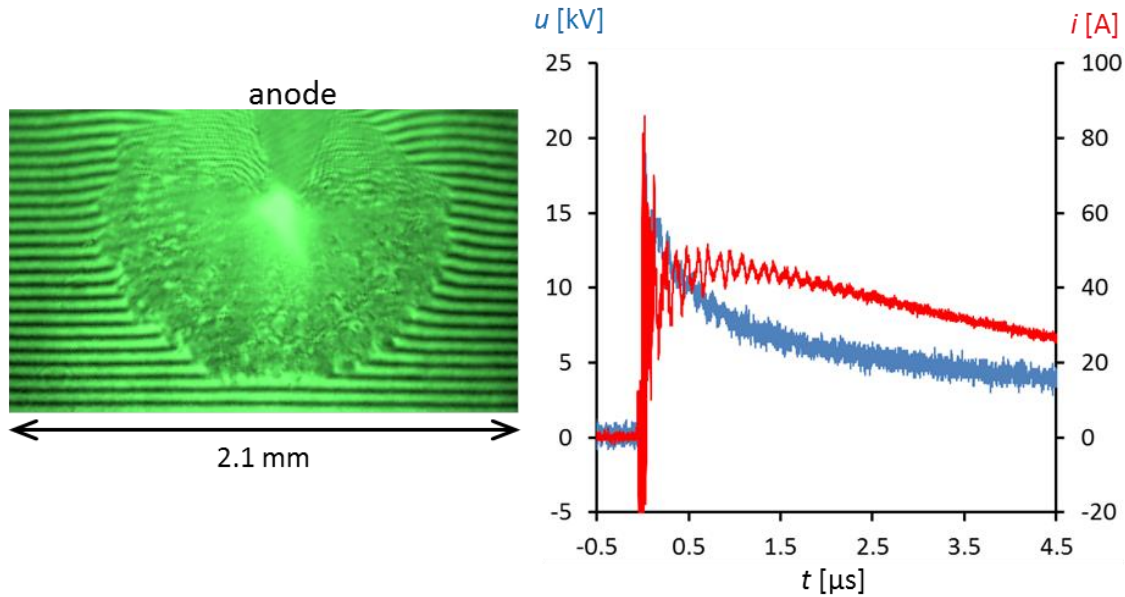
Figure 49 Interferogram of surroundings of streamers growing from a needle anode (left) in salt water solution with conductivity of 0.8 S·m^{-1}; typical V-A temporal waveforms (right).

After increasing solution conductivity to 1.8 S·m^{-1}, number of streamers decreased, and fringes around them can be used to evaluate radial profile of liquid refractive index. The analyzed interferogram is depicted in the left part of the Figure 50. Although there were many long, accidentally distributed streamers, a nearly spherical pressure wave was produced, which can be clearly recognized in the interferogram. Nevertheless, several streamers overtook the spherical wave, and created protrusions on its surface. It is possible that the pressure wave had been created by a primal expanding cavity just before the streamers emerged. Radial profiles of refractive index deviations, water density, and pressure at position A along fringes are depicted in the right part of the Figure 50. The peak pressure reached 18 MPa and was nearly constant along the analyzed interval of radii. The thickness of the pressure transitional region was too large for a shockwave: ~200 μm. Therefore, the interferogram was obviously captured before complete shock formation.

The dark layer on the bottom part of the pressure wave boundary, where no fringes can be seen, represents an area where the laser beam was partly reflected due to large gradient of refractive index and a large angle of incidence to this gradient. This means, that the pressure gradient in this place was larger than that in the position A, where the refractive index has been analyzed. Since the interference field at the bottom part of the pressure wave was destroyed due to high proximity of streamers, no numerical analysis of refractive index could be done in this area.

The current temporal waveform in the bottom right of the Figure 50 shows only low rise of the current amplitude in comparison with the previous experiment. It was caused by an increased voltage loss across the resistor R.

Next growth of the solution conductivity up to 3.8 S·m^{-1} led to small changes in the pressure profile, but significant changes in the discharge pattern, as is shown on the left in the Figure 51. Since streamers nearly disappeared, and only bumpy expanding cavity with signs of streamers left, perfect spherical pressure wave with smooth boundary was produced.

Interesting are both similar pressure profiles on the right of the Figure 51 and Figure 50. Comparison of the current curve in the current and previous experiment (bottom right of the Figure 51) indicates that current nearly does not change when varying conductivity in this range (due to voltage losses across R).
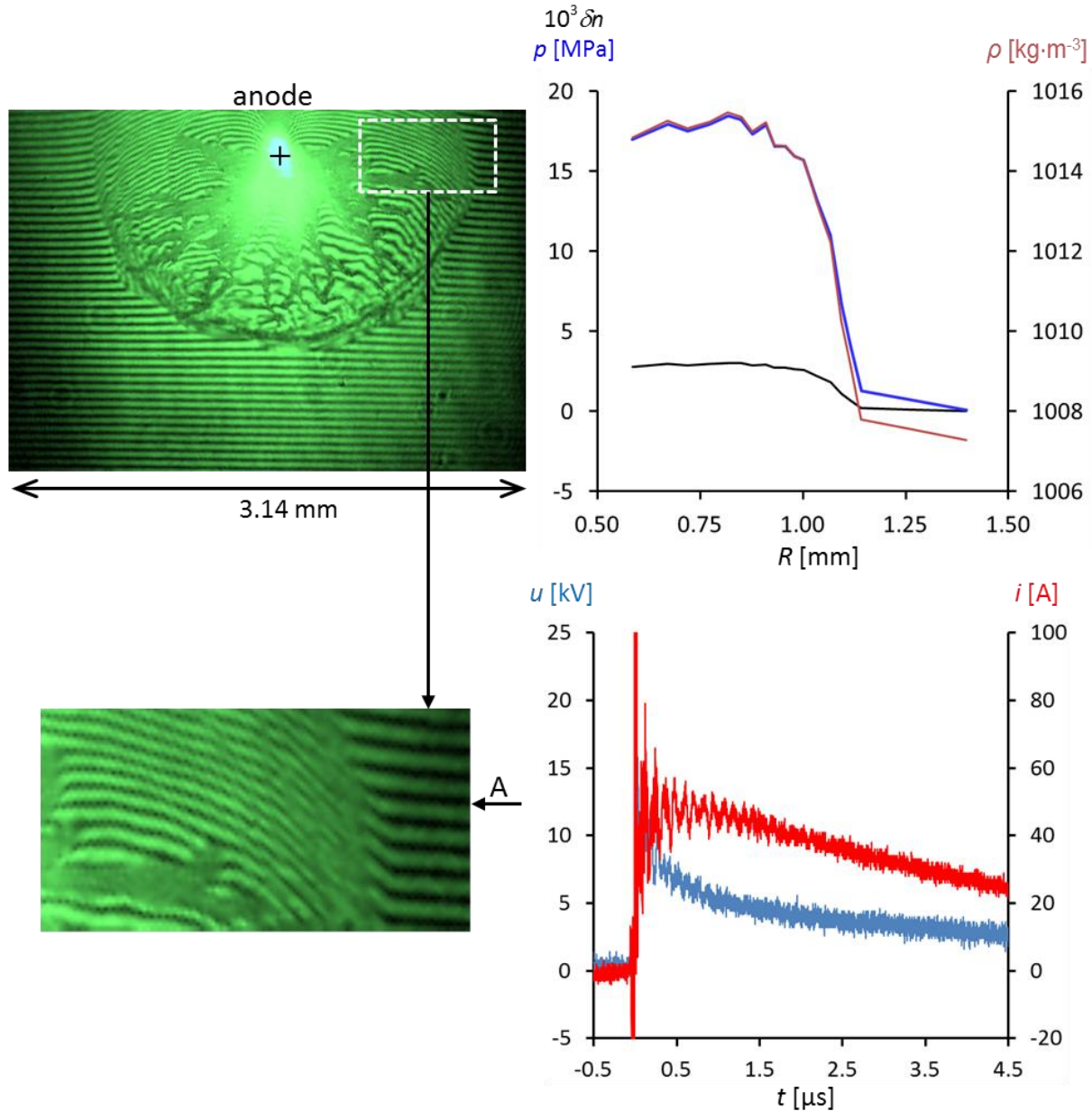
Figure 50 Interferogram of the surroundings of positive corona-like discharges (left) in salt water solution with conductivity of 1.8 S·m^{-1}, with detail of the analyzed area. Radial profiles of refractive index deviations, water density, and pressure at position A along fringes are plotted as functions of R (radial distance from the center of curvature marked by the cross) (top right), and typical V-A temporal waveforms of positive discharge at given solution conductivity (bottom right).

Assuming that expansion of the discharge cavity was driven by heating process due to resistive losses in the cavity, then the resistivity of plasma in both cases had to be similar to produce similar pressure profile, and was independent on the solution conductivity in this range.
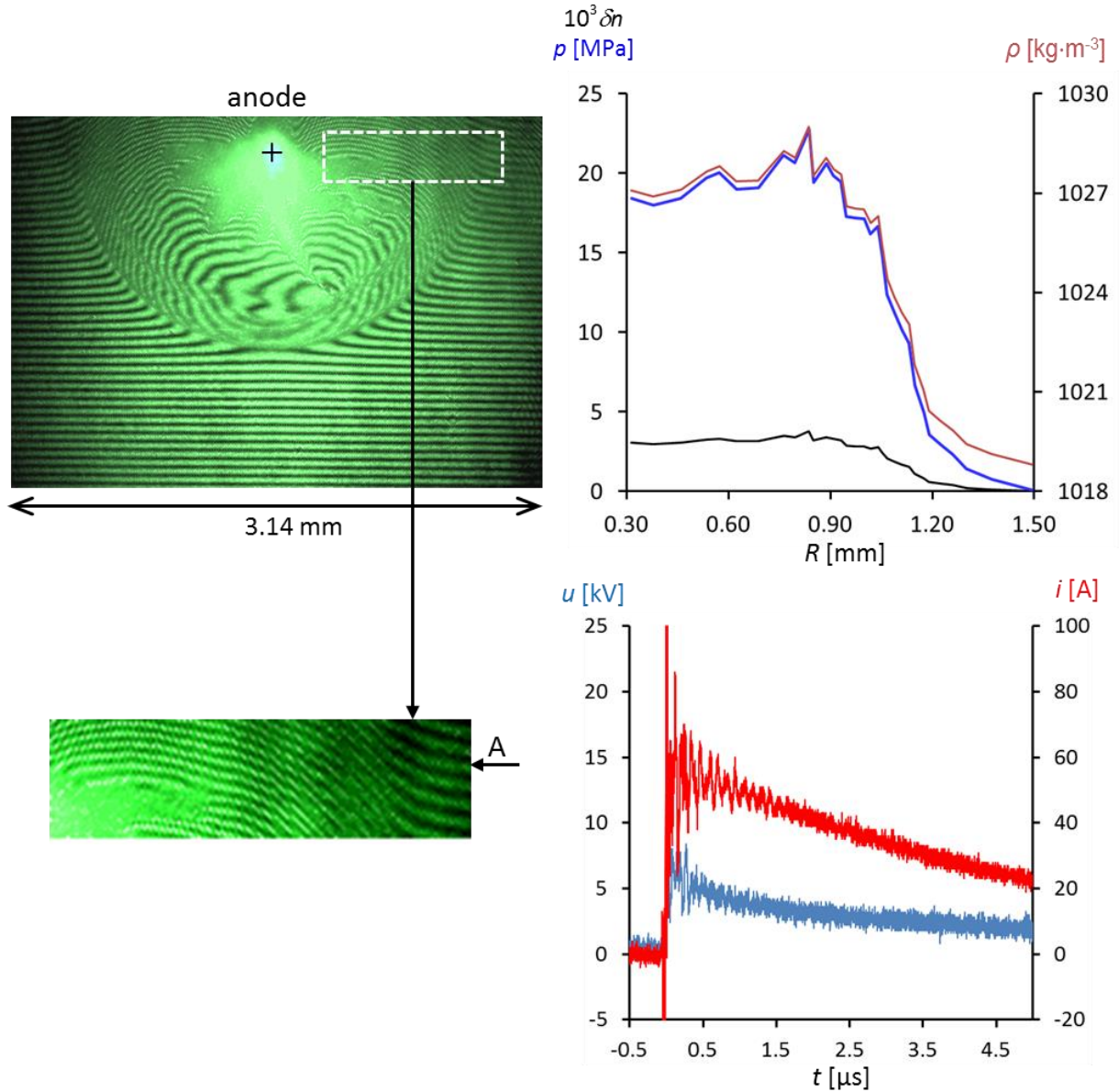
Figure 51 Interferogram of the surroundings of positive corona-like discharges (left) in salt water solution with conductivity of 3.8 S·m⁻¹. Radial profiles of refractive index deviations, water density, and pressure at position A along fringes are plotted as functions of R (radial distance from the center of curvature marked by the cross) (top right), and typical V-A temporal waveforms of positive discharge at given solution conductivity (bottom right).

Experiments with salt water - negative needle electrode

Experiments with negative needle electrode were conducted under the same conditions as the experiments with positive electrode. The discharges did not evince any streamers at solution conductivities $(0.4 - 3.8 \text{ S·m}^{-1})$; approximately spherical expanding cavities were formed only. Therefore, spherical pressure waves with smooth boundary were produced at every experiment. The experimental results are successively depicted in the Figure 52 − Figure 55. Although radial distribution of refractive index could be analyzed in all cases due to non-existence of streamers, near the cavities surfaces it was not possible to translate it into liquid density, because increased liquid temperature also influenced liquid refractive index. Amplitudes of measured current temporal waveforms are lower at 0.4 and 0.8 S·m^{-1} than that acquired in experiments with positive needle electrode. This can be explained by smaller surface of the

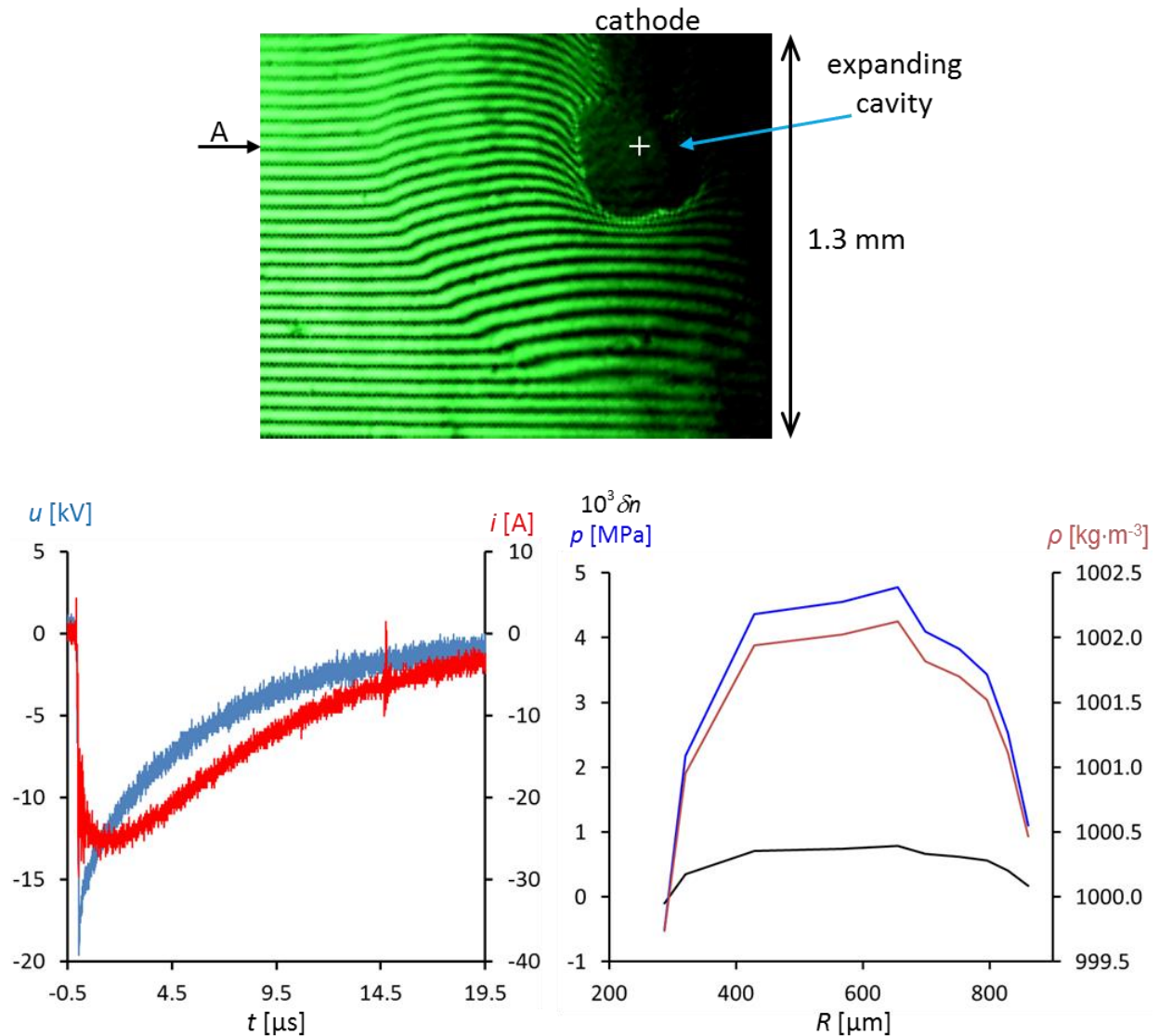

Figure 52 Interferogram of the surroundings of positive corona-like discharges (top) in salt water solution with conductivity of 0.4 S·m^{-1}. Radial profiles of refractive index deviations, water density, and pressure at position A along fringes are plotted as functions of R (radial distance from the center of curvature marked by the cross) (bottom right), and typical V-A temporal waveforms of negative discharge at given solution conductivity (bottom left).

discharge cavity in solutions with small conductivities. Dependence of peak pressure on current was insignificant at solution conductivities of 0.4 and 0.8 S·m^{-1} (Figure 52 – Figure 53). While the current amplitude was higher at 0.8 S·m^{-1}, the peak pressure was even lower. Seemingly considerable increase of peak pressure was detected, when conductivity had been increased to 1.8 S·m^{-1}, as it is depicted in the Figure 54. Nevertheless, radius of the pressure wave captured in the Figure 54 (at position B) was approximately half of that in the Figure 52 – Figure 53. According to acoustic approach, where wave pressure is inversely proportional to radial distance from the origin, the peak pressure of the wave with radius 0.5 mm and amplitude 9 MPa at position B in the Figure 54 falls to 4.5 MPa, when its radius increases to 1 mm. It is nearly two times larger value than that, which can be found in the pressure profile in the Figure 53 at the same radius. However, pressure profile in position A in the Figure 54 shows that it
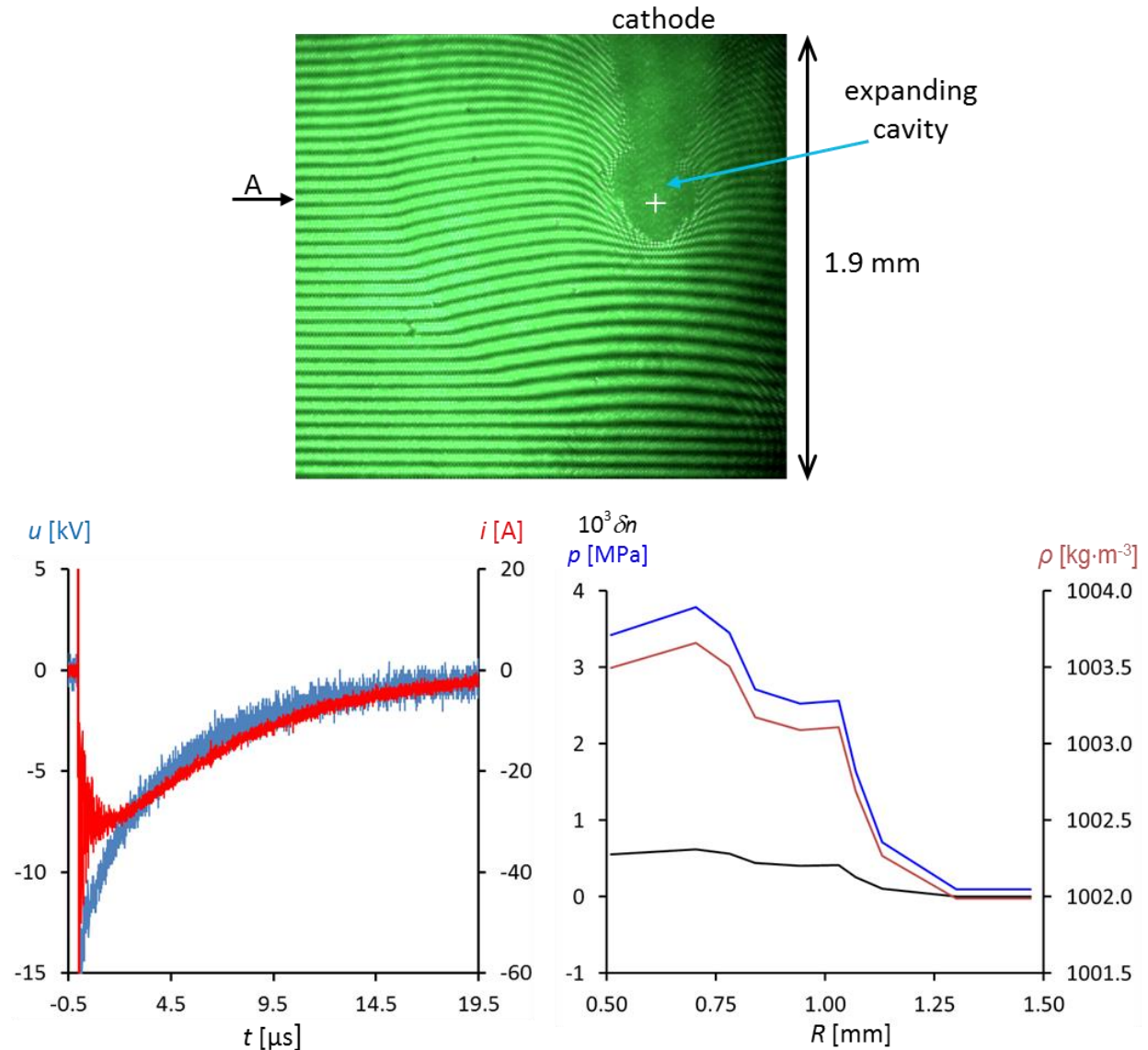
Figure 53 Interferogram of the surroundings of positive corona-like discharges (left) in salt water solution with conductivity of 0.8 S·m^{-1}. Radial profiles of refractive index deviations, water density, and pressure at position A along fringes are plotted as functions of R (radial distance from the center of curvature marked by the cross)(bottom right), and typical V-A temporal waveforms of negative discharge at given solution conductivity (bottom left).
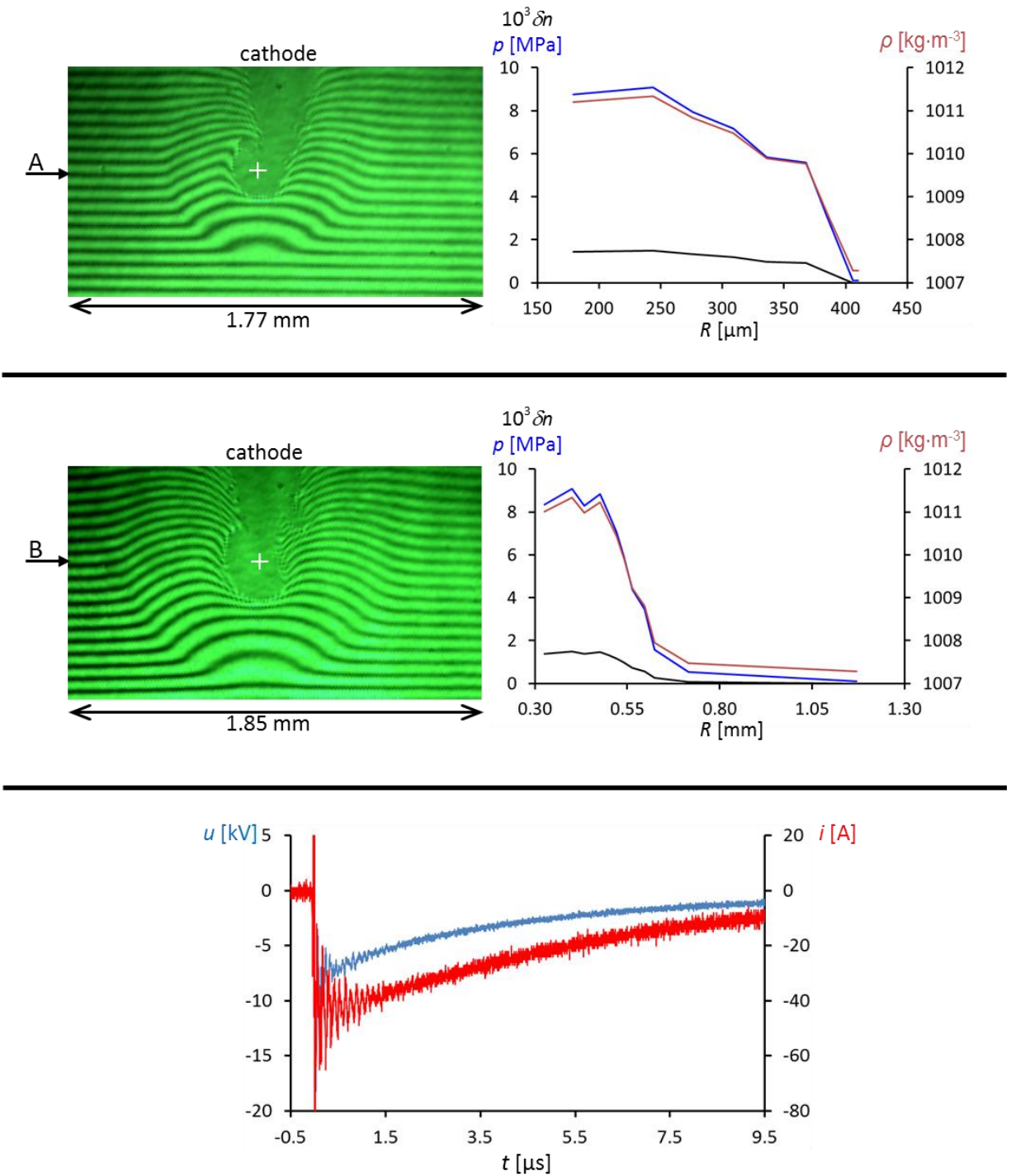
Figure 54 Interferogram of the surroundings of negative corona-like discharges (left) in salt water solution with conductivity of 1.8 S·m⁻¹. Radial profiles of refractive index deviations, water density, and pressure at positions A and B along fringes as functions of R (radial distance from the center of curvature marked by the crosses) are depicted on the right of each interferogram; typical V-A temporal waveforms of nagtive discharge at given solution conductivity (bottom).

Figure 55 Interferogram of the surroundings of negative corona-like discharges (left) in salt water solution with conductivity of 3.8 S·m^{-1}. Radial profiles of refractive index deviations, water density, and pressure at position A along fringes are plotted as functions of R (radial distance from the center of curvature marked by the cross) (bottom right), and typical V-A temporal waveforms of negative discharge at given solution conductivity (bottom left).
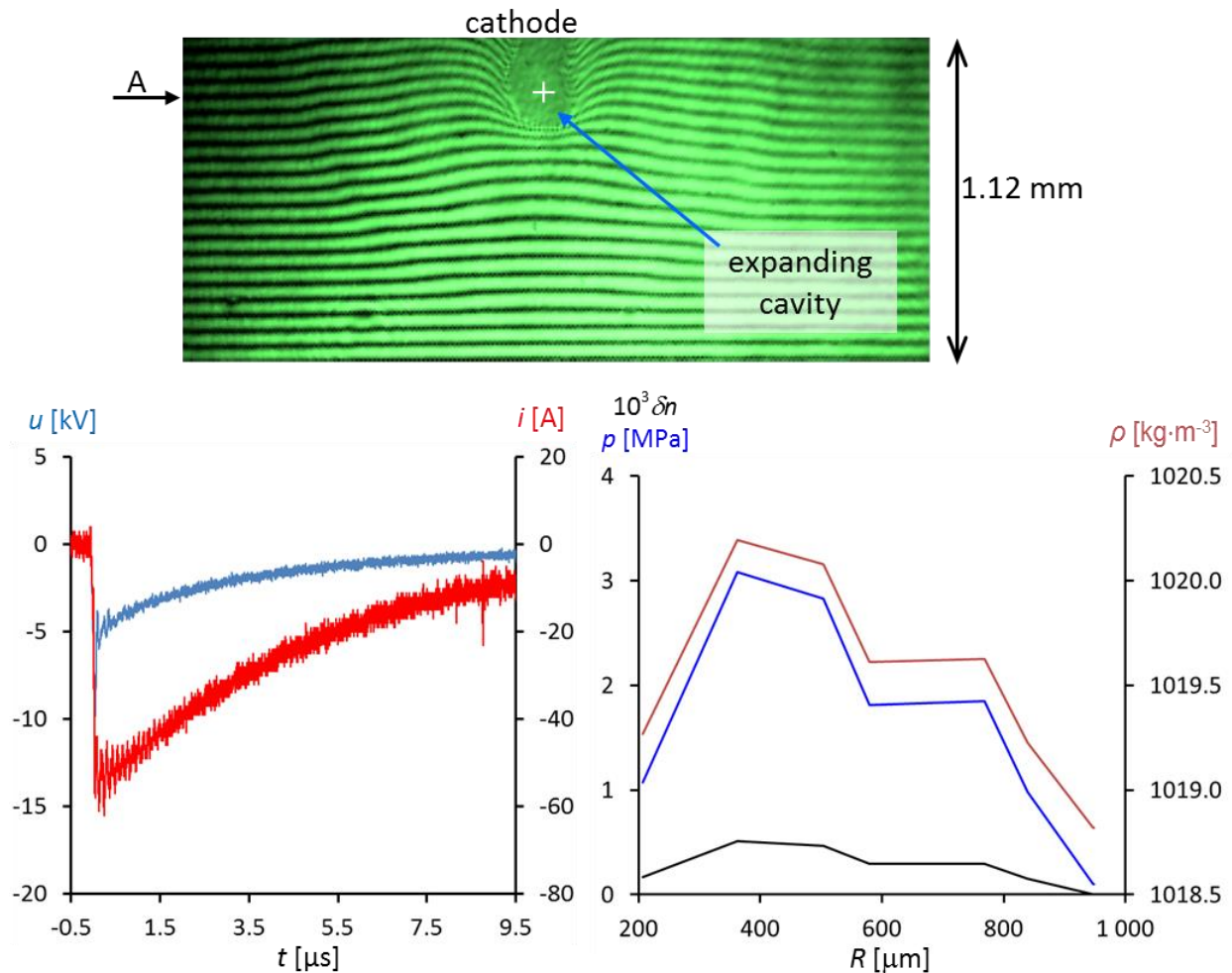
is not a rule, probably because the discharge is ignited every time in initial cavity with different diameter and at different voltage.

The final increase of the solution conductivity up to 3.8 S·m^{-1} led to significant decrease of pressure level, although current amplitude increased, as it is shown in plots in the Figure 55. If the expansion of the discharge cavity is driven by heating process due to resistive losses in the cavity; the plasma resistivity should be significantly different at solution conductivity of 3.8 S·m^{-1} than that at 1.8 S·m^{-1} to produce lower peak pressure, because the current waveforms differ negligibly at these conductivities.

Pressure waves generated by discharges with negative needle electrode have generally lower peak pressure than the pressure waves from discharges with positive needle electrode. It is not surprising with respect to differences in evaporation rates observed in the experiments with discharges in glass capillaries in the Experimental part 1, where evaporation of conductive salt solution working as the liquid cathode was significantly more intense than evaporation from the liquid anode.

Plasma conductivity

Information obtained from the Figure 54 was used for estimation of plasma conductivity inside the expanding nearly spherical cavity (the discharge channel). From the interferogram next to the pressure profile at the position A, also the cavity radius can be determined – being 108 μm. Numerical simulation (in spherical coordinates) of flow with high Mach number was used for finding such time dependent radial velocity of the cavity wall that produces pressure profile similar to the measured one. The simulation used the Tait's equation (4.23) at constant temperature as liquid equation of state. More information about the used computational fluid dynamics module can be found in [68].
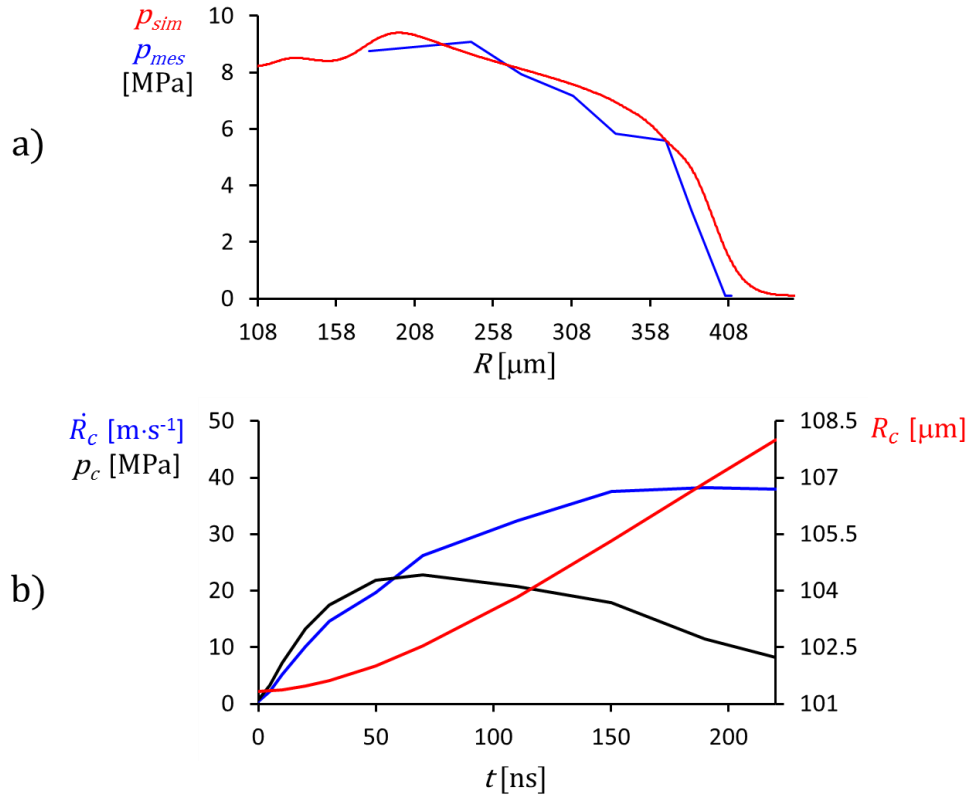
Figure 56 a) comparison of the measured p_{mes} and the calculated p_{sim} pressure profiles in $t = 220$ ns; **b)** temporal waveforms of the calculated parameters of the expanding cavity: pressure on the cavity surface p_c, the cavity radius R_c, and rate of the cavity expansion $\dot{R}_c$.

The calculated p_{sim} and the measured p_{mes} pressure profiles are depicted in the Figure 56a for comparison. The missing part of the measured pressure profile at the interval 108 μm $\leq R \leq$ 179 μm was extrapolated along the tangential line in the last point of the measured pressure curve. The appropriate temporal waveform of the cavity expansion rate $\dot{R}_c$ that produces the calculated pressure profile p_{sim}, is shown in the Figure 56b, where waveforms of cavity radius R_c as well as pressure on the cavity surface p_c, are also displayed. Zero time in this graph corresponds to the beginning of emission of the pressure wave. The Figure 56 says that the cavity radius changes only little, and that this movement does not generate a pressure wave until the cavity radius reaches 101.3 μm. Since no significant disturbance in the interferogram at radii larger than 406 μm were detected (Figure 56a), the cavity had to expand slowly until reaching radius of 101.3 μm. This fact provides another explanation for absence of a significant

67

pressure wave in the interferogram in the Figure 55: the phase of rapid cavity expansion producing the pressure wave had not yet come, when the interferogram in the Figure 55 was captured.

Plasma conductivity in the cavity is determined by the power loss in the cavity, which can be obtained from equation for the internal energy of gas inside the cavity (the first law of thermodynamics)

$$de = \delta Q + \delta W \qquad (4.43)$$

where de, δQ, and δW are by turns infinitesimal change of the cavity internal energy, infinitesimal heat deposited/dissipated in the cavity, and infinitesimal work absorbed by the cavity (if work is done by the cavity, the sign is negative). This equation can be rewritten into a form [69]

$$\frac{1}{\gamma-1}\frac{d(p_c V_c)}{dt} = P_J - p_c\frac{dV_c}{dt} \qquad (4.44)$$

where γ is the ratio of specific heats of gas inside the cavity, p_c [Pa] is pressure on the cavity wall (which is supposed to be approximately the same as the gas pressure inside the cavity, since contribution of water surface tension at radii of the order of ~100 μm is negligible), V_c [m^3] is the cavity volume, t [s] is time, and P_J [W] is the total power loss due to Joule heating

$$P_J = \int_{V_c} \frac{j^2}{\sigma_{pl}} dV \qquad (4.45)$$

where j [A·m^{-2}] is plasma current density in the cavity, and σ_{pl} [S·m^{-1}] is plasma conductivity. However, at once is to be said that this direct recipe for direct P_J calculation cannot be used, because of missing synchronization of camera (registering interferograms, therefore, pressure fields) with oscilloscope (registering the discharge current). Moreover, the equation (4.43) and (4.44) are valid only when there is no mass transfer between the cavity and its surroundings, and when it is possible to neglect heat conductivities and radiative losses. This is, unfortunately, only partly true.

It is assumed that water vapor creates a dominant part of the cavity content. Since the dissociation energy of water molecule is 5.13 eV [70], at temperatures of the order of ~1000 K (see Chapter 3) the degree of dissociation is small. The more also the degree of ionization is very small. Therefore, the ratio of specific heats γ used for the calculation of the power loss can be chosen to be equal to the ratio of specific heats of water vapor ($\gamma = 1.33$). Then the temporal waveform of the total power loss P_J can be calculated from the
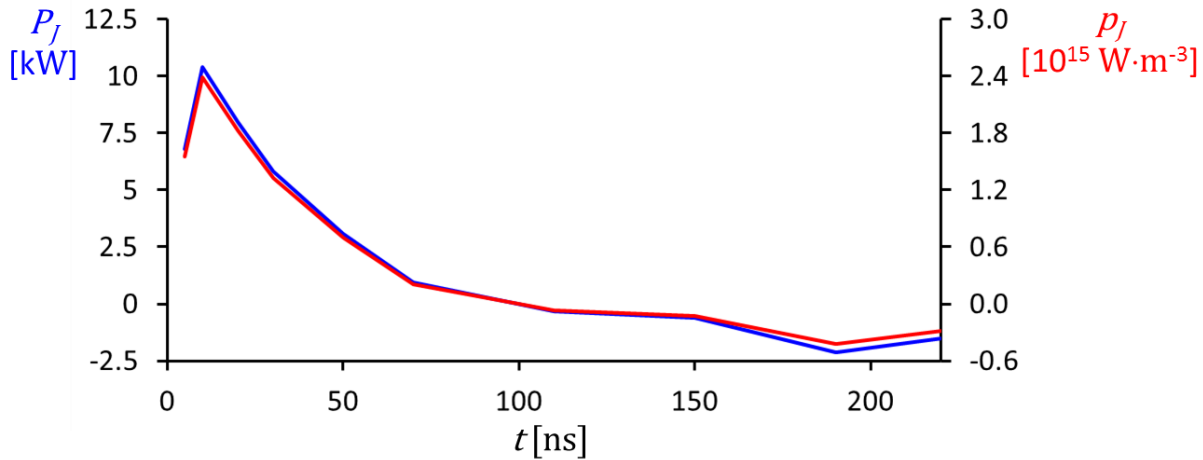
Figure 57 Temporal waveforms of the total power loss P_J and the average power loss density p_J due to Joule heating of plasma inside the expanding cavity.

equation (4.44) and also the average power loss density $p_J = P_J/V_c$ can be inferred. Both these waveforms are shown in the Figure 57. Later parts of these waveforms (110 ns from the beginning of emission of the pressure wave) over-swing to negative values, because loss of gas internal energy in the cavity is larger than the mechanical work done by expanding cavity. It does not mean that the internal energy was recuperated. The internal energy could be transferred to the surrounding water volume mainly by condensation of water vapor on the cavity wall, and also by heat conductivity. An incorrect extrapolation of the missing part of the pressure waveform near the cavity surface in the Figure 56a could be also responsible for the negative values in the power loss waveforms. Therefore, the maximum power losses in the cavity exceeded the peak values in the Figure 57, i.e. $P_J > 10.4$ kW, $p_J > 2.4 \cdot 10^{15}$ W·m^{-3} at 10 ns. The estimation of plasma conductivity requires numerical simulation of power loss density in needle-cavity geometry at different plasma conductivities. The electrode current used for simulation could not have the maximum measured value of ~60 A (at the time, when the cavity had radius >101 μm), because in the beginning the cavity was expanding slowly, and thus it took some time to grow up to 101 μm. Current lower that 10 A was also improbable, since it was found that at the electrode current of 10 A it was possible to achieve the power loss density p_J to be of the order of 10^{15} W·m^{-3} (the wanted power loss density) only with plasma conductivity $\sigma_{PL} = \sigma_L$ (liquid conductivity) = 1.8 S·m^{-1}. It is the maximum power loss density at the given electrode current; it is not achievable at lower electrode currents. Distribution of the power loss density in and around of the cavity at such conditions is shown in the Figure 58.

In conclusion, plasma conductivity inside the expanding cavity, which generated pressure field calculated from the distribution of refractive index at position A in the interferogram in the Figure 54, was estimated to be of the order of ~1 S·m^{-1} at 10 ns after it began generating the pressure wave.
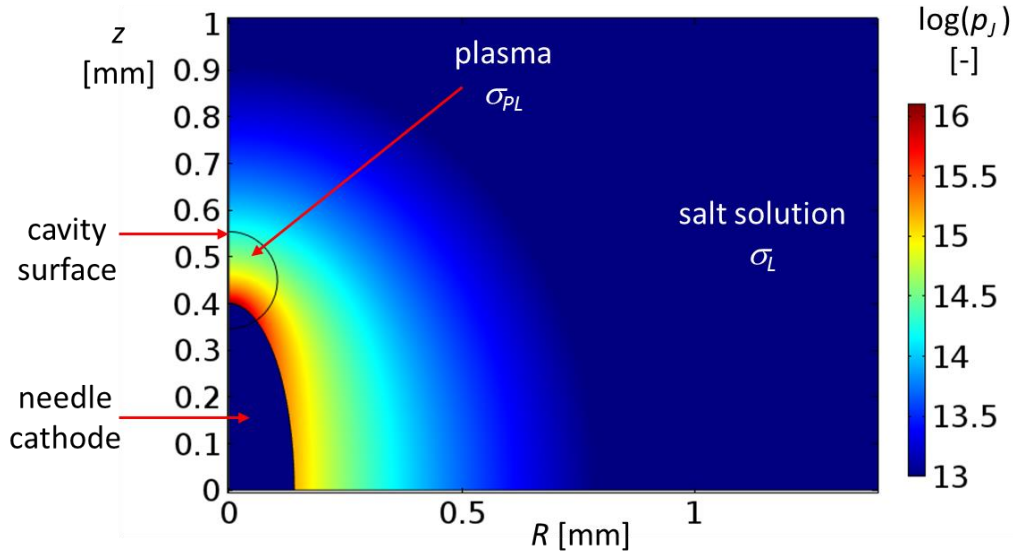
Figure 58 Distribution of maximum power loss density in and around the cavity connected with a needle electrode in conductive salt solution with conductivity $\sigma_L = 1.8$ S·m^{-1}. Plasma conductivity inside the cavity had to be $\sigma_{PL} = \sigma_L$ to achieve the wanted power loss densityof the order 10^{15} W·m^{-3} at the electrode current of 10 A. The simulation was performed at cylindrical coordinates (z – axis of symetry, R - radius) by Comsol Multiphysics software.

Composite electrodes

Experimental setup used in these experiments was the same as in the previous experiments with needle electrodes. Only the needle electrode was replaced by a ceramic coated electrode, hereafter called composite electrode. The composite electrode is made of stainless steel rod with diameter of 5.9 mm, which is covered by a thin (~0.4 mm) ceramic layer of almandine. Photograph of the composite electrode is shown in the Figure 59a. The ceramic layer works as porous insulation, where diameter of the pores is of the order of ~1 μm (Figure 59b). The number density of the pores is approximately ~1 mm^{-2}. When the composite electrode is immersed in a conductive liquid against another metal electrode and voltage is

a)   b)
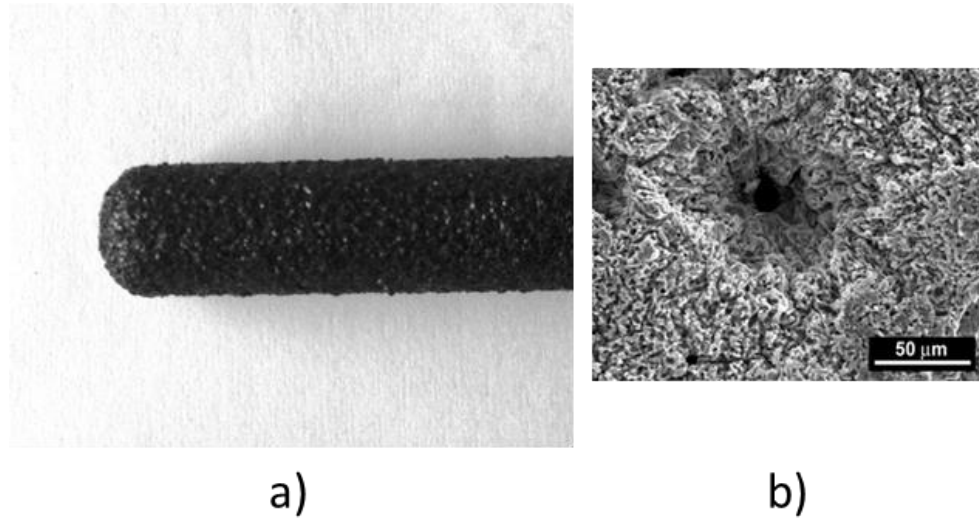
Figure 59 a) Photograph of stainless steel electrode covered by porous ceramic layer of almandine (composite electrode). Outer diameter is of 6.7 mm; **b)** photograph of a pore in the ceramic layer.

applied between them, almost all the potential distributes across the ceramic layer due to high ratio of pores/bulk liquid resistances. Simulation of distribution of electric field in and around of the pore in thin insulation is depicted in the Figure 60. The pore is located on the axis of the model (on the z axis), and is filled with a conductive liquid. As it can be seen in the right part of the Figure 60 the electric filed inside the insulator is of the order of 100 MV·m^{-1}, and it is by 5-7 orders lower outside the insulator. Detail of the pore in the left part of the Figure 60 shows that electric field in the pore is comparable to the electric field in the insulator; the tangential parts of electric field must equal on both sides of the pore boundary, if the temporal change of tangential magnetic field on the boundary is zero: $\partial B_{\parallel}/\partial t = 0$. The difference of electric fields inside and outside the pore in the Figure 60 is caused by presence of normal parts of electric field next to the tangential parts.

If the pore is filled with the conductive liquid (1.8 S·m^{-1} in this case), strong Joule heating σE^2 of the order of 10^{16} J·m^{-3} will result in fast liquid overheating followed by the electrothermal breakdown described in the Chapter 2.2.

If the pore is not filled with the liquid (e.g. when the surface of pore-boundary is hydrophobic), electric field in the pore will change slightly. Then the breakdown of gas in the pore occurs directly without preceding phase change of the liquid.

A corona-like discharge develops in the both cases. Consequent expansion of the plasma channels from the pores produces semi-spherical pressure waves. High number density of pores on the electrode surface leads to generation of many semi-spherical pressure waves, which, after their superposition, form one large-area pressure wave. Using of composite electrodes has some advantages. First, it can be used for generation of pressure waves with arbitrary geometry, since their shape is determined by the shape of the
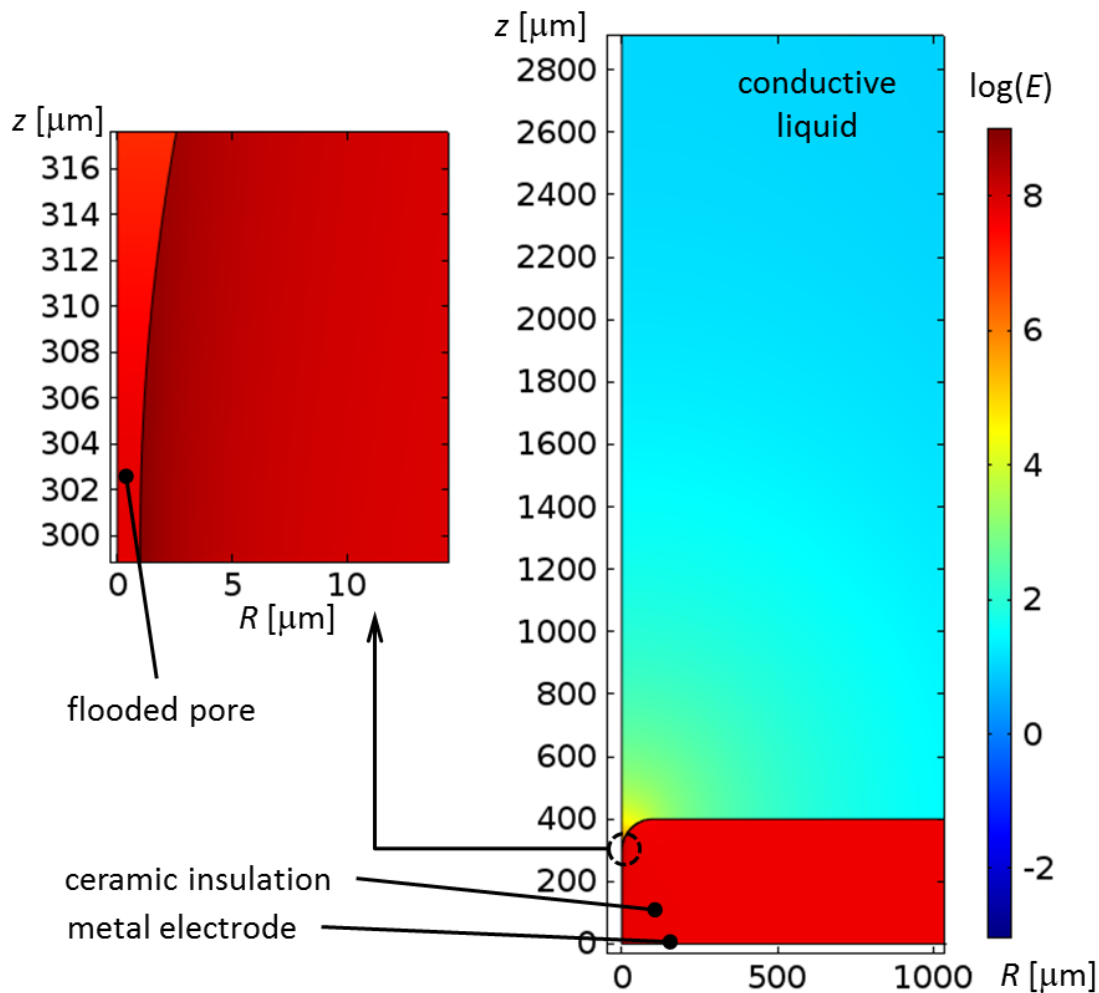
Figure 60 Simulation of distribution of electric field inside and in the vicinity of a tiny pore in ceramic insulation covering metal electrode immersed in conductive liquid. Conductivity of the insulation layer used for the simulation was 10^{-15} S·m^{-1}, and conductivity of the liquid was 1.8 S·m^{-1}. Height of the opposite electrode above the insulation surface was 10 mm, and voltage between the metal electrodes was of 20 kV. The geometry was modeled in cylindrical coordinates (z - axis of symmetry, R – radial distance); simulation was performed in Comsol Multiphysics software.

electrode surface. Second, generation of pressure waves by these electrodes is more efficient, because all the current can flow through the pores only, i.e. through the expanding corona discharges.

All the following described experiments were performed at solution conductivity of 1.8 S·m^{-1}. The reason is that the existing generator of focused shockwaves described in the Experimental part 3 uses salt water solution with just this conductivity 1.8 S·m^{-1}, at which plasma channels are short and dense (number of channels per cm^2 is high) enough for production of cylindrical pressure wave with symmetry axis identical with axis of coated cylindrical electrode.

Experiments with positive composite electrode

Results of experiments focused on analyses of pressure waves produced by corona-like discharges on ceramic coated anode are depicted in the Figure 61. The interferogram in the upper part of the Figure 61 shows early stage of semi-spherical pressure waves together with discharges, which produced them. The
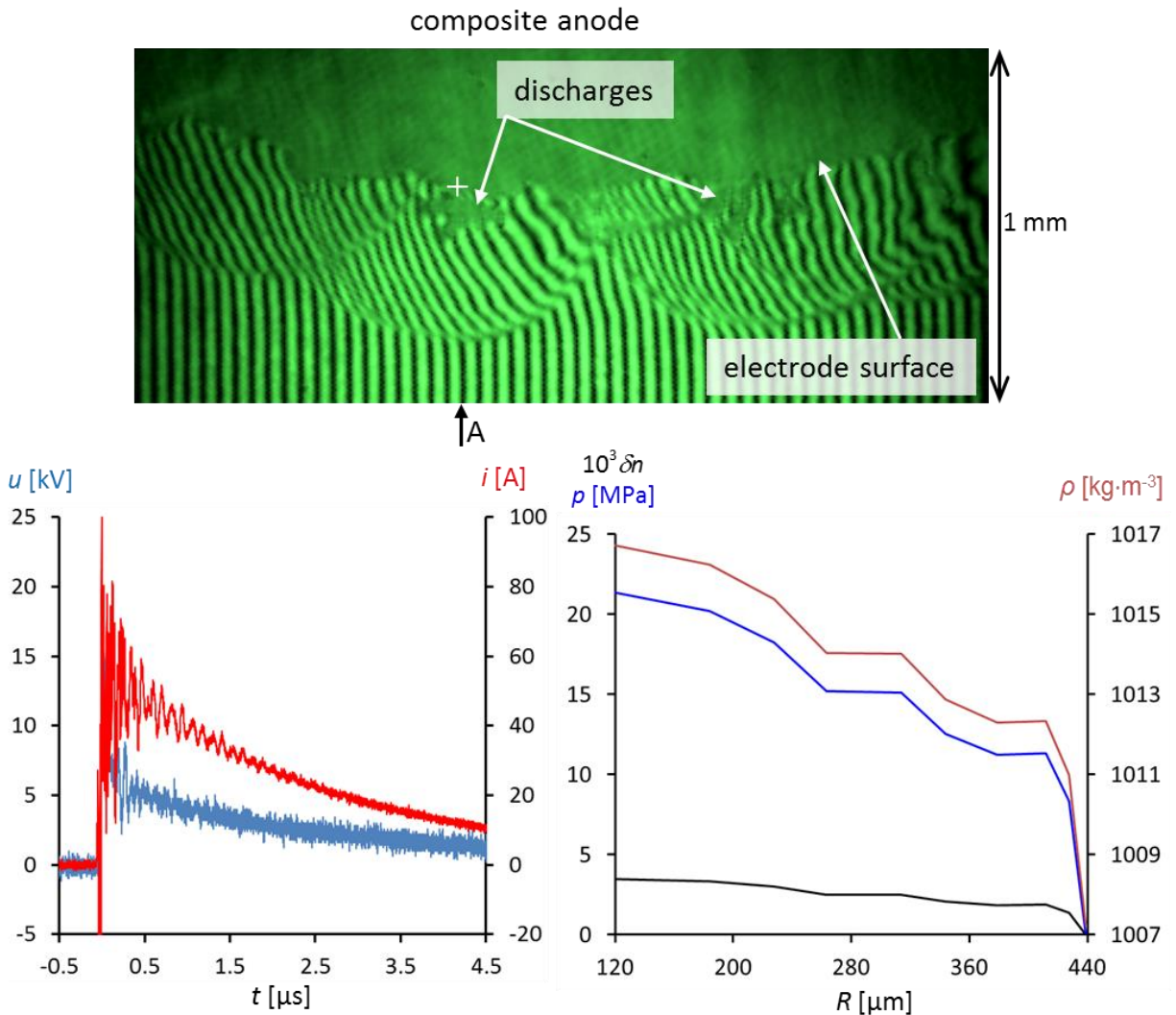
Figure 61 Interferogram of the surroundings of positive corona-like discharges (top) produced on composite anode in salt water solution with conductivity 1.8 S·m^{-1}. Radial profiles of refractive index deviations, water density, and pressure at position A along fringes are plotted as functions of R (radial distance from the center of curvature marked by the cross) (bottom right); typical V-A temporal waveforms of positive discharge at given solution conductivity (bottom left).

pressure waves seemingly physically overlapped, but they rather lay in different distances. Radial profiles of refractive index deviations, water density, and pressure at position A along fringes is depicted in the right part of the Figure 61. The radial pressure profile contains jump up to 8 MPa with thickness of the transition region of 12 μm. Behind this jump the pressure monotonically increases up to 21 MPa, which means that the pressure in the discharge channel was still increasing in the time, when the interferogram was captured.

Comparison of this pressure waveform with the waveforms measured around discharges on the needle anodes is problematic, because the total current is divided among many discharges, and produced pressure waves expand into half space only. The V-A temporal waveforms in the left part of the Figure 61 shows similar current waveform as in the Figure 50. Since the electrode active area (where corona-like discharges appeared) was around 100 mm^{-2}, the total current was divided among ~100 discharges. Therefore, current flowing through the discharges in the interferogram in the Figure 61 reached value of
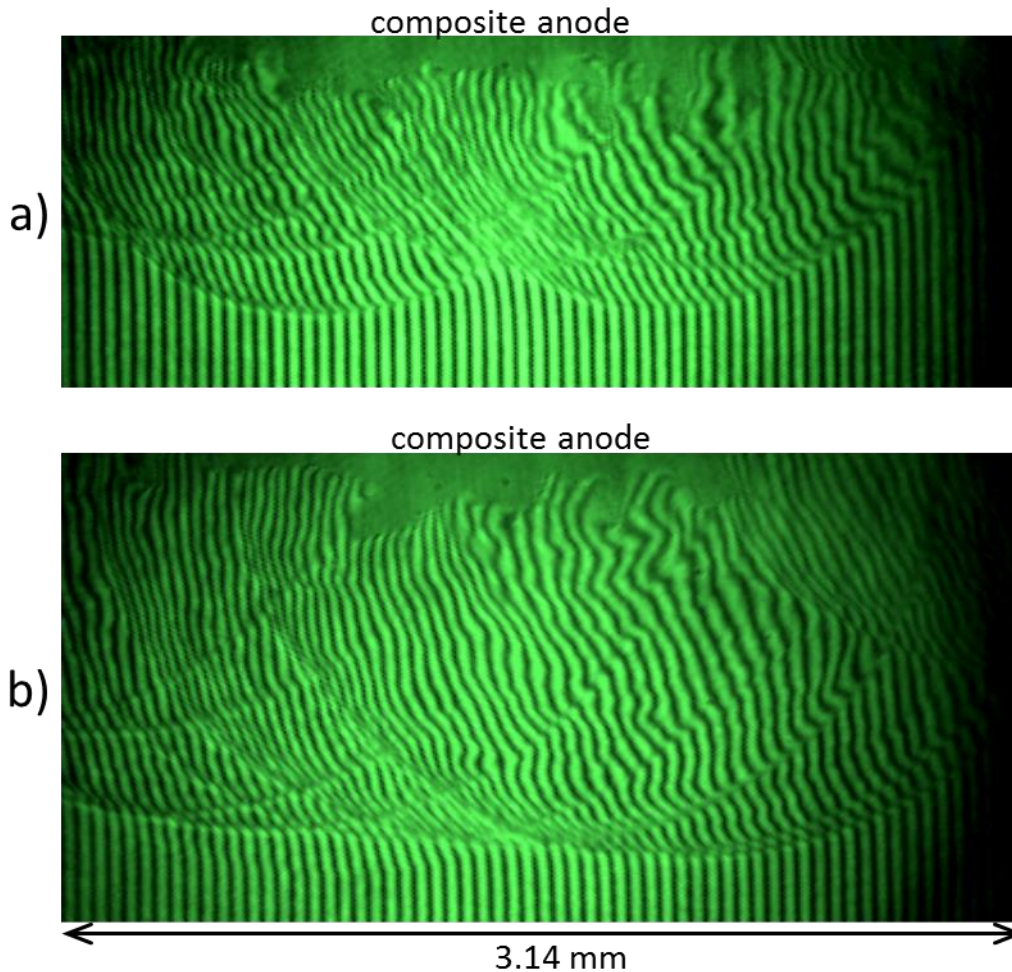
Figure 62 Interferograms of the surroundings of positive corona-like discharges produced on composite anode in salt water solution with conductivity 1.8 S·m^{-1}; **a)** discharges were initiated in different times, emitted pressure waves have different radii; **b)** discharges were initiated simultaneously, emitted pressure waves have the same radii, and their outer boundaries form a uniform envelope.

1 % of the total current flowing through the positive needle electrode, where only one discharge channel was produced. Since their pressure levels are comparable, it can be concluded that production of pressure waves by composite electrodes is much more efficient.

Equal radii of the pressure waves in the interferogram in the Figure 61 show that the pressure waves were produced in the same moment in this case. This synchronicity does not happen every time, as the Figure 62 illustrates. The Figure 62a shows semi-spherical pressure waves with different radii. Assuming that they expanded approximately with the same speed (~speed of sound), the generating discharges had to be initiated at different times. The Figure 62b shows the opposite situation, when the pressure waves have the same radii, and their outer boundaries form a uniform envelop. The discharges had to be initiated simultaneously in this case. As has been said, discharges can be initiated in gas filled pores as well as in flooded pores. The latter case requires an additional time for heating and evaporation of the liquid in pore to make breakdown possible. Since it takes some time to flood pores, when liquid has been blown out by discharge (time required for dissolving of gas in pores in the surrounding liquid), probably not all pores are flooded when next discharges are initiated. Thus, these gas-filled pores could be electrically broken down earlier than the others.

Experiments with negative composite electrode

Experiments with the negative composite electrode were performed under the same conditions as the experiments with the positive electrode. Results of experiments focused on analyses of pressure waves produced by corona-like discharges on composite cathode are depicted in the Figure 63. The

Figure 63 Interferogram of the surroundings of negative corona-like discharges (top) produced on composite cathode in salt water solution with conductivity 1.8 S·m⁻¹. Radial profiles of refractive index deviations, water density, and pressure at position A along fringes are plotted as functions of R (radial distance from the center of curvature marked by the cross) (bottom right); typical V-A temporal waveforms of negative discharge at given solution conductivity (bottom left).

interferogram in the upper part of the Figure 63 depicts an early stage of semi-spherical pressure waves. No discharges can be recognized in the interferogram.

Although the current waveform in the left bottom part of the Figure 63 is very similar to the waveform measured with the ceramic coated anode, the pressure profile shown in the right bottom part of the Figure 63 is different. It monotonically increases from its outer radius to inner one without any jump. It is also directly visible in the interferogram, that the pressure waves have no distinct boundaries. It is obvious that pressure waves generated by composite cathode are generally weaker than the waves generated by composite anode. A similar situation has been observed in the case of needle electrodes.

Initiation of discharges on negative composite electrodes is not simultaneous, as shows the interferogram in the Figure 64, where non-uniformly distributed pressure waves can be recognized.
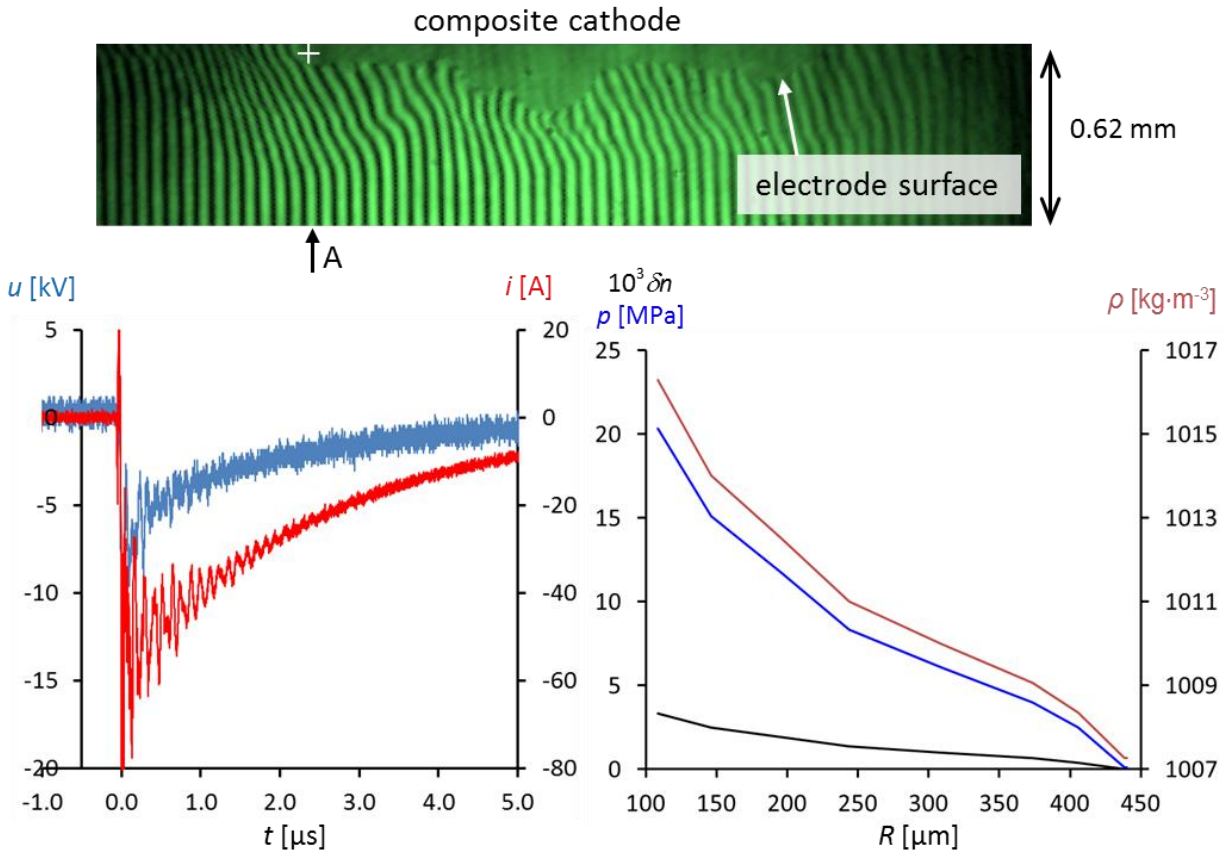
composite cathode

3.14 mm
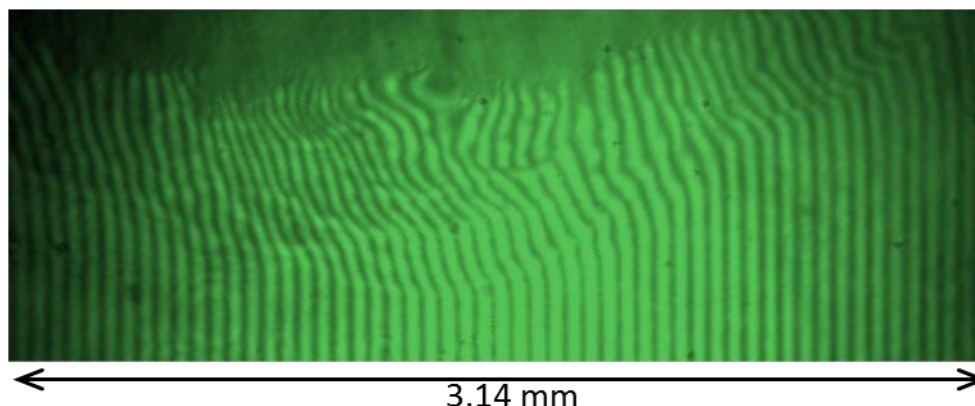
Figure 64 Interferogram of the surroundings of negative corona-like discharges produced on composite cathode in salt water solution with conductivity 1.8 S·m^{-1}. The shift of fringes makes the non-uniformly distributed pressure waves visible.

Conclusions of the experimental part 2

Experiments with corona-like discharges on needle and composite electrodes in aqueous salt solutions with different conductivities have been done. The experiments were aimed at interferometry analysis of pressure field generated by the corona-like discharges. It has been found that pressure waves generated by positive coronas reach generally higher pressure levels.

Spherical shockwave with radius 100 μm, thickness of transition region less than 2.73 μm, and pressure 33 MPa was detected only in the case of primary discharge in distilled water. High volume number density of positive streamers at conductivities 0.4 and 0.8 S·m^{-1} did not allow to recognize fringes in the captured interferograms. Spherical pressure waves with radius ~1 mm, thickness of transition region ~200 μm, and pressure 18-20 MPa were detected at conductivities 1.8 and 3.8 S·m^{-1}. Since the discharge currents at these conductivities were comparable, similarly as the generated pressure levels, it has been found that the plasma conductivity of the discharges had to be similar, and independent on conductivity of the salt solutions. Streamers receded at the highest conductivity, and the pressure waves were generated rather by expanding bumpy cavity with only signs of streamers.

Maximum amplitude of pressure waves formed on tip of negative streamers in distilled water reaches 20 MPa. The pressure profile contains no sharp discontinuity, which bears witness to subsonic propagation speed. No streamers appeared in the case of negative discharges in salt solutions with conductivity ≥ 0.4 S·m^{-1}. An expanding spherical cavity occurred instead; and this cavity produced spherical pressure wave. It was found that at solution conductivities of 0.4 and 0.8 S·m^{-1} the dependence of wave peak pressure (~4 MPa) on current is insignificant. At conductivity of 1.8 S·m^{-1} the peak pressure increases nearly twice (when converted to the same radius) and reaches 9 MPa at the wave radius of 0.5 mm, and significantly varies in experiments done under the same conditions. At conductivity of 3.8 S·m^{-1} the peak pressure falls down to only 3 MPa at the wave radius of 0.5 mm.

Numerical simulations were performed to find such temporal development of the radial velocity of the expanding discharge cavity, which produced a similar pressure profile as that detected by interferogram taken in one not exactly specified moment around discharges in the solution with conductivity of 1.8 S·m^{-1}.A qualified estimate based on this simulation gives plasma conductivity of the order of ~1 S·m^{-1} – i.e. value comparable with surrounding solution condutivity. The simulation has also showed that in the

beginning the cavity expands very slowly and does not generate any pressure wave, however, as soon as the cavity reaches radius ~100 μm, it starts to rapidly expand and generate the pressure wave.

Results of experiments focused on analyses of pressure waves produced by corona-like discharges on composite anode show that radial pressure profile of a typical semi-spherical wave with radius of 440 μm has a jump up to ~8 MPa with thickness of the transition region of 12 μm. Behind this jump the pressure monotonically increases up to 21 MPa. Since about 100 discharges burning on 100 mm^2 of composite anode have together the same current as the discharge on one needle electrode (at the same liquid conductivity) and since one individual discharge on a composite anode generates practically the same pressure as the discharge on the needle electrode, it is possible to concluded that the production of pressure waves by composite electrode is much more efficient than production by needle electrode

Pressure profile of spherical pressure waves generated by discharges on composite cathode monotonically increases from its outer radius to the inner one without any jump reaching the pressure of 20 MPa near the composite cathode surface.

The individual semi-spherical pressure waves generated by discharges on both composite anode and cathode are often not produced simultaneously, probably because of different filling of individual pores.

4.4 Generator of focused shockwaves based on multichannel corona-like discharges

The following chapters deal with experiments done with generator of shockwaves based on multichannel corona-like discharge. The physics of shock waves produced in water by electrohydraulic discharges has been studied for many years, in particular in systems using underwater spark gaps, due to their practical application. In medicine they have been used for extracorporeal shock wave lithotripsy [71] [72] and in industry for fragmentation of composite materials, e.g., recycling concrete [73]. This chapter is focused on physical properties of shock waves generated by underwater multichannel electrical discharge generated by cylindrical composite electrode aligned along the axis of symmetry of a semi-parabolic reflector. [74] [75] [55] [76] The pulsed electrical discharge is generated in conductive aqueous salt solution using a composite cylindrical electrode. The mechanism of the shock wave formation in this multichannel discharge system is different from the formation of shock waves by other methods, e.g., by electromagnetic systems, spark gaps, lasers, or explosions. In spark gap systems, a high current (~1 kA) underwater pulsed spark discharge between two point electrodes in the first focal point of a semi-ellipsoidal reflector is the source of a spherical shock wave, which focuses to the second focal point out of the reflector system. In the present system, a primary cylindrical diverging pressure wave is generated by the underwater multichannel pulsed electrical discharge, which is after reflection on parabolic reflector theoretically transformed to semi-spherical converging pressure wave that near the reflector focus subsequently changes by natural distortion into a shock wave. Large number of low current pulsed discharge channels are formed simultaneously on the surface of the composite cylindrical anode (top part of the Figure 65), which propagate only a short distance into the liquid (less than 1 mm) towards the walls of metallic semi-parabolic reflector serving as ground electrode. Each discharge channel creates a semi-spherical pressure wave in the liquid. By superposition of these waves, a primary cylindrical pressure wave is formed, which propagates from the composite cylindrical anode toward the reflector. This cylindrical pressure wave is reflected by the parabolic reflector and then is focused to a common focal point and close to the focus is transformed into a shock wave (bottom part of the Figure 65). The shock wave focusing with multichannel corona-like discharges on composite cylindrical anode has been used to study biological effects of shock waves in works [75] [76]; however, mechanism of shock wave focusing in this system has not yet been clarified. This chapter reports the results of real-time experiments with high spatial resolution performed to study shock wave focusing in water by this type of shock wave generator. Shock wave pressure profiles and pressure field near the focus were measured by a fiber optic probe hydrophone (FOPH). Dynamics of shock wave propagation through the focal area was studied using high speed real-time optical shadowgraph method.
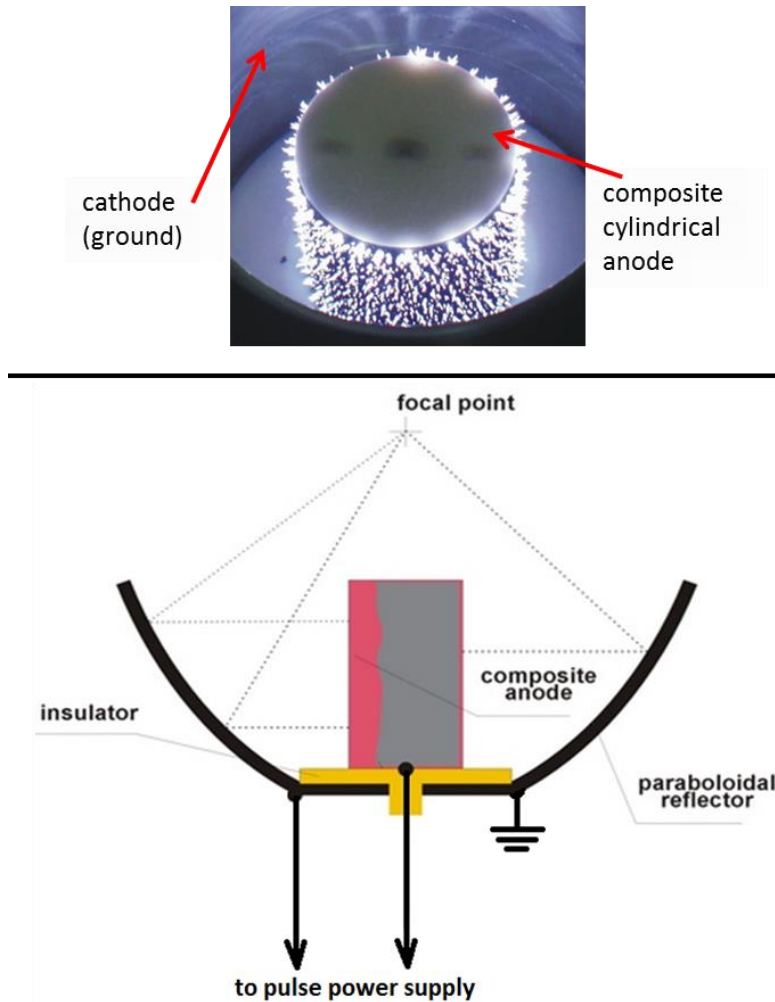
Figure 65 Large number of low current pulsed discharge channels formed on the surface of a composite cylindrical anode (top). Cross-section of generator of focused shockwaves; cylindrical pressure wave generated by the cylindrical composite anode is reflected by the parabolic reflector to a common focal point (bottom).

4.5 Experimental part 3

Experimental setup

Figure 67 shows a schematic diagram of the experimental setup. The shock wave generator consists of a cylindrical high-voltage composite anode placed along the axis of the outer metallic parabolic reflector (cathode) [75]. The cylindrical composite electrode has ⌀60 mm diameter and 100 mm length. The focal point of the parabolic reflector is 70 mm above the reflector's aperture. The pulse power supply consists of a high voltage DC source (model EW30P20, Glassman High Voltage, Inc.), a high voltage capacitor of 0.8 µF, and a spark gap switch. The electrode system is immersed in a conductive aqueous salt solution (1.8 S·m^{-1}). A pulse high voltage of positive polarity with amplitude of 21 kV was applied to the composite electrode. Pressure measurements were performed using a fiber optic probe hydrophone (FOPH 2000, RP Acoustics, Germany). Tip of the FOPH was placed in the generator's focal area, and signals from the FOPH's photo-detector were captured by a digital oscilloscope (Tektronix DPO 4104,

Shockwave generator immersed in saline water

High-speed camera

Flash lamp

FOPH

Delay unit

Pulse power supply

Current monitor

Oscilloscope
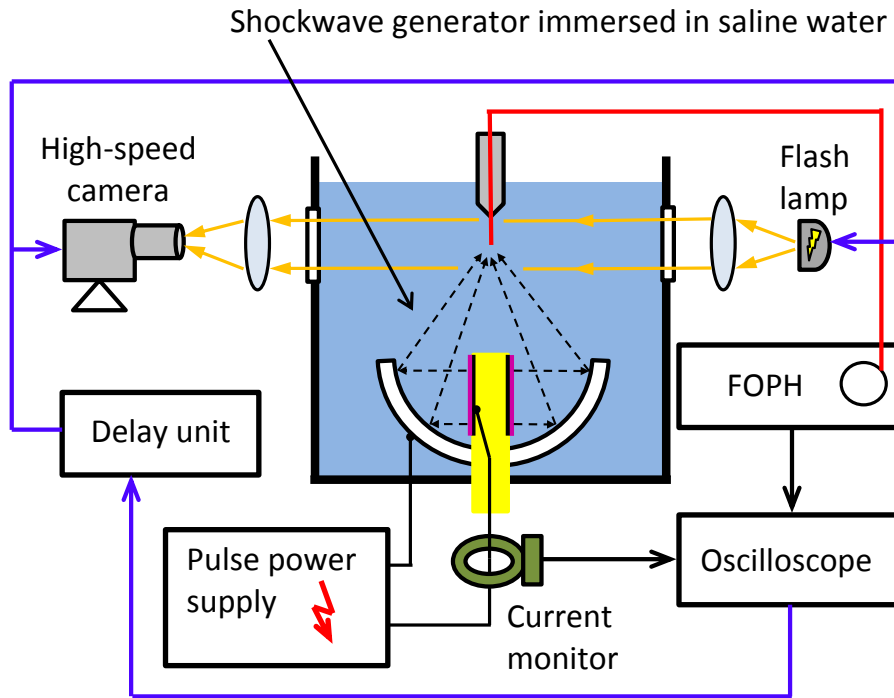
Figure 66 The experimental setup

USA). An ultra-high-speed camera (ULTRA-Neo, Nac Company, Japan) and a flash lamp were used for high speed real-time shadowgraph visualization of shock wave propagation and focusing in the focal area. A Pearson probe current monitor (Pearson, Model 101, USA) was used as a source of trigger signal. This signal directly triggered the oscilloscope and a delay unit (Stanford Research System Inc., Model DG535, USA), which was used to synchronize the timing of the flash lamp and the camera.

Results
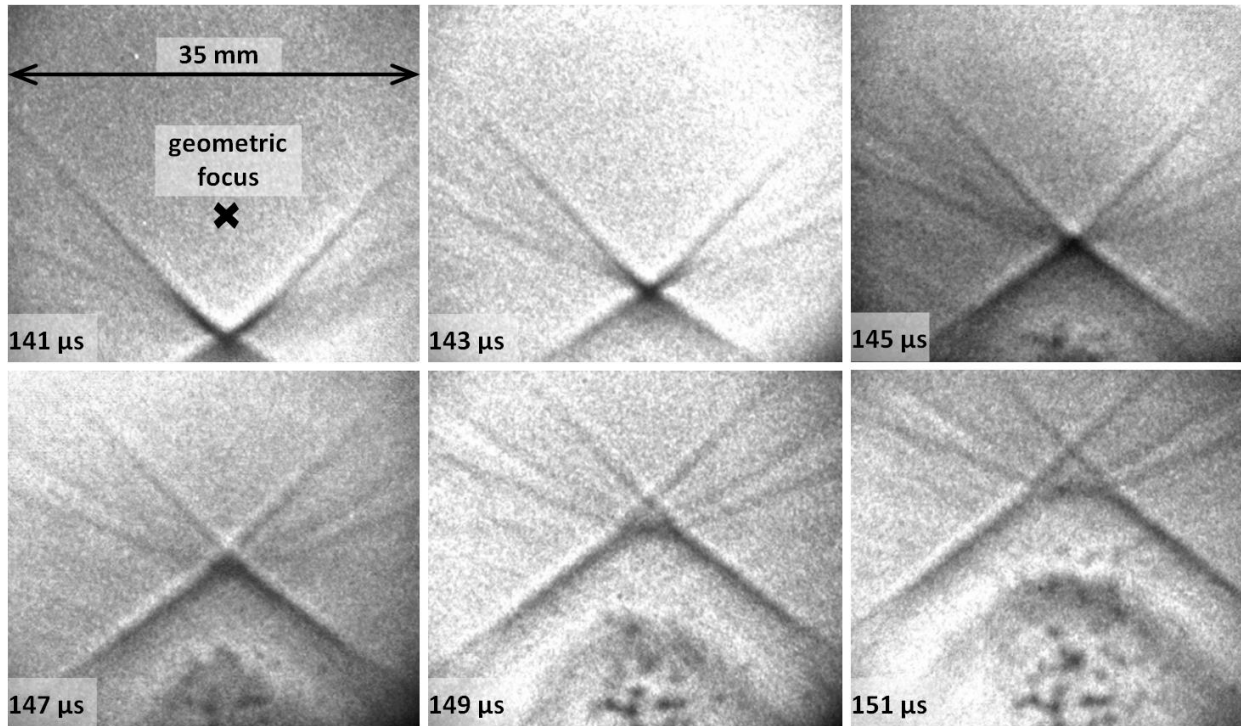
Figure 67 shows selected frames from real-time shadowgraph images of the shock wave propagation through the focal area in water. The shock wave propagated from the bottom to the top. In each experiment, 12 images were recorded with time interval of 1 μs and exposure time of 20 ns. The label on the bottom of each frame indicates the time delay between the pulse power supply trigger and the image capture by the high speed camera. The parabolic reflector's geometrical focal point is depicted in the first image. The images show that the primary diverging cylindrical pressure wave is transformed after reflection from the parabolic reflector into an approximately conical converging shock wave at the focus after reflection from the parabolic reflector. The shock front is visible in shadowgraphs as two lines intersecting on the axis of symmetry. A similar pattern has been observed for toroidal shock wave focusing [77] and imploding conical shock waves [78] in gases, however, this phenomenon in water or other liquid medium has not yet been verified. Here, the propagation of the shock wave is described by two parameters, which are deduced from the shadowgraphs in the Figure 67. The first parameter v_n describes the speed of shock front propagation in its normal direction and is determined from the shift of the intersecting lines with time to be $v_n = 1.51 \pm 0.1$ km·s^{-1} (Figure 68a). The second parameter v_{ip} describes the speed of propagation of the intersection point of the conical shock front in axial direction, and it is determined from the shift of an intersection point (Figure 68a) to be $v_{ip} = 2.17 \pm 0.1$ km·s^{-1}. In the

Figure 67 Selected real-time shadowgraph images of shock wave propagation through the focal area. The shock wave propagated from the bottom to the top of the frame.
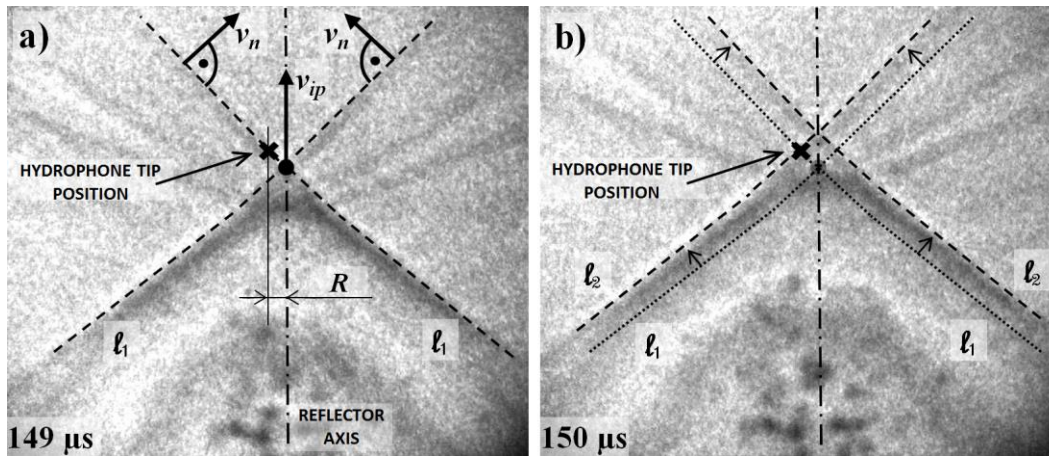
Figure 68 Analysis of shockwave propagation and development of multiple discontinuities in two successive shadowgraphs. v_n is the shock front normal velocity; v_{ip} is the shock velocity along the symmetry axis; R is the FOPH lateral distance, ℓ_1 and ℓ_2, positions of the shock fronts in 149th μs and 150th μs.

last two image frames of Figure 67, a rounded tip of conical expansion wave can be recognized behind the shock wave. Propagation speed of this expansion wave was approximately $v_e = 1.5 \pm 0.2$ km·s^{-1}. Cavitation produced by the expansion wave can be seen on these images.

Figure 69 shows the shock wave pressure waveforms measured by the FOPH at three different lateral distances (R) from the focus. The waveforms were measured in the axial distance of 7.5 mm above the geometric focus (i.e., 77.5 mm from the aperture of focusing reflector), where the shock wave amplitude reached its maximum value (see also Figure 70 and further text). In the focus ($R = 0$), the peak amplitude of the positive pressure wave was $p_{max} = 372$ MPa with a positive phase duration of 1.8 μs. The peak amplitude of the following negative pressure part was −17 MPa with duration of 2 μs. In some of the

79
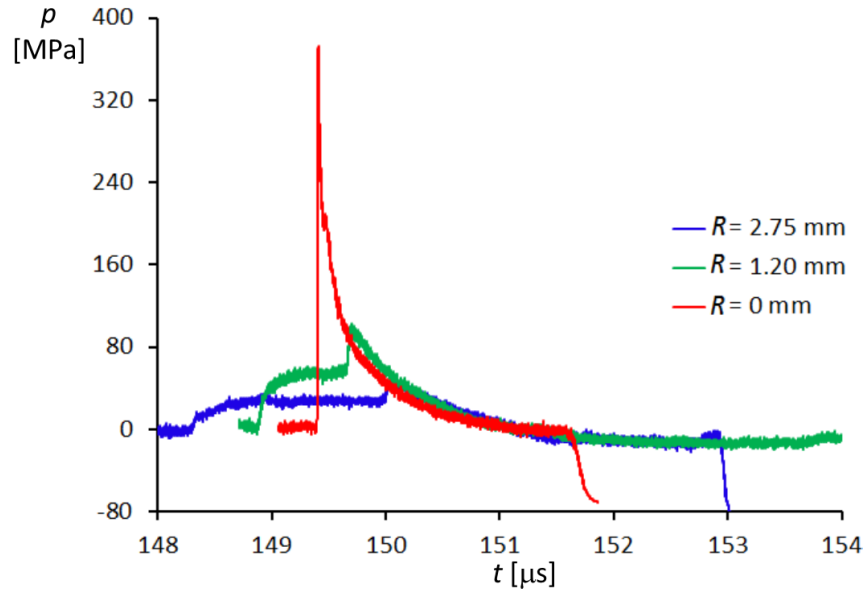
Figure 69 Shock wave pressure waveforms measured by the FOPH at three different lateral distances (R) from the focus.

measurements the negative pressure was affected by the occurrence of a spurious negative signal, which was caused by cavitation bubbles growing around the fiber optic tip. The FOPH measurements revealed much higher peak pressure in the focus than the measurements with polyvinylidene fluoride (PVDF) pressure sensors in the previous works [75] [76]. The peak positive/negative pressure amplitude of the same shock wave measured by PVDF pressure sensor with active area of 1 mm^2 (model S-25-01, Piezotech, France) was typically 50 MPa and -15 MPa, respectively [75]. Since the diameter of the active area of the FOPH (100 μm) is one order of magnitude smaller than PVDF (1 mm), FOPH can more accurately capture the pressure variation within the focal area smaller than 1 mm^2. This is further apparent from the shock wave peak pressure values measured outside the reflector axis (Figure 69), which rapidly decreased with lateral distance R from the focus (see also Figure 70).

In the Figure 69, the pressure waveforms measured in 1.20 and 2.75 mm of lateral distances from the focus have two discontinuities in the pressure waveform compared to only one pressure rise measured exactly in the focus. The first discontinuity is followed by a compression wave which creates a nearly constant pressure till the arrival of the shock wave reflected from the opposite side of the reflector. At the second shock wave discontinuity the pressure reaches its maximum value and then decreases. Figure 69 also shows that the pressure signals change their sign from the positive to the negative value in the same time (approx. 151.2 μs) independent of the probe distance from the reflector axis confirming that the expansion wave has a rather uniform front upon reaching the focal extension. The two pressure discontinuities in the Figure 69 showed that the probe tip is crossed by two shock fronts, which can be explained by the flow visualization results in the Figure 68a and the Figure 68b. The pressure waveform profiles in the Figure 69 correlate well with the time difference between the two discontinuities passing the hydrophone tip position in the Figure 68a and the Figure 68b.

From pressure waveforms measured by FOPH in different axial distances, the velocity of propagation of focusing shock front v_{ipFOPH} through the focal area was estimated in addition to the v_{ip} value determined from shadowgraphs. Combining the z-values of axial positions of the FOPH probe with times, at which the shock wave reached the probe, v_{ipFOPH} was determined to be 2.07 ± 0.11 km·s^{-1}, which is in good agreement with the value $v_{ip} = 2.17 \pm 0.1$ km·s^{-1}. Relation (4.29) was used to calculate the shock wave propagation speed (at zero electric field) corresponding to the obtained shock wave pressure p_{max}. Based
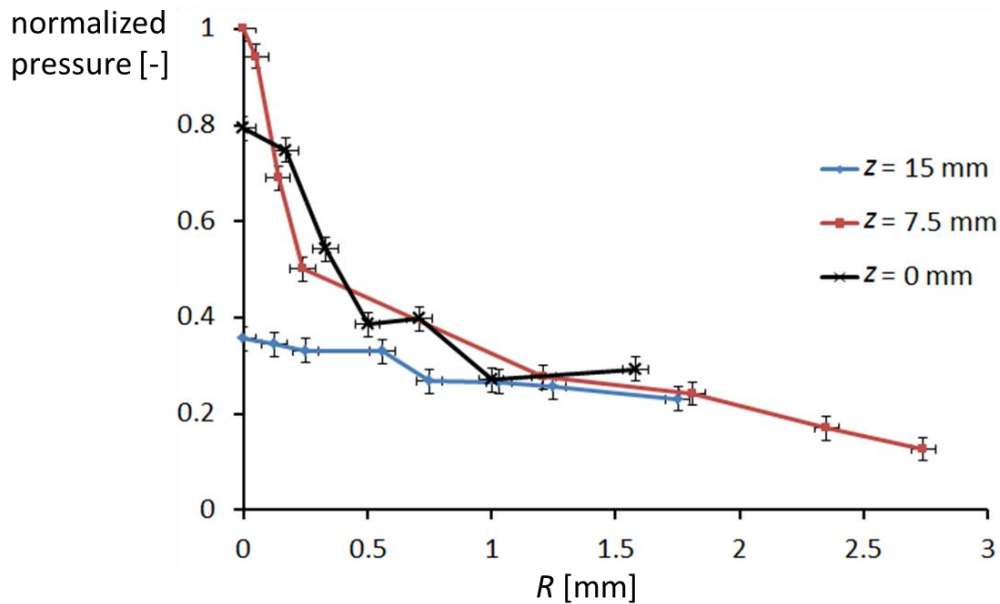
Figure 70 Variation of shock wave peak pressure with the lateral and axial distance from the focus. Pressure amplitudes were normalized by $p_{max} = 372$ MPa.

on this values of the shock pressure in the focus, $u_s = 1.89$ km·s^{-1} is calculated, which is considerably lower than the v_{ip} and v_{ipFOPH}. This confirms that v_{ip} (v_{ipFOPH}) is not shockwave normal velocity, but it is rather seeming propagation velocity of the intersection point determined by the geometry (vertex angle) of the intersecting conical shockwave.

Figure 70 shows variation of shock wave peak pressure measured in different lateral and axial distances from the geometric focus (the pressure values were normalized to the measured p_{max}). The maximum peak pressure and the highest radial dependence was measured in the axial position $z = 7.5$ mm above the geometric focus. The displacement of the real focus from the geometric one has been observed in a lithotripter field as well. This was attributed to a nonlinear propagation of the shock wave [79]. The corresponding diameter of the high pressure focal area (full width at half maximum (FWHM, −6 dB)) was 0.48 mm. In the axial direction, the dimension of high pressure area (−6 dB) was 22 mm, from $z = −8$ mm to $z = 14$ mm relative to the geometric focus position. In an axial distance of 15 mm above the geometric focus the main pressure peak nearly disappeared.

In this case the shock front of conical wave, which is otherwise visible in shadowgraphs as two lines intersecting in the vertex of double cone, does not cross anymore. A similar effect is also visible in the opposite axial direction.

Conclusions of the experimental part 3

In conclusion, the generation and focusing of shock waves generated by the multichannel corona-like discharge system with the composite cylindrical anode has been investigated. Experiments have shown that expanding cylindrical pressure wave produces after reflection a conical shock wave travelling along the axis of symmetry of the reflector. The pressure amplitudes of the shock wave rapidly decrease with lateral distance R from the focus (~0.25 mm), and the pressure waveforms significantly change with R. The maximum measured peak pressure of the focused shock wave was 372 MPa, averaged over the area of the FOPH (100 μm in diameter). The propagation velocity of the conical shock front in its normal

direction was 1.51 ± 0.1 km·s^{-1}. The propagation velocity of the intersection point of the conical shockwave on the axis of symmetry was 2.17 ± 0.1 km·s^{-1}.

Conclusion

One of the most frequent initiation mechanisms of underwater discharges is an electrical breakdown of bubbles on a metallic electrode, from which the discharge penetrates (through limited area of bubble-water interface) into liquid volume. This situation simulates experiments with *liquid anode* and *cathode* in glass capillaries that are described in the Experimental part 1. The experiments were aimed at studies of above mentioned penetration of plasma from the limited liquid surface (meniscus in the capillary) into the liquid volume. High speed shadowgraphy was used as the main diagnostic tool.

Experiments with *liquid anodes* showed, that liquid surface in the place of the largest current density (at the plasma-liquid interface) recedes. This receding is caused by reaction pressure resulting from liquid evaporation. Thus, long cavities with plasma inside can be formed or even can cause the total electrical breakdown. Propagation speed of the elongating cavity-wall is of the order of 1 m·s^{-1}, and it depends on current density. The liquid surface of the meniscus or cavity remains smooth when the liquid conductivity is larger than the conductivity of adjacent plasma. In the opposite case (if the liquid conductivity is smaller than the conductivity of adjacent plasma), the distribution of current density on the plasma-liquid boundary is unstable due to liquid evaporation. Any initial surface disturbances boost the current density in local surface valleys causing simultaneously a detriment of the surrounding current density. Consequent stronger liquid evaporation in the valleys causes their deepening, and hence, next enhancement of the current density distribution inhomogeneity. The dips created in this way subsequently elongate, and often fluently transform into negative streamers, when electric field larger than 1 MV·m^{-1} appears near the liquid surface. Based on this idea, the plasma conductivity was estimated to lie between of $14{-}140 \text{ mS·m}^{-1}$. Negative streamers propagate toward the immersed metal anode at subsonic speed of the order of 100 m·s^{-1}. Creation of negative streamers is preceded by spikes on the discharge current waveform.

Experiments with *liquid cathodes* showed significantly more intense liquid evaporation than the experiments with liquid anodes – under otherwise the same conditions. Therefore, elongation speed of gas cavities is also significantly higher. Although development of spikes on the liquid surface is also determined by the ratio of plasma-liquid conductivities, it is followed by transition to secondary positive streamers only when larger electric field than 10 MV·m^{-1} appears near the liquid surface. Also creation of positive secondary streamers is preceded by spikes on the discharge current waveform.

Besides the positive secondary streamers, slow positive streamers of low conductivity were rarely observed to grow from the liquid surface spikes. Propagation speed of these structures is of the order of 10 m·s^{-1}.

Experiments with corona-like discharges on needle and composite electrodes in aqueous salt solutions with different conductivities are reported in the Experimental part 2. The experiments were aimed at interferometry analysis of pressure field generated by the corona-like discharges. It has been found that pressure waves generated by positive coronas reach generally higher pressure levels.

Profile of spherical shockwave generated by primary discharge on *positive needle electrode* in distilled water was successfully analyzed. The shock front represents boundary of the driving fan-shaped primary streamer discharges; its pressure amplitude reaches 30 MPa at the wave radius 100 μm, and thickness of the shock front transition region is of the order of 1 μm.

Experiments with positive discharges in salt aqueous solutions showed high volume number density of positive streamers at conductivities 0.4 and 0.8 S·m^{-1}, which did not allow to recognize fringes in the captured interferograms. Spherical pressure waves around positive discharges in solutions with higher conductivities - 1.8 and 3.8 S·m^{-1} enabled pressure analysis yielding pressure amplitude in both cases 20 MPa at the wave radius 1 mm; the radial thickness of transition region is of the order of 100 μm. Since the discharge currents at these conductivities (1.8 and 3.8 S·m^{-1}) were comparable, similarly as the generated pressure levels, it has been concluded that the plasma conductivity of the discharges had to be

similar, and independent on conductivity of the salt solutions. At the highest conductivity (3.8 S·m^{-1}) streamers receded, and the pressure waves were generated rather by expanding bumpy cavity with only signs of streamers. It is in agreement with results of the Experimental part 1.

Profile of spherical pressure wave generated by discharge on *negative needle electrode* in distilled water was successfully analyzed. Maximum amplitude of pressure waves formed on tip of negative streamers in distilled water reaches 20 MPa. The pressure profile contains no sharp discontinuity, which bears witness to subsonic propagation speed.

No streamers appear in the case of negative discharges in salt solutions with conductivity ≥0.4 S·m^{-1}. Instead, an expanding nearly spherical cavity occurs and produces spherical pressure wave. The pressure waves generated by such expanding cavity have generally lower peak pressure than the pressure waves from discharges on positive needle electrode. It is not surprising with respect to differences in evaporation rates observed in the experiments with discharges in glass capillaries in the Experimental part 1, where evaporation of conductive salt solution working as the liquid cathode was significantly more intense than evaporation from the liquid anode. Dependence of the wave peak pressure on current has been found to be insignificant at lower solution conductivities (0.4 and 0.8 S·m^{-1}). The peak pressure reaches 4 MPa (at wave radius ~0.5 mm) for these conductivities. However, at conductivity of 1.8 S·m^{-1} the peak pressure increases nearly twice reaching ~9 MPa at the wave radius of 0.5 mm. At conductivity of 3.8 S·m^{-1} the peak pressure falls back to only ~3 MPa at the wave radius of 0.5 mm.

Numerical simulations were performed to find such temporal development of the radial velocity of the expanding discharge cavity, which produces a similar pressure profile as that detected around discharges on negative needle electrode in the salt solution with conductivity of 1.8 S·m^{-1}. From these simulations it was estimated that the plasma conductivity is of the order of 1 S·m^{-1}. The simulations and experiments also showed that in the beginning the cavity expands so slowly that this expansion does not generate any pressure wave; however, as soon as the cavity radius reaches ~100 µm the situation is just opposite: a rapid cavity expansion occurs and is accompanied by generation of strong pressure wave.

All this knowledge gained at studies of discharge penetration into liquid electrode can be used at analyses of discharges initiated on composite electrodes (electrodes covered by a thin layer of porous ceramics), where discharges start from gas-filled or partly/fully flooded pores.

Analysis of interferogram of corona-like discharges burning on *composite anode* in aqueous salt solution with conductivity of 1.8 S·m^{-1} showed that radial pressure profile of a typical semi-spherical pressure wave (due to the discharge from a single pore) with radius of 440 µm has on its front a pressure jump up to 8 MPa with thickness of the transition region of 12 µm. Behind this jump the pressure monotonically increases up to 21 MPa. Since there are many such simultaneous discharges, which have together the same current as the discharge burning from one needle electrode (at the same liquid conductivity), it can be concluded that production of pressure waves by composite electrodes is much more efficient.

The same similarity with needle electrode holds also in the case of *composite cathode*: the pressure profile of wave generated by a discharge from single pore monotonically increases from its outer radius to the pore without any jump reaching 20 MPa near the composite cathode surface.

The semi-spherical pressure waves generated by discharges on electrodes of both polarities (on composite anode and cathode) do not often have in one moment (moment of laser-shot generating interferogram) the same radii, probably because each discharge is initiated in slightly different time (due to various filling of pores).

Experiments with focused shockwaves generated by multichannel corona-like discharges on the cylindrical composite anode are described in the Experimental part 3. The experiments showed that expanding cylindrical pressure wave, which is formed by many elementary semi-spherical waves produced by surface corona-like discharges, creates after reflection from a parabolic reflector a conical shock wave travelling along the axis of symmetry of the reflector. The pressure amplitudes of the shock wave rapidly decrease with radial distance from the generator axis in the plane of real focus, which is slightly further than the geometrical focus of the parabolic reflector; it falls to half of its maximum at 0.25 mm. The pressure waveform also significantly changes with the radial distance. The measured peak

pressure of the focused shock wave reaches 372 MPa, averaged over the area of the fiber optic probe hydrophone (100 μm in diameter). The propagation velocity of the conical shock front in its normal direction is 1.51 ± 0.1 km·s^{-1}. The propagation velocity of the vertex of the conical shockwave on the axis of symmetry is at the given geometry 2.17 ± 0.1 km·s^{-1}.

The future work can continue in diagnostics and analysis of shock and pressure waves generated by corona-like discharges, but with improved apparatus. It is necessary to use high voltage pulsed power supply, which can be easily triggered and thus synchronized with diagnostic nanosecond laser. To achieve higher magnification of photographed small structures (e.g. shockwaves around primary discharges in distilled water) it is necessary to set up a new interferometer with smaller dimensions. Simultaneously a new heavy-duty glass cuvette capable to withstand impact of shockwaves produced by spark breakdown between electrodes has to be designed and constructed. This enables to eliminate any high-voltage resistors limiting maximum current in driving circuit by voltage loss across them.

References

[1] J. R. Roth, Industrial Plasma Engineering, Volume 1: Principles, London: Institute of Physics Publishing, 1995.

[2] J. D. Meek and J. M. Craggs, Electrical Breakdown of Gases, John Wiley and Sons, Ltd., 1978.

[3] H. Reather, Electron Avalanches and Breakdown in Gases, London: Butterworth and Co. Ltd., 1964.

[4] J. Kracík, J. B. Slavík and J. Tobiáš, Elektrické výboje, Praha: Státní nakladatelství technické literatury, 1964.

[5] A. von Engel, Ionized Gases, Oxford: Clarendon Press, 1965.

[6] Y. P. Raizer and E. M. Bazelyan, Lightning Physics and Lightning Protection, London: IOP Publishing Ltd, 2000.

[7] Y. Seepersad, M. Pekker, M. N. Shneider, A. Fridman and D. Dobrynin, "Investigation of positive and negative modes of nanosecond pulsed discharge in water and electrostriction model of initiation," *J. Phys. D,* vol. 46, p. 355201, 2013.

[8] M. Goldman, A. Goldman and R. S. Sigmond, "The Corona Discharge, its Properties and Specific Uses," *Pure & Appi. Chem.,* vol. 57, p. 1353—1362, 1985.

[9] R. S. Sigmond, "The Oscillations of the Positive Glow Corona," *Journal de Physique IV,* vol. 07, no. C4, pp. C4-383 - C4-395, 1997.

[10] W. R. Rutgers and E. M. van Veldhuizen, "Pulsed Positive Corona Streamer Propagation and Branching," *J. Phys. D: Appl. Phys.,* vol. 35, p. 2169–2179, 2002.

[11] T. J. Lewis, "Breakdown Initiating Mechanisms at Electrode Interfaces in Liquids," *IEEE Transactions on Dielectrics and Electrical Insulation,* vol. 10, pp. 948-955, 2003.

[12] V. Y. Ushakov, Impulse Breakdown of Liquids, Heidelberg: Springer-Verlag, 2007.

[13] A. Starikovskiy, Y. Yang, Y. I. Cho and A. Fridman, "Non-equilibrium plasma in liquid water: dynamics of generation and quenching," *Plasma Sources Sci. Technol.,* vol. 20, p. 7pp, 2011.

[14] A. Denat, "High Field Conduction and Prebreakdown Phenomena in Dielectric Liquids," *IEEE Transactions on Dielectrics and Electrical Insulation,* vol. 13, pp. 518-525, 2006.

[15] K. Schoenbach, J. Kolb, S. Xiao, S. Katsuki, Y. Minamitani and R. Joshi, "Electrical Breakdown of Water in Microgaps," *Plasma Sources Sci. Technol.,* vol. 17, p. 024010 (10), 2008.

[16] J. R. Melcher, Continuum Electromechanics, Cambridge, Massachusetts, London: The MIT Press, 1981.

[17] M. N. Shneider and M. Pekker, "Dielectric fluid in inhomogeneous pulsed electric field," *Phys. Rev.,* vol. 87, p. 043004(7), 2013.

[18] M. Pekker, Y. Seepersad, M. N. Shneider, A. Fridman and D. Dobrynin, "Initiation stage of nanosecond breakdown in liquid," *J. Phys. D: Appl. Phys.,* vol. 47, p. 025502, 2014.

[19] Y. Seepersad, M. Pekker, M. N. Shneider, D. Dobrynin and A. Fridman, "On the electrostrictive mechanism of nanosecond-pulsed breakdown in liquid phase," *J. Phys. D: Appl. Phys.,* vol. 46, p. 162001(6), 2013.

[20] C. E. Brennen, Cavitation and Bubble Dynamics, Oxford: Oxford University Press, 1995.

[21] E. Herbert, S. Balibar and F. Caupin, "Cavitation pressure in water," *Phys. Rev. E,* vol. 74, no. 4, p. 041603(22), 2006.

[22] T. G. Leighton, The Acoustic Bubble, San Diego: Academic Press, 1994.

[23] M. V. Kosevich, V. S. Shelkovsky, O. A. Boryak and V. V. Orlov, "'Bubble Chamber Model' of Fast Atom Bombardment Induced Processes," *Rapid Commun. Mass Spectrom.,* vol. 17, pp. 1781-

1792, 2003.

[24] R. D. Finch, "Influence of Radiation on The Cavitation Threshold of Degassed Water," *J. Acoust. Soc. Am.,* vol. 36, no. 12, pp. 2287-2292, 1964.

[25] D. Sette and F. Wanderlingh, "Nucleation by Cosmic Rays in Ultrasonic Cavitation," *Phys. Rev.,* vol. 125, no. 2, pp. 409-417, 1962.

[26] R. Maceška, "Měření vodivosti kapalin," Vysoké učení technické v Brně, Brno, 2009.

[27] J. A. Dean, Lange's Handbook of Chemistry, New York: McGraw-Hill, 1972.

[28] M. A. Margulis, Sonochemistry and Cavitation, Amsterdam: Gordon and Breach Science Publishers, 1995.

[29] A. Saul and W. Wagner, "International Equations for the Saturation Properties of Ordinary Water Substance," *J. Phys. Chem. Ref. Data,* vol. 16, pp. 893-901, 1987.

[30] N. B. Vargaftik, B. N. Volkov and L. D. Voljak, "Inrenational Tables of the Surface Tension of Water," *J. Phys. Chem.,* vol. 12, pp. 817-820, 1983.

[31] N. Škoro, D. Marić, G. Malović, W. G. Graham and Z. Petrović, "DC Breakdown in Water Vapour at Low Pressures," in *Proceedings of 20th European Conference on the Atomic and Molecular Physics of Ionized Gases* , Novi Sad, 2010.

[32] M. Radmilović-Radjenović, B. Radjenović and M. Savić, "Breakdown Phenomena in Water Vapor Microdischarges," *Acta Physica Polonica A,* vol. 117, pp. 752-755, 2010.

[33] E. J. Rothwell and M. J. Cloud, Electromagnetics, London: CRC Press LLC, 2001.

[34] K. C. Kao, "Some Electromechanical Effects on Dielectrics," *British Journal of Applied Physics,* vol. 12, pp. 629-632, 1961.

[35] E. Hourdakis, G. W. Bryant and N. M. Zimmerman, "Electrical Breakdown in the Microscale: Testing the Standard Theory," *J. of App. Phys. ,* vol. 100, p. 123306(6), 2006.

[36] A. Vankov and D. Palanker, "Nanosecond Plasma-Mediated Electrosurgery with Elongated Electrodes," *Journal of Applied Physics,* vol. 101, p. 124701(7), 2007.

[37] K. Tachibana, Y. Takekata, Y. Mizumoto, H. Motomura and M. Jinno, "Analysis of a pulsed discharge within single bubbles in water under synchronized conditions," *Plasma Sources Sci. Technol.,* vol. 20, p. 034005 (12), 2011.

[38] P. Bruggeman, J. Degroote, C. Leys and J. Vierendeels, "Plasma Characteristics in Air and Vapor Bubbles in Water," in *Proceedings of 28th International Conference on Phenomena in Ionized Gases*, Prague, 2007.

[39] P. Bruggeman, D. Degroote, J. Vierendeels and C. Leys, "DC-excited Discharges in Vapour Bubbles in Capillaries," *Plasma Sources Sci. Technol.,* vol. 17, p. 025008 (7), 2008.

[40] P. Bruggeman, E. Ribežl, A. Maslani, J. Degroote, A. Malesevic, R. Rego, J. Vierendeels and C. Leys, "Characteristics of Atmospheric Pressure Air Discharges With a Liquid Cathode and a Metal Anode," *Plasma Sources Sci. Technol.,* vol. 17, p. 025012 (11), 2008.

[41] P. Mezei, T. Cserfalvi and L. Csillag, "The Spatial Distribution of The Temperatures and The Emitted Spectrum in The Electrolyte Cathode Atmospheric Glow Discharge," *J. Phys. D: Appl. Phys.,* vol. 38, p. 2804–2811, 2005.

[42] P. Mezei and T. Cserfalvi, "Charge Densities in The Electrolyte Cathode Atmospheric Glow Discharges (ELCAD)," *Eur. Phys. J. Appl. Phys.,* vol. 40, p. 89–94, 2007.

[43] A. Kulentsan, V. Rybkin, T. Titov and S. Smirnov, "Physical Characteristics of Atmospheric Pressure Glow Discharge With Liquid Electrolyte Cathode (Water and CuCl2 Solutions)," in *ICPIG*, Prague, 2007.

[44] M. R. Webb, G. Chan, F. J. Andrade, G. Gamez and G. M. Hieftje, "Spectroscopic Characterization of Ion and Alectron Populations in a Solution-Cathode Glow Discharge," *J. Anal. At. Spectrom.,* vol.

21, p. 525–530 , 2006.

[45] P. Bruggeman, J. Liu, J. Degroote, M. G. Kong, J. Vierendeels and C. Leys, "Dc Excited Glow Discharges in Atmospheric Pressure Air in Pin-to-Water Electrode Systems," *J. Phys. D: Appl. Phys.,* vol. 41, p. 215201 (11), 2008.

[46] D. Staack, B. Farouk, A. Gutsol and A. Fridman, "Characterization of a DC Atmospheric Pressure Normal Glow Discharge," *Plasma Sources Sci. Technol.,* vol. 14, p. 700–711, 2005.

[47] W. An, K. Baumung and H. Bluhm, "Underwater Streamer Propagation Analyzed from Detailed Measurements of Pressure Release," *J. Appl. Phys.,* vol. 101, p. 053302(10), 2007.

[48] J. F. Kolb, R. P. Joshi, S. Xiao and K. H. Schoenbach, "Streamers in Water and Other Dielectric Liquids," *J. Phys. D: Appl. Phys.,* vol. 41, p. 234007 (22), 2008.

[49] P. Bruggeman and C. Leys, "Non-thermal Plasmas in And in Contact with Liquids," *J. Phys. D: Appl. Phys.,* vol. 42, p. 053001(28), 2009.

[50] H. Fujita, S. Kanazawa, K. Ohtani, A. Komiya and T. Sato, "Role of Pulsed Repetitive Current for Positive Primary Streamers in Water," in *21. International Symposium on Plasma Chemistry*, Cairns, 2013.

[51] I. V. Lisitsyn, H. Nomiyama, S. Katsuki and H. Akiyama, "Thermal Processes in a Streamer Discharge in Water," *IEEE Transactions on Dielectrics and Electrical Insulation,* vol. 6, pp. 351-356, 1999.

[52] M. Šimek, M. Člupek, V. Babický, P. Lukeš and P. Šunka, "Emission Spectra of a Pulse Needle-to-Plane Corona-Like Discharge in Conductive Aqueous Solutions," *Plasma Sources Sci. Technol.,* vol. 21, p. 055031 (12), 2012.

[53] J. Nieto-Salazar, N. Bonifaci, A. Denat and O. Lesaint, "Characterization and Spectroscopic Study of Positive Streamers in Water," in *IEEE Int. Conf. Dielectric Liquids*, Coimbra, 2005.

[54] L. Bok-Hee, K. Dong-Seong and C. Jong-Hyuk, "Underwater Discharge Phenomena in Inhomogeneous Electric Fields Caused by Impulse Voltages," *Journal of Electrical Engineering & Technology,* vol. 5, pp. 329-336, 2010.

[55] P. Lukes, M. Clupek, V. Babicky and P. Sunka, "Pulsed Electrical Discharge in Water Generated Using Porous-Ceramic-Coated Electrodes," *IEEE Transactions on Plasma Science,* vol. 36, pp. 1146-1147, 2008.

[56] Y. A. Barinov, V. B. Kaplan, V. V. Rozhdestvenski and S. M. Shkol'nik, "Determination of The Electron Density in a Discharge with Nonmetallic Liquid Electrodes in Atmospheric-Pressure Air from the Absorption of Microwave Probe Radiation," *Tech. Phys. Lett.,* vol. 24, pp. 929-931, 1998.

[57] P. Ceccato, "Filamentary Plasma Rischarge Inside Water : Initiation and Propagation of a Plasma in a Dense Medium," Phd Report, 2009.

[58] I. M. Gavrilov, V. R. Kukhta, V. V. Lopatin and P. G. Petrov, "Dynamics of Prebreakdown Phenomena in a Uniform Field in Water," *IEEE Transactions on Dielectrics and Electrical Insulation,* vol. 1, pp. 496-502, 1994.

[59] J. R. Roth, Industrial Plasma Engineering, Volume 2, London: Institute of Physics Publishing, 2001.

[60] Y. B. Zel'dovich and Y. P. Raizer, Physics of Shock Waves and High-Temperature Hydrodynamic Phenomena, New York and London: Academic Press, 1966.

[61] G. Ben-Dor, O. Igra and T. Elperin, Handbook of Shock Waves, Vol. 1, London: Academic Press, 2001.

[62] M. F. Hamilton and D. T. Blackstock, Nonlinear Acoustics, New York: Academic Press, 1998.

[63] M. Cowperthwaite, "Significance of Some Equations of State Obtained from Shock-Wave Data," *Am. J. Phys.,* vol. 34, pp. 1025-1030, 1965.

[64] V. K. Kedrinskii, Hydrodynamics of Explosion, Berlin: Springer-Verlag Berlin Heidelberg, 2005.

[65] X. Yousheng, X. Hongsen, G. Jie, Z. Haifei , Z. Yueming and S. Maoshuang, "Conductivity of NaCl solution at 0.4-5.0 GPa and 25-500 °C," *Science in China,* vol. 40, pp. 398-402, 1997.

[66] B. Gross, Měření vysokých teplot, Praha: SNTL, 1962.

[67] L. Weiss, A. Tazibt, A. Tidu and M. Aillerie, "Water Density and Polarizability Deduced from the Refractive Index Determined by Interferometric Measurements up to 250 MPa," *J. Chem. Phys.,* vol. 136, p. 124201 (8), 2012.

[68] Comsol, "CFD Module User's Guide," COMSOL, Inc., 2013.

[69] I. V. Timoshkin, R. A. Fouracre, M. J. Given and S. J. MacGregor, "Hydrodynamic Modelling of Transient Cavities in Fluids Generated by High Voltage Spark Discharges," *J. Phys. D: Appl. Phys.,* vol. 39, pp. 4808-4817, 2006.

[70] B. d. Darwent, "Bond Dissociation Energies in Simple Molecules," Nat. Stand. Ref. Data Ser., Nat. Bur. Stand. (U.S.), Washington, 1970.

[71] A. J. Coleman and J. E. Saunders, "A Review of the Physical Properties and Biological Effects of the High Amplitude Acoustic Fields Used in Extracorporeal Lithotripsy," *Ultrasonics,* vol. 31, pp. 75-89, 1993.

[72] R. O. ClevelandR. and J. A. McAteer, "The Physics of Shock Wave Lithotripsy," in *Smith's Textbook of Endourology*, Wiley-Blackwell, 2012, p. 527.

[73] H. Bluhm, W. Frey, H. Giese, P. Hoppe, C. Schultheiss and R. Strassner, "Application of Pulsed HV Discharges to Material Fragmentation and Recycling," *IEEE Trans. Dielectr. Electr. Insul.,* vol. 7, no. 5, pp. 625 - 636, 2000.

[74] P. Sunka, V. Babicky, M. Clupek, M. Fuciman, P. Lukes, M. Simek, J. Benes, B. R. Locke and Z. Majcherova, "Potential Applications of Pulse Electrical Discharges in Water," *Acta Phys. Slovaca,* vol. 54, no. 2, pp. 135-145, 2004.

[75] P. Sunka, V. Babicky, M. Clupek, J. Benes and P. Pouckova, "Localized damage of tissues induced by focused shock waves," *IEEE Trans. Plasma Sci.,* vol. 32, no. 4, pp. 1609 - 1613, 2004.

[76] V. Stelmashuk and P. Hofferp, "Shock Waves Generated by an Electrical Discharge on Composite Electrode Immersed in Water With Different Conductivities," *IEEE Transactions on Plasma Science,* vol. 40, no. 7, pp. 1907-1912, 2012.

[77] S. H. R. Hosseini and K. Takayama, "Experimental Study of Toroidal Shock Wave Focusing in a Compact Vertical Annular Diaphragmless Shock Tube," *Shock Waves,* vol. 20, no. 1, pp. 1-7, 2010.

[78] B. W. Skews, N. Menon, M. Bredin and E. V. Timofeev, "Imploding Conical Shock Waves," *Shock Waves,* vol. 11, no. 4, pp. 959-964, 2002.

[79] M. A. Averkiou and R. O. Cleveland, "Modeling of an Electrohydraulic Lithotripter with the KZK Equation," *J. Acoust. Soc. Am.,* vol. 106, pp. 102-112, 1999.

[80] P. Kulhánek, Úvod do teorie plazmatu, Praha: Aldebaran Group for Astrophysics, 2011.

[81] V. V. Gogosov and V. A. Polyansky, "Shock Waves in Electrohydrodynamics," *Prog. Aerospace Sci.,* vol. 20, pp. 125-216, 1983.

[82] G. Siedler and H. Peters, "Properties of sea water, physical properties (general)," in *Landolt-Bornstein, Numerical Data and Functional Relationships in Science and Technology, New Series , Ocenaography*, Berlin, Springer, 1986, pp. 233-264.

[83] X. Quan and E. S. Fry, "Empirical Equation for the Index of Refraction of Seawater," *Optical Society of America,* vol. 34, pp. 3477-3480, 1995.

Appendixes

Appendix 1

Derivation of the equations (4.4) and (4.8):
The laws of conservation of mass, charge, momentum, and energy are expressed by equations of continuity [80]:

$$\frac{\partial \rho}{\partial t} + \nabla \cdot (\rho \vec{u}) = 0, \frac{\partial \rho_Q}{\partial t} + \nabla \cdot \vec{j} = 0, \qquad \text{(A1.1) (A1.2)}$$

$$\frac{\partial}{\partial t}\left(\rho\vec{u} + \vec{D} \times \vec{B}\right) + \nabla \cdot \left(\overleftrightarrow{T}_P + \overleftrightarrow{T}_E + \overleftrightarrow{T}_M\right) = \vec{0}, \qquad \text{(A1.3)}$$

$$\frac{\partial \rho}{\partial t}\left(\frac{\rho u^2}{2} + e + \frac{\vec{E}\cdot\vec{D}}{2} + \frac{\vec{H}\cdot\vec{B}}{2}\right) + \nabla \cdot \left(\frac{\rho u^2}{2}\vec{u} + e\vec{u} + \overleftrightarrow{P}\cdot\vec{u} + \vec{q} + \vec{E} \times \vec{H}\right) = 0. \qquad \text{(A1.4)}$$

Quantities in these equations are these: ρ is liquid density, ρ_Q is charge density, $\vec{u}$ is velocity vector, $\vec{j}$ is current density vector, $\vec{D}$ and $\vec{E}$ are displacement and electric field vectors, $\vec{B}$ [T] and $\vec{H}$ [A·m⁻¹] are magnetic flux density and magnetic field vectors, e is internal energy, and $\vec{q}$ is heat flux vector. Neglecting liquid viscosity, the tensors $\overleftrightarrow{T}_P$ and $\overleftrightarrow{T}_E$ are given by

$$\overleftrightarrow{T}_P = p\overleftrightarrow{1} + \rho\vec{u}\otimes\vec{u}, \overleftrightarrow{T}_E = \frac{\vec{E}\cdot\vec{D}}{2}\overleftrightarrow{1} - \vec{E}\otimes\vec{D} \,, \; \overleftrightarrow{T}_M = \frac{\vec{H}\cdot\vec{B}}{2}\overleftrightarrow{1} - \vec{H}\otimes\vec{B}, \qquad \text{(A1.5) (A1.6) (A1.7)}$$

where $p\overleftrightarrow{1} = \overleftrightarrow{P}$, and symbol $\otimes$ means tensor product.

Using of equations (A1.1)-(A1.4) on shock front, time derivatives disappears in steady state (fluid does not accumulate on shock front, internal energy, velocities, and field vectors on both sides of shock front do not change with time). Next, when thickness of shock front goes to zero, the equations (A1.1)-(A1.4) can be written in form:

$$(\rho_2\vec{u}_2 - \rho_1\vec{u}_1) \cdot \vec{n} = 0, \; (\vec{j}_2 - \vec{j}_1) \cdot \vec{n} = -\frac{\partial \xi}{\partial t} \qquad \text{(A1.8) (A1.9)}$$

$$\left[\overleftrightarrow{T}_{P2} + \overleftrightarrow{T}_{E2} + \overleftrightarrow{T}_{M2} - \left(\overleftrightarrow{T}_{P1} + \overleftrightarrow{T}_{E1} + \overleftrightarrow{T}_{M1}\right)\right] \cdot \vec{n} = \vec{0} \qquad \text{(A1.10)}$$

$$\begin{bmatrix} \frac{\rho_2 u_2^2}{2}\vec{u}_2 + e_2\vec{u}_2 + p_2\vec{u}_2 + \vec{q}_2 + \vec{E}_2 \times \vec{H}_2 - \\ \left(\frac{\rho_1 u_1^2}{2}\vec{u}_1 + e_1\vec{u}_1 + p_1\vec{u}_1 + \vec{q}_1 + \vec{E}_1 \times \vec{H}_1\right) \end{bmatrix} \cdot \vec{n} = 0. \qquad \text{(A1.11)}$$

Let's divide the vectors on two parts perpendicular to each other: $\vec{a} = \vec{a}_\perp + \vec{a}_{||}$, where symbol $\perp$ resp. $||$ represents the part of a vector perpendicular resp. tangential to the shock front. Equations (A1.8), (A1.9), and (A1.11) are equations (4.4), (4.5), and (4.8) after multiplication by the unit vector $\vec{n}$ normal to shock front (only vector parts acting on the shock front surface are important), and by neglecting heat flux.

Now, if $\vec{D} = \varepsilon\vec{E}$ and $\vec{B} = \mu\vec{H}$, with liquid permittivity and permeability ε and μ, the tensors multiplied by the unit normal vector are

$$\overleftrightarrow{T}_P \cdot \vec{n} = \left[\begin{pmatrix} p & 0 \\ 0 & p \end{pmatrix} + \rho\begin{pmatrix} u_\perp^2 & u_\perp u_{||} \\ u_\perp u_{||} & u_{||}^2 \end{pmatrix}\right] \cdot \vec{n} = \rho\begin{pmatrix} u_\perp^2 \\ u_\perp u_{||} \end{pmatrix} + \begin{pmatrix} p \\ 0 \end{pmatrix} \qquad \text{(A1.12)}$$

$$\overset{\leftrightarrow}{T_E} \cdot \vec{n} = \begin{pmatrix} \frac{\vec{E} \cdot \vec{D}}{2} - E_{\perp} D_{\perp} & -E_{\perp} D_{||} \\ -E_{||} D_{\perp} & \frac{\vec{E} \cdot \vec{D}}{2} - E_{||} D_{||} \end{pmatrix} \cdot \vec{n} = \begin{pmatrix} -\frac{\varepsilon}{2}\left(E_{\perp}^2 - E_{||}^2\right) \\ -\varepsilon E_{\perp} E_{||} \end{pmatrix} \tag{A1.13}$$

$$\overset{\leftrightarrow}{T_M} \cdot \vec{n} = \begin{pmatrix} \frac{\vec{H} \cdot \vec{B}}{2} - H_{\perp} B_{\perp} & -H_{\perp} B_{||} \\ -H_{||} B_{\perp} & \frac{\vec{H} \cdot \vec{B}}{2} - H_{||} B_{||} \end{pmatrix} \cdot \vec{n} = \begin{pmatrix} -\frac{1}{2\mu}\left(B_{\perp}^2 - B_{||}^2\right) \\ -\frac{1}{\mu} B_{\perp} B_{||} \end{pmatrix}. \tag{A1.14}$$

After substitution of the equations (A1.12), (A1.13), and (A1.14) into the equation (A1.10), it leads to a pair of equations

$$\left[\rho u_{\perp}^2 + p - \frac{\varepsilon}{2}\left(E_{\perp}^2 - E_{||}^2\right) - \frac{1}{2\mu}\left(B_{\perp}^2 - B_{||}^2\right)\right]_1^2 = 0, \tag{A1.15}$$

$$\left[\rho u_{\perp} u_{||} - \varepsilon E_{\perp} E_{||} - \frac{1}{\mu} B_{\perp} B_{||}\right]_1^2 = 0, \tag{A1.16}$$

where $[a]_1^2 = a_2 - a_1$. The equation (A1.15) is the equation (4.6) after neglecting magnetic field. Since directions of tangential parts of the vectors may be arbitrary, unlike direction of normal parts perpendicular to the shock front, the equation (A1.16) is written more generally as [81]

$$\rho u_{\perp} \left[\vec{u}_{||}\right]_1^2 - \vec{E}_{||} \left[\varepsilon E_{\perp}\right]_1^2 = \vec{0}, \tag{A1.17}$$

which is the equation (4.7). The tangential parts of the electric field are the same on both sides of the shock front if changing magnetic field can be neglected ($\nabla \times \vec{E} = -\partial\vec{B}/\partial t$).

Appendix 2

Derivation of the equations (4.25) and (4.26):

From the equation (4.24) it is known that $\rho_2 u_{\perp 2} = \rho_2\left(u_s - u_p\right) = \rho_1 u_s$. Substitution of $\rho_1 u_s$ into the equation (4.15) leads to $\rho_1 u_s\left(u_s - u_p\right) + p_2 + p_{E2} = \rho_1 u_s^2 + p_1 + p_{E1}$, which, after an rearrangement, gives the equation

$$\rho_1 u_s u_p = p_2 - p_1 + p_{E2} - p_{E1}. \tag{A2.1}$$

From the equation (4.24) further follow these identities:

$$u_s = u_p \frac{\rho_2}{\rho_2 - \rho_1}, \; u_p = u_s \frac{\rho_2 - \rho_1}{\rho_2}. \tag{A2.2)(A2.3}$$

Putting of equations (A2.2) and (A2.3) into the equation (A2.1) leads to the equations (4.25) and (4.26).

Derivation of the equation (4.27):

Substitution of $\rho_2 u_{\perp 2} = \rho_1 u_s$ form the equation (4.24) into the equation (4.17) simplifies it to

$$e_1 + \frac{p_1}{\rho_1} + \frac{1}{2}u_{\perp 1}^2 = e_2 + \frac{p_2}{\rho_2} + \frac{1}{2}u_{\perp 2}^2. \tag{A2.4}$$

The equations (4.14) and (4.15) yield relations for the normal velocities [60]:

$$u_{\perp 1}^2 = \frac{p_2 + p_{E2} - (p_1 + p_{E1})}{\rho_1^2\left(\frac{1}{\rho_1} - \frac{1}{\rho_2}\right)}, \quad u_{\perp 2}^2 = \frac{p_2 + p_{E2} - (p_1 + p_{E1})}{\rho_2^2\left(\frac{1}{\rho_1} - \frac{1}{\rho_2}\right)}. \tag{A2.5) (A2.6}$$

Putting of equations (A2.5) and (A2.6) into the equation (A2.4) leads to the equation

$$e_2 - e_1 + \frac{p_2 + p_{E2} - (p_1 + p_{E1})}{2\left(\frac{1}{\rho_1} - \frac{1}{\rho_2}\right)}\left(\frac{1}{\rho_2^2} - \frac{1}{\rho_1^2}\right) + \frac{p_2}{\rho_2} - \frac{p_1}{\rho_1} = 0,$$

which, after an rearrangement, gives the equation (4.27).

Appendix 3

Salinity of NaCl water solution, which is basically a measure of the mass of salt per unit mass of salt water, can be determined by this formula [82]:

$$S_a(R_{15}) = s_0 + s_1 R_{15} + s_2 R_{15}^2 + s_3 R_{15}^3 + s_4 R_{15}^4 + s_5 R_{15}^5 \qquad [\text{‰}], \qquad (A3.1)$$

where $s_0 = -0.08996$ ‰, $s_1 = 28.2972$ ‰, $s_2 = 12.80832$ ‰, $s_3 = -10.67869$ ‰, $s_4 = 5.98624$ ‰ and $s_5 = -1.32311$ ‰. R_{15} is the ratio $R_{15} = \sigma(S_a, 15,0)/\sigma(35,15,0)$, where $\sigma(S_a,15,0)$ is the conductivity of water solution with the given salinity S_a at 15 °C at normal pressure, and $\sigma(35,15,0)$ is the Normal Water conductivity at 15 °C at normal pressure, whose value is of 4.29 S·m^{-1}. The formula is valid for 2 ‰ $\leq S_a$ $\leq$ 42 ‰, and standard deviation is of 1.5·10^{-3} ‰.

Density of a NaCl water solution depends on its salinity, pressure and temperature. For normal pressure (101.325 kPa) the density is described by the following *One Atmosphere International Equation of State of Water* [82]:

$$\rho_s(T, S_a) = \rho_w(T) + (a_0 + a_1 T + a_2 T^2 + a_3 T^3 + a_4 T^4)S_a + (b_0 + b_1 T + b_2 T^2)S_a^{3/2} + d_0 S_a^2$$
$$[\text{kg·m}^{-3}], (A3.2)$$

where $a_0 = 8.24493\cdot10^{-1}$ kg·m^{-3}·‰$^{-1}$, $a_1 = -4.0899\cdot10^{-3}$ kg·m^{-3}·‰$^{-1}$·°C^{-1}, $a_2 = 7.6438\cdot10^{-5}$ kg·m^{-3}·‰$^{-1}$·°C^{-2}, $a_3 = -8.2467\cdot10^{-7}$ kg·m^{-3}·‰$^{-1}$·°C^{-3}, $a_4 = 5.3875\cdot10^{-9}$ kg·m^{-3}·‰$^{-1}$·°C^{-4}, $b_0 = -5.72466\cdot10^{-3}$ kg·m^{-3}·‰$^{-3/2}$, $b_1 = 1.0227\cdot10^{-4}$ kg·m^{-3}·‰$^{-3/2}$·°C^{-1}, $b_2 = -1.6546\cdot10^{-6}$ kg·m^{-3}·‰$^{-3/2}$·°C^{-2}, $d_0 = 4.8314\cdot10^{-4}$ ‰$^{-2}$, S_a is solution salinity [‰], and $\rho_w(T)$, the density of the *Standard Mean Ocean Water*, is given by

$$\rho_w(T) = e_0 + e_1 T + e_2 T^2 + e_3 T^3 + e_4 T^4 + e_5 T^5 \qquad [\text{kg·m}^{-3}],$$

with $e_0 = 999.842594$ kg·m^{-3}, $e_1 = 6.793952\cdot10^{-2}$ kg·m^{-3}·°C^{-1}, $e_2 = -9.09529\cdot10^{-3}$ kg·m^{-3}·°C^{-2}, $e_3 = 1.001685\cdot10^{-4}$ kg·m^{-3}·°C^{-3}, $e_4 = -1.120083\cdot10^{-6}$ kg·m^{-3}·°C^{-4}, $e_5 = 6.536332\cdot10^{-9}$ kg·m^{-3}·°C^{-5}. The formula (A3.2) is valid for 0 ‰ $\leq S_a \leq$ 42 ‰ and -2 °C $\leq T \leq$ 40 °C, and standard deviation is of 3.6·10^{-3} kg·m^{-3}.

Refractive index of a NaCl water solution as function of solution salinity, temperature and wavelength is given by [83]:

$$n_s(S_a, T, \lambda) = n_0 + (n_1 + n_2 T + n_3 T^2)S_a + n_4 T^2 + \frac{n_5 + n_6 S_a + n_7 T}{\lambda} + \frac{n_8}{\lambda^2} + \frac{n_9}{\lambda^3} \qquad [\text{-}], \qquad (A3.3)$$

where $n_0 = 1.31405$, $n_1 = 1.779 \cdot 10^{-4}$ ‰$^{-1}$, $n_2 = -1.05 \cdot 10^{-6}$ ‰$^{-1} \cdot °C^{-1}$, $n_3 = 1.6 \cdot 10^{-8}$ ‰$^{-1} \cdot °C^{-2}$, $n_4 = -2.02 \cdot 10^{-6}$ °C^{-2}, $n_4 = -2.02 \cdot 10^{-6}$ °C^{-2}, $n_5 = 15.868$ nm, $n_6 = 0.01155$ nm$\cdot$‰$^{-1}$, $n_7 = -0.00423$ nm$\cdot°C^{-1}$, $n_8 = -4382$ nm^2, $n_9 = 1.1455 \cdot 10^6$ nm^3, S_a [‰] is the solution salinity, T [°C] is the solution temperature, and λ [nm] is the radiation wavelength. The ranges of validity are 0 °C $\leq T \leq$ 30 °C, 0 ‰ $\leq S_a \leq$ 35 ‰, and 400 nm $\leq \lambda \leq$ 700 nm. The maximum deviation is less than $5 \cdot 10^{-5}$.

Molar mass of a NaCl water solution with salinity S_a, when molar masses of water and salt are M_{H_2O} and M_{NaCl}, is from the definition of salinity given by

$$M_s(S_a{}^*) = \frac{m_{H_2O} + m_{NaCl}}{N_{H_2O} + N_{NaCl}} = \frac{m_{H_2O} + m_{H_2O}\left(\frac{S_a{}^*}{1 - S_a{}^*}\right)}{\frac{m_{H_2O}}{M_{H_2O}} + \frac{m_{H_2O}\left(\frac{S_a{}^*}{1 - S_a{}^*}\right)}{M_{NaCl}}} = \left(\frac{1 - S_a{}^*}{M_{H_2O}} + \frac{S_a{}^*}{M_{NaCl}}\right)^{-1} \qquad [\text{kg} \cdot \text{mol}^{-1}], \qquad (A3.4)$$

where m [kg] and N [mol] are mass and number of moles, and $S_a{}^* = 10^3 S_a$ [-].